Broadband TeraHertz Time Domain Spectroscopy for Rapid Material Characterization

BY
Josh Gibbs

A thesis submitted to the Faculty of Graduate Studies of The University of Manitoba in partial fulfillment of the requirements for the degree of

Master of Science

The Department of Physics and Astronomy
The University of Manitoba
Winnipeg, Canada
October 2022

Thesis advisor: Professor Jacob Burgess Josh Gibbs

Broadband TeraHertz Time Domain Spectroscopy for Rapid Material Characterization

Abstract

This work revolves around the design and construction of a broadband terahertz time domain spectrometer using nonlinear optics for the generation and detection of THz light. Methods for signal collection and processing are discussed, including the removal of spurious reflection using window functions. Furthermore, attenuated total reflection is optimized for THz light as a means to circumvent critical issues faced when working with polar solvents or highly absorbing samples. The discussion then turns to the calibration and analysis of performance of the spectrometer with measurements of the THz power and peak THz electric field generated by the spectrometer as well as evaluation of the signal-to-noise and dynamic range of the instrument. Issues involving humid air are introduced and re-framed as a way of using a slight contamination of water vapour as an internal standard. Finally, it is shown how THz-TDS can be used to characterize low energy phenomena in two uniquely different classes of materials, namely that of magnetic metal oxides and organic chiral species. The former analyzes materials that may find use in the development of new computational devices, while the latter forms the basis for quick way to differentiate between isomeric species present in liquid and solid phases.

Contents

Listing of figures

Listing of tables

Listing of abbreviations

ADC Analog-to-Digital converter
ATR Attenuated total reflection
a.u. Arbitrary units
DR Dynamic Range
EM Electromagnetic
EO(S) Electric-optic (sampling)
FFT Fast Fourier Transform
DFG Difference frequency generation
DFT Discrete Fourier Transform
FID Free induction decay
FP Fabry-Pérot
FWHM Full-width half max
GHz Gigahertz
HDPE High-density Polyethylene
HRFZ High-resistivity float-zone
IR Infrared
NPs Nanoparticles
OAP Off-axis parabolic
OR Optical rectification
SHG Second harmonic generation
SNR Signal-to-noise ratio
TDS Time domain spectroscopy
THz Terahertz
TO Transverse-optical

For the fools who dream.

Acknowledgments

THIS WORK would not have been possible without the help and input from so many people. This list is far from comprehensive, however, there are numerous people in which I would like to personally thank.

First and foremost I would like to thank my supervisor Dr. Jacob Burgess for the opportunity and support throughout the time I spent in his lab. During my time here, I learned indelible skills that helped me grow as a scientist, and for this I am grateful.

I would also like to express my earnest gratitude to Akif Ahmed and AJ Braconnier for their help with optics and all of the interesting conversations, both academic and otherwise. Sangeev Selvaratnam deserves a special thanks for all his help with 3D design and our talks of camping. I would also like to thank Christie Balanduk and Nils Refvik for their contributions to the lab.

Thank you Dmitry Vrublevskiy for all of the samples you provided, as well as the excellent conversations on metal oxides and music.

This work would not have been possible without the help of the office staff Susan, Aymsley, and Robyn, and technical staff Maiko and Peiqing. I would also like to thank NSERC and Mitacs for their contributions to funding this work. The Lab2Market program was a wonderful opportunity to learn about business, and for this I am appreciative of Brenda Frisk.

Last, but not least, I would like to thank my friends and family for their continued love and support they have offered over the years. This would not have been possible without them. And a special thanks to Sarah and Brutus for the wonderful times at the dog park.

We have artists with no scientific knowledge and scientists with no artistic knowledge and both with no spiritual sense of gravity at all, and the result is not just bad, it is ghastly.

Robert M. Pirsig

1 Introduction

Although still in it's adolescence, terahertz (THz) spectroscopy offers rich insight into many different low energy phenomena. Infrared (IR) spectroscopy has been known for many decades to be a deeply useful technique in elucidating vibrational modes of molecules and fingerprinting complex molecular structures. However, due to the so-called THz gap, the far IR part of the electromagnetic spectrum remains the final frontier and is largely unexplored. Recent progress in generation and detection schemes[1,2,3] have led to tremendous growth and development of THz spectroscopy, finding uses in pharmaceutical manufacturing,[4,5,6] explosive and illicit drug detection,[7,8,9,10,11] food and botanical extracts quality control,[12,13] and solid state devices.[14,15,16,17]

The THz region of the electromagnetic (EM) spectrum lies between infrared and microwave, covering the frequency range 0.1 - 10 THz. Photons at these energies* are able to excite slow, complex vibrations, *e.g.*, molecular skeletal vibrations and crystal lattice phonons,[18] weak intermolecular forces such as hydrogen bonds[19] and other non-covalent interactions, and molecular rotations, as can be seen in Fig. 1.1. These characteristics, along with the fact that THz is non-ionizing, suggests that THz spectroscopy and imaging are considered completely non-invasive techniques. Many non-conducting materials

*About 4 - 20 meV for 1 THz and 5 THz, respectively.

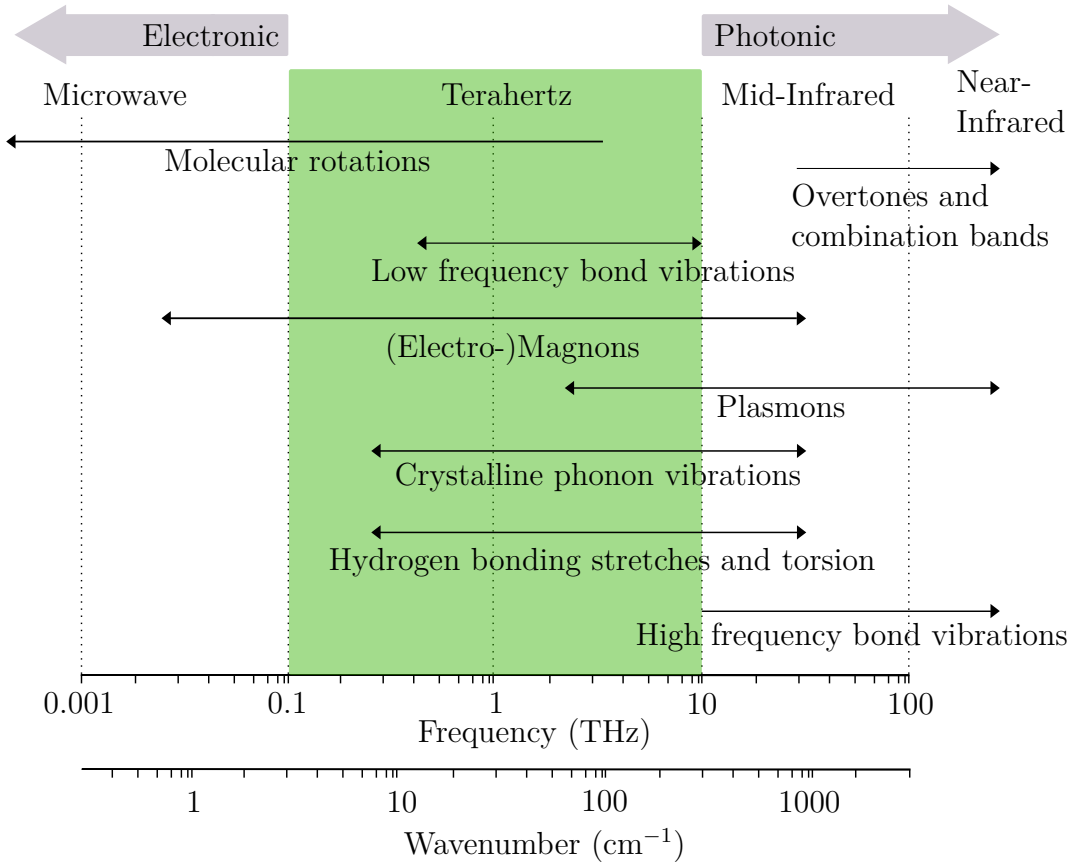

Figure 1.1: The THz region of the EM spectrum, depicting low energy phenomena that can occur in this frequency range.

are relatively transparent to THz light due to the low energy of THz photons, making THz imaging a useful tool for security screening.[20,21] The longer wavelengths (*i.e.*, 10s to 100s of μm) allows for probing of specific layers in composite materials such as historical works of art.[22,23]

The colloquial term "THz gap" originates from the difficulties that arise in generating EM radiation in the THz range. Traditional THz EM sources operate either electrically, where oscillating charge carriers induce a propagating EM wave, or optically, where photon energies are down-converted to the desired energy level. However, both of these approaches give rise to significant problems in the THz region. Increasing frequencies in the electrical regime is limited to charge carrier mobility and the rise/fall times of said carriers which are typically on the order of nanoseconds and constrains generation to

100s of GHz. On the other hand, attempting to reduce optical frequencies emitted from electronic transitions in semiconductors in the THz range is inhibited by the energy of transitions required to produce THz light being less than ambient thermal energy at room temperature ($k_BT \geq h\nu_{THz}$).

While they are becoming more common, spectroscopic techniques to probe intermolecular forces and low frequency transitions have historically been difficult to realize due to the aforementioned challenges. Given that frequencies in the THz range are too slow to produce optically and too fast to form electronically, this requires bridging the electronic and photonic regimes and consequently, our understanding of how materials behave in response to THz radiation. Current progress in communications and computing technologies have necessitated a shift in operating frequencies from low/mid GHz to high GHz - low THz,[24] and with this arises the need for rapid characterization of materials that can operate in the THz region. While novel machine learning methods have been developed in an attempt to predict materials and their properties, these all require meticulously curated empirical data sets for training and validation.[25,26]

Two areas in which THz spectroscopy could prove greatly beneficial are in the development of new solid state devices utilizing spintronics and chirally selective organic catalysts. Both of these areas have received considerable attention is recent years in the hopes of offering power alternatives to current technologies. The following two subsections offer a brief overview of technologies relating to these fields, and how rapid characterization with THz spectroscopy could greatly aid in the material discovery process.

Spintronics

One field where low energy interactions is of great interest is that of spintronics, a portmanteau of spin transport electronics. Spintronics offers a low power alternative to creating logical circuits by using the spin of a single or small ensemble of particles rather than the flow of charge.[27] By utilizing a particle's spin to transfer information, spintronics allows for the transfer of information to occur where charge transfer is normally prohibited (*i.e.*, insulators). One way of accomplishing this in practice is through the use of magnmolecular vibrations and rotations as well as intermolecular modesmolecular vibrations and rotations as well as intermolecular modesons. These are quantized

collective spin excitations in which the spin state of individual electrons in a magnetic lattice are coupled into a propagating wave of coherent magnetization.

Antiferromagnetic (AF) materials are an attractive candidate for construction of such devices as they have magnetic order, yet remain insensitive to external magnetic fields.[28] To date, most AF materials that have been discovered are commonly insulating by nature, yet exhibits excitations at THz frequencies. This allows for high frequency spin waves to be used in the construction of THz sensors, computational elements, and other devices using materials that have AF order.[29]

Isomer detection

In addition to solid state devices, THz spectroscopy can be used for isomeric differentiation and the analysis of hydrogen bonds[30]. Isomers and tautomers are different conformations of the same molecules and are very prevalent in the synthesis of medicinal compounds and drug interactions in the human body, among other things. There are currently no reliable forms of determining the presence of different isomers that are simultaneously inexpensive and efficient in facilitating the distinction between these conformations in heterogeneous mixtures, or that enable the rapid measurements of concentration for different conformations present. This type of chemical fingerprinting and other studies of low energy phenomena are of great importance to the pharmaceutical industry and organic catalysis, which won the 2021 Nobel Prize in chemistry.[31] Additionally, these are often species that require being dissolved or suspended in solvents. Many polar and protic solvents give rise to molecular vibrations and rotations as well as intermolecular modes[32] in the THz region that can obstruct information of interest in experiments done with THz spectroscopy.

Addressing Issues in THz-TDS

Unfortunately, in addition to problems involving species dissolved in polar or protic solvents, THz light also has strong absorption lines from ambient humidity due to hydrogen bonding, molecular rotations, and electric polarization effects in atmospheric water vapour.[32] Therefore, humid air must be removed in order to mitigate the presence of unwanted peaks in the final spectra. This requires an inert gas purgebox to be constructed around the instrument, which greatly hampers sample throughput as it

requires significantly more time exchanging samples as well as time spent waiting for the volume within the instrument to be purged. One way to circumvent polar solvent absorptions and time lost to purging the apparatus is to utilize attenuated total reflection (ATR) through the use of a internal reflection element that has been built into the purgebox itself.

ATR is a technique that has already found common use in IR spectroscopy. It is used to describe experiments where the sample is placed on a prism in which the beam is passed through at such an angle to allow for total internal reflection to occur. There are numerous advantages to using this technique, such as its ability to scan many different types of samples, including powders, liquids, thin films, and polymers, with little to no preparation. Additionally, ATR can be used in experiments that would normally not permit transmission experiments due to high absorbance, such as optically thick materials or analytes dissolved in polar liquids. Careful consideration must be put into the choice of prism material however, as total internal reflection only occurs when the sample has a lower index of refraction than the prism. Geometry of the prism also plays a key role in reducing power loss due to reflections and increasing penetration depth of the evanescent wave formed at the prism interface.

To summarize, spectroscopy is an important tool used in the non-destructive examination of samples of interest. The longer wavelengths of THz light compared to IR makes it useful in studying low energy phenomena in numerous phases of materials. This includes magnetic interactions that can be used to create new computational elements and the distinction of chiral species. While THz technology has recently been finding use in many areas of study, it is still new enough that its applications are still being discovered. The development of ATR THz-TDS helps to solve some large hurdles that arise in building these type of spectrometers, hopefully allowing large scale production of instruments and the incorporation of inline manufacturing quality control methods. In turn, this will allow THz-TDS to reach farther corners of the market for these instruments sooner, expediting the discovery process. With this, databases of THz spectroscopic data can be generated significantly faster than with conventional purge methods, filling big gaps in our understanding of THz light and hopefully related fields like spintronics and pharmaceutical research.

The work presented in this thesis is organized as follows:

Chapter 2 discusses the theory pertaining to generation and detection of THz electromagnetic radiation using nonlinear optics. The use of optical rectification and electro-optic sampling for generation and detection of THz light will be discussed, as well as challenges and techniques in data collection and processing. This chapter will also include an introduction of ATR and discuss how it can be optimized for use in THz-TDS.

Chapter 3 outlines the experimental methodology and instrumental parameters used in collecting the THz data for the experiments done in this thesis. The THz power measured by the instrument will be compared to that of a commercial power meter and metrics for evaluating the performance of the instrument will also be discussed. Additionally, sample preparation automated purge methods are examined.

Chapter 4 shows how THz-TDS can be used for the analysis of multiple classes of materials. This includes common metal oxides that may find use in antiferromagnetic or multiferroic devices and other solid state technologies, and the detection of different vibrational/rotational modes of organic molecules which can allow for rapid differentiation between isomers.

Chapter 5 offers an outlook of how THz-TDS can be used to study low energy phenomena that are found in many different industries, from low power electronic devices to pharmaceutical manufacturing. Furthermore, it discusses areas in which could benefit from the use of THz-TDS and ways to expand the technology.

Table 1.1: Useful values in the THz range

Unit	1 THz	5 THz
Angular frequency $\omega = 2\pi\nu$	6.28 THz	31.4 THz
Wavelength $\lambda = \mathrm{c}/\nu$	300 μm	59.96 μm
Period $\tau = 1/\nu$	1 ps	0.2 ps
Wavenumber $\bar{k} = \mathrm{k}/2\pi = 1/\lambda$	33.3 cm^{-1}	166.8 cm^{-1}
Photon energy $\mathrm{h}\nu = \bar{h}\omega$	4.14 meV	20.7 meV
Temperature $\mathrm{T} = \mathrm{h}\nu/\mathrm{k}_B$	48 K	240 K

If people do not believe that mathematics is simple, it is only because they do not realize how complicated life is.

John von Neumann

2 Theory

Spectroscopy is a non-destructive technique that began as a way of evaluating materials based on their response to incident EM radiation. If the frequency of the EM wave is the same as a natural frequencies of the system, the energy can be transferred into the system which then excites certain fundamental processes. Therefore, a spectrum of colours could be transmitted, reflected, or otherwise tangentially applied to a sample, and the resulting spectrum could then be compared to the reference spectrum allowing researchers to glean intrinsic properties of a sample. Other forms of spectroscopy have since been developed to include non-EM sources, *e.g.*, neutron diffraction spectroscopy or acoustic spectroscopy, and it has since become the study of how energy, waves, and frequencies interact with the material of interest.

This chapter focuses on how terahertz time-domain spectroscopy (THz-TDS) is done in practice, from generation and detection of THz EM radiation, and on to the processing and analysis of data collected from THz-TDS experiments. Furthermore, techniques for optimization of attenuated total reflection (ATR) will be discussed as a means to circumvent critical issues faced in working with THz light.

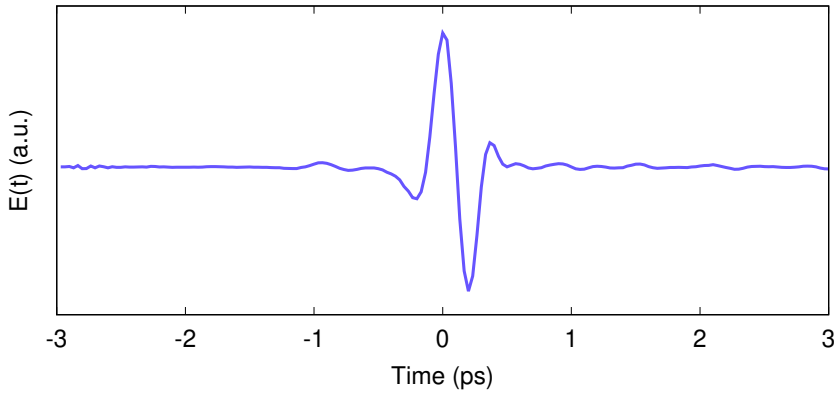

Figure 2.1: An experimentally collected time resolved single cycle THz pulse generated from the optical rectification of 1040 nm light in (110) cut GaP.

2.1 THz Time Domain Spectroscopy

In THz-TDS, a single cycle pulse of THz EM radiation is first generated in a nonlinear crystal and then recorded by measuring the intensity of the electric field of the pulse at different points in time. An example of such a pulse produced from the instrument constructed in this work can be seen in Fig. 2.1. This process relies on the use of nonlinear optics for both generation and detection of THz light. It is accomplished by first splitting the beam of a NIR laser into two separate components, the pump and the probe, and subsequently measuring polarization changes of the probe due to the THz generated by the pump. THz light can also be generated and detected using photoconductive antennas, however this work focuses solely on generation and detection of THz light using nonlinear optics.

In order to measure the THz pulse with sub-picosecond resolution, the path length of the pump is changed relative to that of the probe on the order of 10s of μm. Since the speed of light remains more or less constant regardless of wavelength (ignoring dispersion), each spatial step that changes the path length translates directly to the time taken for the beam to traverse that path within the instrument. Therefore, a 10 μm change in path length corresponds to a 33 fs step in time.

Time domain measurements offer several unique advantages over frequency domain spectroscopy. While collecting data in either time or frequency domains allows for amplitude measurements, TDS also has the inherent advantage of preserving the phase

characteristics of the EM radiation. This leads to the ability to temporally resolve events excited by the THz pulse. The Fellgett advantage[18] commonly ascribed to FTIR applies to THz-TDS as well. It describes an improvement in the signal-to-noise ratio (SNR) of a multiplexed signal over that of a monochromatic collection using a CCD. Effectively, there is less error in a signal where all of the frequency data is collected simultaneously and extracted from the time domain compared to direct measurements over the frequency domain.

2.1.1 THz Generation

Most optical phenomena are dictated by the response of the material's electrons to external EM waves. Application of an oscillating electric field can induce motion for free charge carriers as well as couple to and excite motion of electrons localized in the molecular orbitals the material. When charges are accelerated, there is a subsequent release of EM radiation while energy is dissipated as the particles returns to their initial energy state. For homoatomic crystalline materials this means that electrons oscillate equally back and forth along the σ bonds that hold the crystal together. This picture is similar for binary polyatomic crystals, however, here the σ bond tends toward ionic bonds and movement along the bond will be biased towards the direction of the atoms with higher electronegativity creating a non-harmonic potential and is the basis for nonlinear effects. This process is largely governed by charge carrier mobility and their related relaxation time dictates the bandwidth of generation. Materials that feature non-symmetric potentials give rise to many nonlinear effects including difference frequency generation, optical rectification, and the Pockels effect, to name a few. Before delving into optical rectification, the fundamental process in which THz is generated for these experiments, we first must form a good understanding of polarization effects in the solid state.

Polarization in Solids

In dielectrics, the polarization response $\vec{P}$ due to an applied electric field $\vec{E}$ can be expressed as

$$\vec{P} = \chi \epsilon_0 \vec{E} \tag{2.1}$$

where χ is the electric susceptibility and ϵ_0 is the permittivity of free space. Susceptibility usually takes the form of a scalar in linear isotropic materials, however when the applied field is sufficiently strong, many anisotropic materials fall in the nonlinear regime where susceptibility becomes a second rank tensor, $\chi^{(2)}_{ijk}$. This results in higher order polarization effects becoming much more prominent in such materials, where $\vec{P}$ may not be collinear with $\vec{E}$. Given that $n = \sqrt{(1+\chi)}$, a nonlinear materials refractive index also becomes a tensor. Materials where diagonal elements of the refractive index tensor are not equal are said to be birefringent. An example of such a material is calcite, which leads to a doubling of images viewed through the sample due to the different indices of refraction along different crystal planes. This phenomenon will be further explored in the following subsection.

In nonlinear materials, the polarization response under a sufficiently strong electric field then becomes

$$P_i = \sum_j \chi^{(1)}_{ij} E_j(t) + \sum_{jk} \chi^{(2)}_{ijk} E_j(t) E_k(t) + ... \tag{2.2}$$

which now reflects the higher order terms that arise from the susceptibility tensor. Here i, j, k denote the Cartesian components of the electric field. In the second order term of equation 2.2, P_i is now proportional to E^2, and therefore the pulse becomes positive. It is often convenient to refer to the envelope that encompasses the electric field pulse. In the far field limit of the dipole approximation, the THz pulse can be approximated by taking the second time derivative of the IR pulse envelope,[33] $E_{THz} \sim \frac{\partial^2 P(t)}{\partial t^2}$. This is expanded upon in Appendix A.

The nonlinear polarization response of a material due to difference frequency generation, a second order nonlinear effect, can then be expressed as[34]

$$P^{(2)}_i(\omega_2 - \omega_1) = \sum_{j,k \in (x,y,z)} \epsilon_0 \chi^{(2)}_{ijk} E_j(\omega_2) E^*_k(\omega_1) \tag{2.3}$$

where $\omega_{1,2}$ are the frequencies of the electric fields of incident photons, and $\chi^{(2)}_{ijk}$ is the susceptibility tensor for the given crystal system. Here we consider the electric field of two photons of different frequencies, $E_j(\omega_2)$ and $E^*_k(\omega_1)$ which combine to give the polarization response $P^{(2)}_i$ in the form of a second rank tensor.

Nonlinear polarization terms are zero in materials with inversion symmetry due to symmetries of the susceptibility tensor and therefore, require materials with noncentrosymmetric symmetry. In GaP for example, a noncentrosymmetric crystal with space group $F\bar{4}3m$, the susceptibility tensor can be written in terms of the effective nonlinear coefficients $d_{il} = \frac{1}{2}\chi^{(2)}_{ijk}$

$$\frac{1}{2}\chi^{(2)}_{ijk} = \begin{pmatrix} 0 & 0 & 0 & d_{14} & 0 & 0 \\ 0 & 0 & 0 & 0 & d_{14} & 0 \\ 0 & 0 & 0 & 0 & 0 & d_{14} \end{pmatrix}$$

For highly symmetric crystals, many of the tensor elements can be equated to each other or reduced to zero. The elements that remain define the orientation of the crystal that will enable light of a given polarization to couple to the crystal bonds and undergo nonlinear optical processes. For crystals with the space group $F\bar{4}3m$ this angle lies normal to the (110) plane.

Optical Rectification

Optical rectification (OR) is a second-order nonlinear optical effect in which THz is created through difference frequency generation of monochromatic light. The polarization response for OR takes the same form as difference frequency generation, however since the light is monochromatic $\omega_1 = \omega_2 = \omega$, and therefore equation 2.3 becomes

$$P^{(2)}_i(0) = \sum_{j,k\in(x,y,z)} \epsilon_0 \chi^{(2)}_{ijk} E_j(\omega) E^*_k(\omega) \tag{2.4}$$

When the electric field of incoming photons couples to electrons that form the σ bonds of the crystal, photons of the same frequency combine to form a quasi-DC field which rectifies the signal and generates photons of THz light. This process is strongly dependent on the crystals orientation, as THz generation power is maximized when the polarization of the incident beam oscillates the same direction as the bonds within the crystal. For crystals of the space group $F\bar{4}3m$, light travelling along the [110] axis can couple to bonds parallel to the $[\bar{1}11]$ or $[1\bar{1}1]$ axes. The angular dependence of the

polarization can then be written as[35]

$$|P|^2 = 4\epsilon_0^2 d_{14} E_0^4 \sin^2\theta \left(4\cos^2\theta + \sin^2\theta \sin^2\phi\right) \tag{2.5}$$

where θ is the polar angle between the polarization of the beam and the [001] axis, and ϕ is the azimuthal angle. Equation 2.5 is optimized when $\sin^2\phi = 1$, or when $\phi = \pi/4$ or $3\pi/4$ which aligns the polarization with the crystal bonds. Motion of the electrons between atoms is dependent on their electronegativities, which form an asymmetric potential and therefore effectively changes the force constants experienced by the electrons. These disproportionate oscillations are the basis for rectification. Fig. 2.2 shows the relationship between the polarization angle around the [110] axis and the resulting THz power. This plot shows how measured THz power matches the theoretical generation power described by equation 2.5. When using NIR light sources (1040 nm), second harmonic generation also creates green light (520 nm) which serves as an indicator for the generation of THz and can aid in alignment of the pump beam to optimize THz generation and detection.

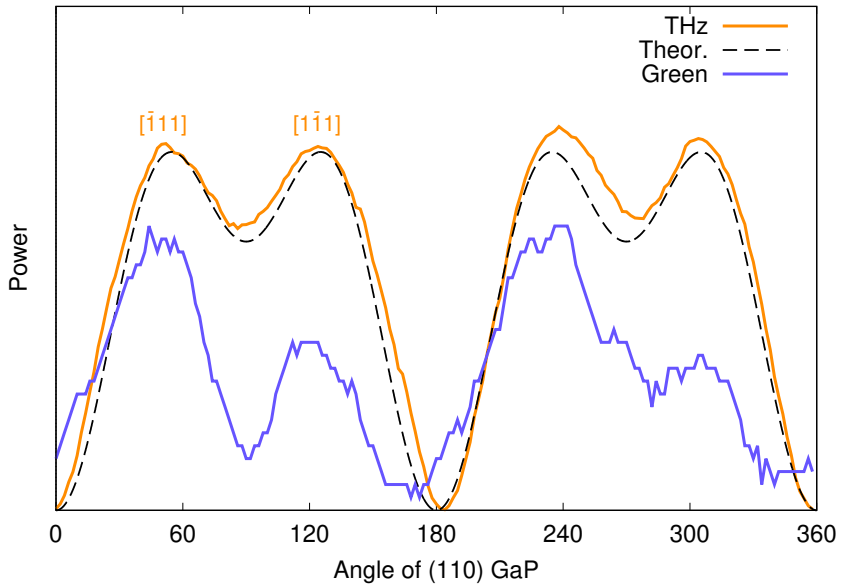

Figure 2.2: THz power generated by optical rectification in GaP as polarization is rotated around the [110] axis compared to the theoretical polarization response given in equation 2.5. Also shown is the power of green light (520 nm) generated by second harmonic generation, both measured using the instrument built in this work.

Choice of Generation Material

Ideally, the phase of the generated THz pulse should move through the generation material at the same rate as the IR group velocity, as this velocity matching would help elicit the gradual amplification of the THz field. This is often not the case in real nonlinear crystals however, as dispersion leads to spatial, and therefore temporal delay between the group and phase velocities, which are given by

$$v_{gr}(\omega) = \frac{\partial \omega}{\partial k} \quad ; \quad v_{ph}(\omega) = \frac{\omega}{k} \tag{2.6}$$

respectively. In the book Principles of Terahertz, Lee explains that ZnTe is the most widely used material for generation of THz EM radiation due to its low dispersion and therefore, exceptional phase matching.[35] However, due to previously mentioned symmetries in the susceptibility tensor, any crystal with the space group $F\bar{4}3m$ (GaP, GaAs, InP, *etc.*) will be able to generate THz through OR. Work by Hoffman *et al.* has compared the generation of THz light in multiple nonlinear crystals and have shown that $LiNbO_3$ and GaP far outperform ZnTe at 1035 nm.[36] However, while LiNbO3 (d_{eff} = 152.4 pm/V) has a much higher nonlinear coefficient than GaP (d_{eff} = 21.7 pm/V) and therefore, better generation efficiency, it requires a more complex tilted pulse front setup to accommodate phase mismatch caused by its high refractive index.[37] Negel *et al.* also report that GaP is a better material for THz generation than other III-V semiconductors like ZnTe and GaAs due to better phase matching.[38] Table 2.1 compares important properties of common THz generation crystals.

Table 2.1: Common materials used for generating THz EM radiation, where d_{eff} is the highest nonlinear coefficient.

Material	d_{eff} (pm/V)	Bandwidth (THz)	Space group
GaP	21.7	6.5	$F\bar{4}3m$
GaAs	46.1[39]	2.5	$F\bar{4}3m$
ZnTe	90[40]	3.5	$F\bar{4}3m$
$LiNbO_3$	152.4	2.5	$R3c$
DAST	490[41]	16+	$C2/m$

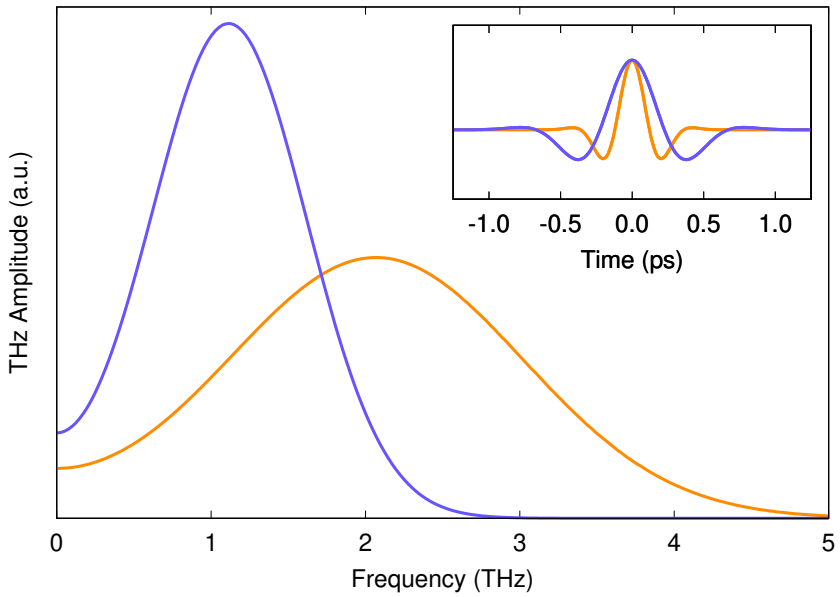

Figure 2.3: A comparison of simulated THz pulses and the resulting spectra. The inset figure shows two pulses of different temporal lengths of the form $E = E_0 e^{-\alpha t^2} \cos(\omega t)$, while the outset plot shows the spectra after Fourier transform. Pulses shorter in time produce wider bandwidth spectra.

In generating THz through OR, the thickness of the crystal plays a critical role in both efficiency and bandwidth. Due to phase mismatch, there is a direct trade off between the thickness of the crystal in the conversion of IR to THz and THz phase delay that leads to pulse width broadening in time. Due to dispersion, thinner crystals provide higher bandwidth as there is reduced temporal widening of the pulse. However, when the volume of the crystal that IR passes through is reduced, so to is the efficiency of generation, which scales with the volume that the beam occupies in the material. Fig 2.3 illustrates the effect of pulse broadening in the resulting spectra after Fourier transformation on simulated pulse envelopes.

In terms of dispersion, the generation crystal should ideally be infinitesimally thin as to minimize the broadening of the pulse, however as the crystal thickness approaches the pulse length there is the risk of self-interference due to internal reflections. The coherence length l_c is defined as the distance the THz pulse can propagate before its phase is retarded by $\pi/2$ and is written

$$l_c = \frac{c}{2\nu_{THz}|n_{gr} - n_{THz}|} \tag{2.7}$$

where n_{gr} and n_{ph} the group and phase indices of refraction and depend on v_{gr} and v_{ph}. Zhao *et al.* posit that the bandwidth of THz generated becomes saturated as the generation crystal becomes thinner and that the ideal crystal thickness is 0.2 mm.[42] This implies that there is interest in keeping the crystal thickness longer than l_c to avoid destructive interference and saturation of the crystal. According to Wu *et al.*, GaP has wider spectral bandwidth than either GaAs or ZnTe due to carrier mobility and can reach up to 6.5 THz.[43] Cui *et al.* report 20x amplitude increase in generation of 6.5 THz with grating etched 0.2 mm GaP.[44] This is due to group and phase index matching based on diffraction angle, which induces amplification of the electric field. The unit cell and (110) plane of GaP, a $F\bar{4}3m$ crystal, can be seen in Fig. 2.4.

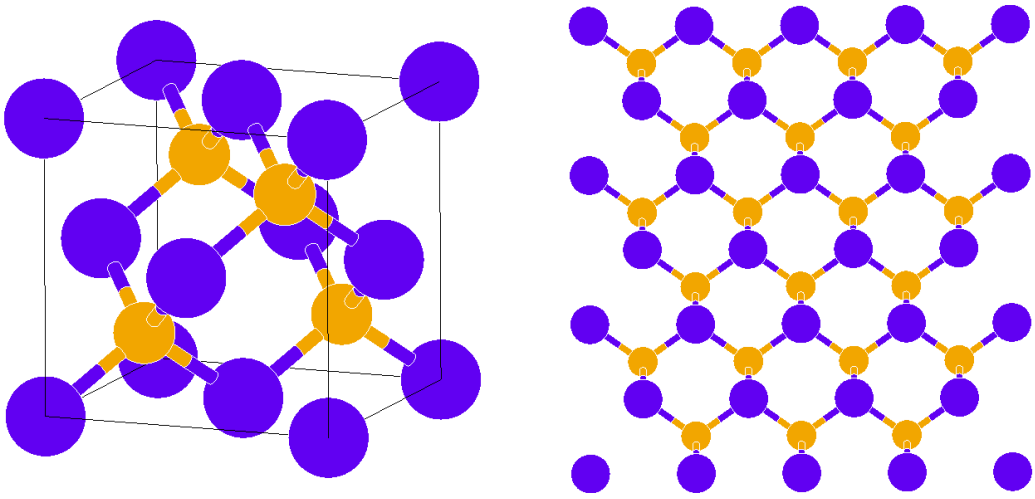

Figure 2.4: Image on the left shows the unit cell of GaP and the image on the right is the (110) plane of GaP, illustrating the bonds that allow incoming photons of a given polarization to couple to the electrons and generate THz light through OR.

The spectral bandwidth of generation is largely dominated by absorption processes in the THz range due to the fact that noncentrosymmetric symmetry leads to the presence of polarity/dipole moments and therefore, absorptions due to these processes. Transverse-optical (TO) phonon modes are the predominate absorption present in most generation crystals.[45] The lowest phonon mode of ZnTe is 5.3 THz, greatly hampering any ability to produce spectral content above that region, even at cryogenic levels. The

lowest phonon mode in GaP is 11 THz,[46] although this can be greatly reduced if the generation crystal is cooled to 80 K.[47] Generation with OR in organic crystals, such as 4-N,N-dimethylamino-4'-N'-methyl-stilbazolium tosylate (DAST), can reach a bandwidth of up to 30 THz.[48] Although DAST has considerably higher nonlinear coefficient (d_{eff} = 490 pm/V[41]), the group and phase velocity matching criteria is only met with 1550 nm light. Also, in addition to significant TO phonon modes between 1-5 THz, the resultant THz fields are much more complex in both time and frequency domains, and therefore pose increased challenges in interpreting data collected with THz light generated by DAST.

It is possible to generate ultrabroadband THz light through OR. Kampfrath reports good phase matching in GaSe, which can lead to high bandwidth of up to 40 THz,[49] however these crystals have to be on the order of 10 μm thin and glued to thicker (001) cut windows of the same crystal to reduce destructive interference from internal reflections. They also point out the difficulty and cost of manufacturing these optics, and that the presence of the glue interface can still lead to problematic internal reflections. GaSe is also minorly birefringent, making nonlinear detection difficult. Moreover, generation above 400 cm^{-1} ($\sim$12 THz) is largely unnecessary as it is beyond the THz region and most commercial IR spectrometers are easily capable of generation in this range.

In terms of designing a broadband THz spectrometer for rapid characterization, a source that can generate a high bandwidth and clean spectrum should ideally be chosen. While DAST and GaSe can generate ultrabroadband spectra, the degradation of organic crystals and accompanying complexity of the electric field of DAST, and birefringence and complexity of manufacturing thin windows of GaSe make them difficult to work with. Of the available nonlinear semiconductor sources, GaP is broadband and has its lowest TO phonon mode is well above the maximum generation frequency. Also, the damage threshold of GaP far exceeds that of any organic crystal, and (110) cut GaP is also readily available as semiconductor wafer.

2.1.2 THz Detection

Much like THz generation, the detection of THz radiation can also make use of nonlinear polarization effects in noncentrosymmetric materials* in order to measure the intensity of the electric field of the THz pulse. As previously discussed, THz-TDS is accomplished by tracing out the intensity of the electric field through a method called electro-optic sampling (EOS)[50,51], which uses the electro-optic effect to measure the electric field of the THz pulse at different points in time. The electro-optic effect describes how a nonlinear material's optical properties change with the application of a static or slowly varying external electric field. This effect can induce a change in polarization of a beam travelling through such a material. When a material's index of refraction changes linearly with an applied electric field, this is known as the Pockels effect[52,53,54].

The Pockels effect

As introduced in the previous section, birefringence is a property of transparent media in which light is refracted differently depending on its polarization with respect to the specific crystal planes of the material and, therefore, is a function of the susceptibility tensor. The Pockels effect can be thought of as a form of birefringence induced by an electric field and can be used to detect THz EM radiation. Since the index of refraction only varies slightly in relation to the applied electric field, it can be approximated with a Taylor series expansion as

$$n(E) = n(0) + \frac{dn}{dE}E + \frac{1}{2}\frac{d^2n}{dE^2}E^2 + ... \tag{2.8}$$

Although the Pockels effect is a second order nonlinear effect due to polarization changes in a nonlinear crystal, also known as a Pockels cell, it is considered a first order effect in terms of change of refractive index (*i.e.*, first order as a function of electric field n(E)).† It is a very similar process to optical rectification, however, a material's response to the incident electric field is referred to in terms of the electro-optic coefficient (r_{ijk}) instead

*or photoconductive antennas, however, this work relies solely on the use of nonlinear optical effects.

†Although they are usually orders of magnitude weaker, higher order effects can be measured. The quadratic electro-optic effect, for example, is called the Kerr effect and is the basis for electro-optical Kerr effect which is used to design EO modulators.

of the nonlinear coefficient (d_{eff}). These can be related through the susceptibility tensor as[55]

$$\Delta n_i = \frac{1}{n_i}(\chi^{(2)}_{ijk} \cdot E_k) \quad \Delta n_i = -\frac{1}{2} n_i^3 (r_{ijk} \cdot E_k)$$

$$r_{ijk} = -\frac{2 \cdot \chi^{(2)}_{ijk}}{n_i^4} \tag{2.9}$$

In lossless media, the electro-optic coefficient is the same as the nonlinear coefficient, however this is not often the case. The negative in this relationship implies that these effects are inversely complementary, and therefore materials ideal for THz generation will also be ideal for EOS.

A Pockels cell comprised of a nonlinear material that is used for detection can be thought of as a voltage controlled waveplate, where the application of the electric field induces a quasi-static change to the birefringence much like that of a conventional waveplate. The polarization response due to the external field can be written as

$$P_i^{(2)}(\omega) = \sum_j \epsilon_0 \chi_{ij}^{(2)} E_j(\omega) \tag{2.10}$$

Here we can see that the polarization only depends on the electric field of one photon, compared to optical rectification which requires two-photon absorption. In terms of choosing the optimal material for creating the Pockels cell, the material should show no birefringence under normal incidence without the presence of an electric field. Fortunately, crystals with the $F\bar{4}3m$ space group are optically isotropic in $\chi^{(1)}$ and thus, are good candidates for EOS.

Because of the innate similarities between OR and the EO effect, many of the same restrictions of OR apply equally to EOS. Phase and group velocities play a similarly large role in EOS as they do in OR. The crystal thickness is directly proportional to the response amplitude, however it also leads to larger phase mismatch. Table 2.2 shows various EO materials and their performance in EOS, including the wavelength at which group and phase velocities match, λ_0, the effective electro-optic coefficient r_{eff}, and lowest phonon mode, ν_{phonon}. Wu *et al.* have shown that a 0.3 - 1 mm thick GaP for detection with 1060 nm light is the best choice for EO crystal, and that the THz phase index of refraction matches the IR group velocity at 8.43 THz.[43] GaP is described as

Table 2.2: Properties of common EOS materials used in THz-TDS. Here λ_0 is the IR wavelength in which phase matching in the nonlinear medium occurs, r_{eff} is the effective electro-optic coefficient, and ν_{phonon} is the lowest TO phonon. Data from Y. Lee's *Principles fo Terahertz*.[35]

Material	λ_0 (μm)	r_{eff} (pm/V)	ν_{phonon} (THz)
ZnTe	0.8	4.04	5.3
CdTe	0.97	6.8	4.3
GaP	1.06	1.43	11
InP	1.22	1.47[56]	9.2
GaAs	1.35	0.97	11

the ideal material for high bandwidth EO sampling by Pradarutti *et al.* due to phase mismatch in other material with higher r_{eff}, such as CdTe.[57]

Fig. 2.5 shows an experimentally measured THz pulse collected using a 0.3 mm GaP for detection. The lack of broadening seen in the pulse on the left leads to the full-width half-max (FWHM) of the pulse to be around 0.2 ps which leads to broadband THz generation, as can be seen in the spectrum on the right. The pulse compression of the laser, which is related to the pulse length of the IR envelope, can be adjusted in the laser settings, as can be seen in Fig. 2.6, where the plot shows the effect of pulse compression on the THz bandwidth. Changing this value emulates the effect of pulse broadening in OR and EO crystals and shows the reduction of bandwidth as the pulse length increases.

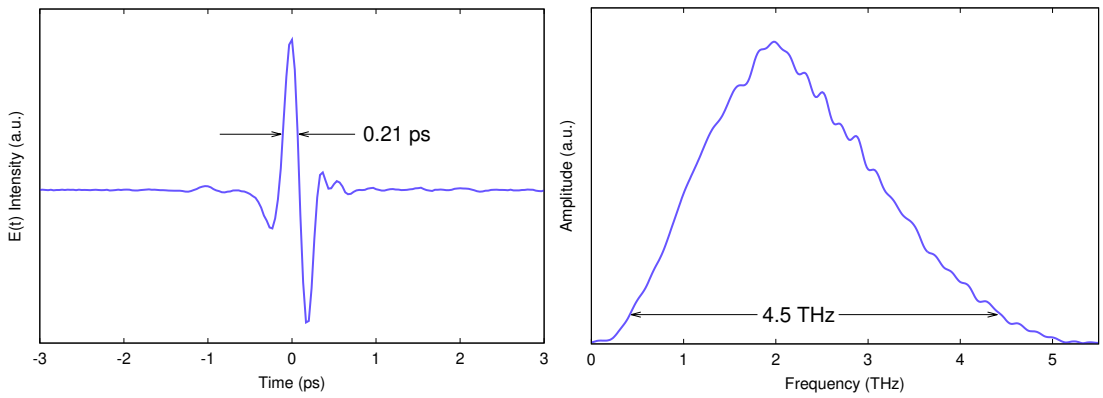

Figure 2.5: The THz pulse generated and detected by 0.3 mm GaP shown in time (left) and the resulting spectrum after Fourier transform (right).

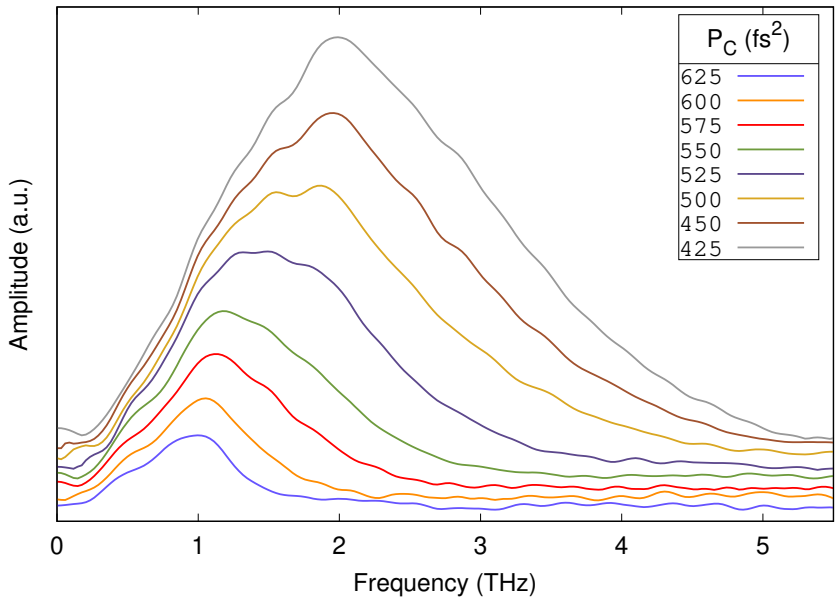

Figure 2.6: The resulting THz spectra of various values of pulse compression (P_C) of a 1 μJ pulse, as modulated by changing laser settings. The range of pulse compression from 425 - 625 fs^2 show the inverse nature between the pulse length and the spectral bandwidth, however true IR pulse size measurements are difficult to achieve without the use of an autocorrelator or FROG.

As the corresponding pulse length of all these spectra are all $\leq$ 1 ps, and given that the rise and fall time of electrical circuits are typically picoseconds to nanoseconds,[58] there is a need for the implementation of clever optical techniques to measure the profile of the THz pulse. This can be accomplished through balanced photodetection.

Balanced Photodetection

In THz-TDS the NIR beam is initially split into two different paths, the pump and probe. The pump is the portion of the beam used in THz generation, while the probe is what is actually measured. In order to measure the magnitude of the THz electric field, both beams are collinearly transmitted through the Pockels cell, which is comprised of a nonlinear crystal. When both optical paths are of equal length, the time taken for the THz pulse to traverse the instrument is the same to that of the probe pulse. Consequently, the electric field of the THz pulse is able to induce the Pockels effect and changes the polarization of the collinear IR probe beam from linear to elliptical. If

there is no THz light present, passing the beam through a $\lambda/4$ waveplate changes the linear polarization to circular. However, if THz is present, then the beam polarization is changed to elliptical. The beam can then be steered through a Wollaston prism which splits the vertical and horizontal components of the beam to be measured by balanced photodetection (BPD).

BPD measures the intensity of two beams relative to one another after the Wollaston prism splits the orthogonal components of the beam into two separate beam paths. These can subsequently be measured as a ratio that is directly proportional to the electric field intensity of the THz beam. The signal $S(t)$ is the response of the photodiodes of the detector to the intensity of the orthogonal components I_x and I_y. BPD therefore measures phase delay of ellipticity of the probe. Since we are comparing the ratio of the two polarizations, detector response is the normalized intensity of the electric field $E(t)$, and is recorded in arbitrary units (a.u.), although it is possible to calibrate the instrument to measure changes in polarization in μrad.

2.1.3 Signal Processing

Now that methods for generation and detection of THz have been established, we now turn to how data is collected and subsequently processed. Data in TDS is collected in the time domain, however, in order to analyze its frequency components, it is necessary to transform the data from the time domain to the frequency domain.

Fourier Transformation

The Fourier transform is a linear transformation that can be used to convert data from the time domain to the frequency domain, and *vice versa*.

$$F(t) \xrightarrow{FT} \tilde{F}(\omega)$$

This is accomplished by decomposing the signal $F(t)$ into its underlying frequency components

$$\tilde{F}(\omega) = \frac{1}{\sqrt{2\pi}} \int F(t) e^{-i\omega t} dt \tag{2.11}$$

where $\tilde{F}(\omega)$ is the signal in units of frequency and the factor $1/\sqrt{2\pi}$ is convention.[60] The signal created by the THz pulse is continuous, however, in order to physically collect signal through balanced photodetection it must be collected with an analog-to-digital converter (ADC) which leads to the signal becoming discretized. Therefore, the Fourier transform becomes the Discrete Fourier transform (DFT), where instead of collecting a signal as a continuous function, it is sampled at repeating intervals. The equation for the DFT becomes

$$x[k] = \sum_{n=0}^{N-1} x[n] e^{-i2\pi \frac{nk}{N}} \tag{2.12}$$

Here $x[n]$ is the signal strength collected at point n, and N is the number of points that have been sampled over.

The temporal separation between points n_k and n_{k+1} determines the highest frequency that can unambiguously be determined using DFT. If the sample rate of data collection is too low, the signal is said to be undersampled, which can lead to results that do not accurately convey the true 'essence' of the analog information. This effect is known as aliasing[59] and can create artifacts which greatly distort high frequency features in the data. The Nyquist frequency

$$f_N = \frac{N\Delta f}{2} \tag{2.13}$$

is the highest frequency that can be fully resolved from a signal and is equal to twice the bandwidth (B). Since the bandwidth of the time domain is inversely proportional to that of the frequency domain, data must be sampled at a rate of 1/2B Hz in order to capture the full bandwidth. For a bandwidth of 5 THz, the signal must be collected every 0.1 ps.

In recreating an analog signal in digital form, the resolution of features in the frequency domain is limited by the number of data points collected. The resolution is inversely proportional to the length of the scan collected as $\Delta f = 1/\Delta t$. Therefore, a 100 ps scan has 10 GHz resolution of spectral features. Zeros can be added to the end of a scan to help artificially extend the number of points in the scan, and therefore increase the resolution. It should be noted, however, that this method does not actually create any new information. Instead zero padding is equivalent to interpolating data and is a way of smoothing over the spectrum so as to make delineating meaningful data

easier to accomplish with the same amount of data.

Since the Fourier transform retains complex information, TDS allows for an analysis of the complex index of refraction. Anytime EM radiation is passed through some medium, there is always a component that is refracted or reflected, and a component that is absorbed. These can be related to the complex index of refraction by $\bar{n} = n + i\kappa$, where n is the real index of refraction relating to the components that are refracted/reflected, and κ is the extinction coefficient which is related to the complex term and is used to describe the absorption coefficient by $\alpha = \kappa \cdot 2\lambda/c$. By using amplitude and phase information available in TDS, one can obtain optical parameters without the use of the Kramers-Kronig relations.[61] This is relevant for reasons that will become apparent in the following chapter.

Suppressing Reflections

Due to the inverse nature between time and frequency resulting from the Fourier transform, one is required to collect longer scans in order to obtain high resolution data to deconvolve fine spectral features.[‡] It is necessary to scan for 100 ps or more to increase the resolution of the signal down to 10 GHz or less, however this becomes problematic when employing thin GaP for optical rectification and electro-optic sampling as this leads to the inclusion of spurious internal reflections, namely those formed by Fabry-Pérot (FP) etalon modes. The presence of these reflections leads to oscillations that form in the spectrum after Fourier transform, as can be seen in the top two plots in Fig. 2.7. The frequency of these oscillations is related to the temporal separation between the main pulse and its reflections as $\Delta f = 1/\Delta t$, where Δt is the time taken by the THz pulse to traverse the optical component and is given by

$$\Delta t = \frac{2dn_i}{c} \tag{2.14}$$

Here Δt is defined by the time required for light to traverse twice the thickness, d, of the optically denser medium, and c is the speed of light. For a 0.3 mm thick GaP crystal with $n_{GaP} = 3.34$,[62] these reflection occur at integer multiples of ∼7.5 ps after initial

[‡]Higher resolution does not always allow for spectral features to be fully distinguished. Appendix B introduces line shapes and shows how first and second derivatives can be used to help separate features of the spectrum.

pulse and all reflections of significant amplitude occur well within moderate resolution scan length.

In order to remove the FP etalon effects, reflections of the main peak must be removed from the signal. Arguably the easiest way to remove unwanted reflections is to employ antireflection coatings. Ahmed *et al.* have recently shown that this can be accomplished using carefully stacked films of Kapton™ tape on the optical component of interest.[63] Other methods involve algorithmically removing the reflections from the time trace using special mathematical functions. Naftaly *et al.* have posited that this is ideally done by normalizing the signal and removing scaled copies of the main pulse convolved with the Dirac delta function,[64] however, due to phase mismatch originating from dispersion, every subsequent reflection after the main pulse will undergo temporal distortions away from the original pulse shape and therefore, will not be perfectly scaled copies of the main pulse.

Another common method in other types of Fourier transform spectroscopy is to employ the use of special window functions to remove unwanted reflections. The reflection removal process[§] typically involves the use of special mathematical functions, referred to as a window, that isolates the section to be removed and truncates that section of the signal. Popular windows include Hamming/Hanning, sigmoidal, square functions, ... *etc.*, however each have their own drawbacks. Whenever data is manipulated in post-processing, there is a risk of introducing artifacts that can give rise to erroneous features in the spectrum. Therefore, these window functions must be carefully chosen in order to mitigate major distortions in the resulting spectrum.

[§]This is often referred to as apodization in FTIR spectroscopy

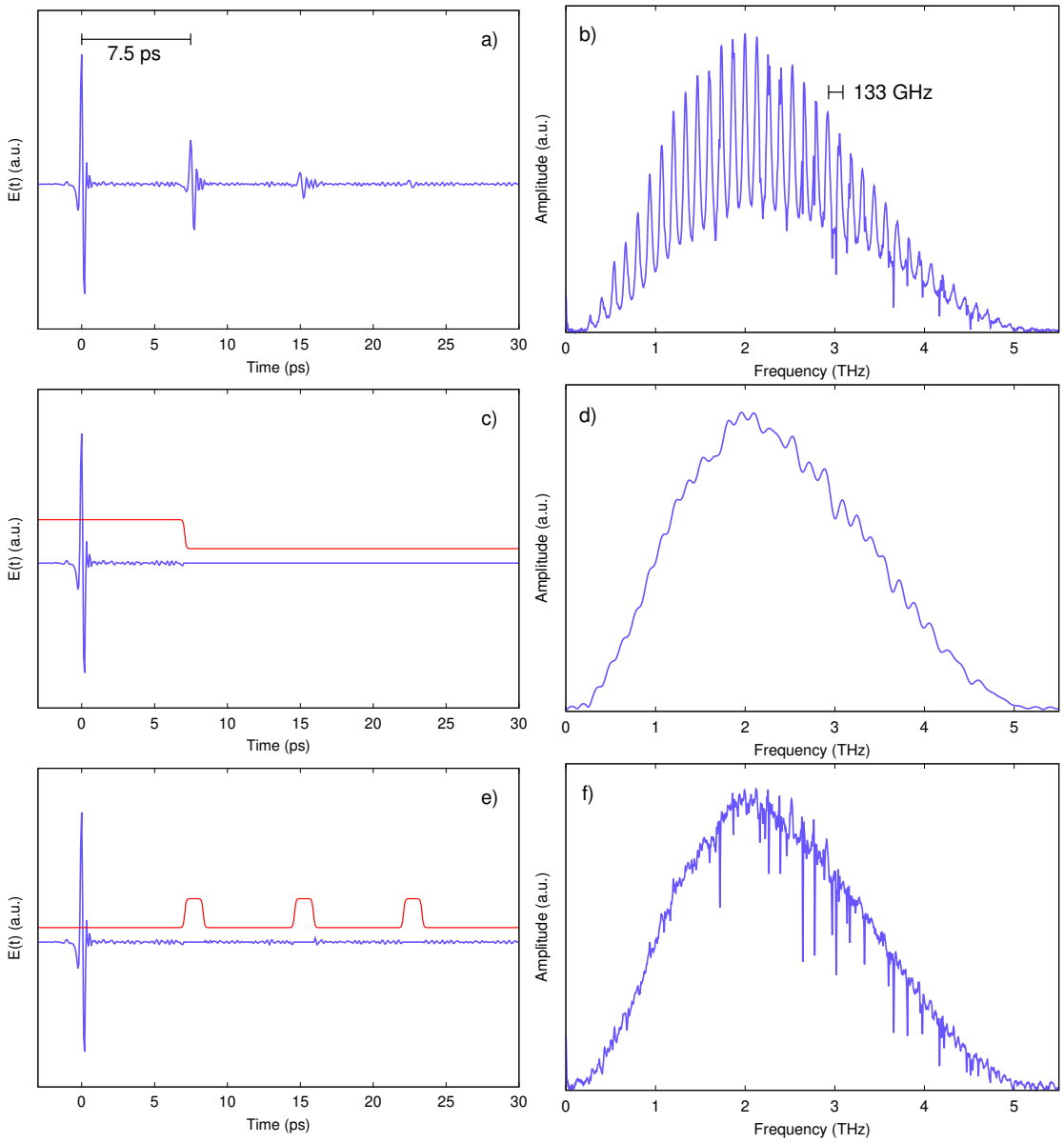

Figure 2.7: Top plots a) and b) show a 30 ps THz waveform displaying the first 3 internal reflections from the generation GaP as well as the spectrum of this waveform after Fourier transform. c) and d) show the same THz pulse with internal reflections removed using a sigmoid window centered around the main peak along with respective spectrum, and e) and f) show reflection removal using the same sigmoid window, now centered instead around individual reflections, along with the resulting spectrum.

Traditionally, window functions are often centered around the main pulse and trun-

cate all data that occurs after the beginning of the first reflection. This can be seen in the middle two plots in Fig. 2.7. However, when using a 0.3 mm GaP for generation and detection, this cannot be done without occluding all data occurring 7.5 ps after pulse due to the proximity of the first reflection to the main pulse. This leads to a serious reduction in resolving power even when zero padding is utilized. Instead, we can elect to use multiple smaller window functions centered around individual reflections in order for them to be removed. In this scenario, minimal data is lost in the reflection removal process, preserving the bulk of the spectral data collected in a scan. Moreover, the window size can be iteratively increased to accommodate pulse broadening through dispersive media, thus ensuring only the reflection data is removed.

The top plots in Fig. 2.7 shows a longer time trace which includes the three largest measurable reflections, as well as the spectrum after Fourier transform. Here we can easily see the FP fringes present in the spectrum. The middle plots show the effect of the reflection removal process when the sigmoid window function is centered around the main pulse. While the FP fringes have been removed, so to has the vast majority of spectral information present in the time trace. The bottom plots in Fig. 2.7 show reflection centered sigmoid windows. The accompanying spectrum now shows the FP fringes removed while preserving the high resolving power of the longer time trace.

The shape of the sigmoid window can be modified by changing function parameters, and therefore, a sigmoid window can be thought of as a customizable Hanning/Hamming window. By choosing appropriate parameters, one can tweak the size, shape, and offset of the window to ensure all reflections are appropriately handled. The sigmoid function is expressed as

$$\Lambda = \left(\frac{1}{1+e^{(-s(t-t_1))}}\right) \cdot \left(\frac{1}{1+e^{(s(t-t_2))}}\right) \tag{2.15}$$

where $t_{1,2}$ are the initial and final points to form the window around, respectively, and s is the steepness of the sigmoid transition. For small values of s the window appears Gaussian in nature, however as $s \to \infty$, Λ effectively becomes a unit box function. Examples of the sigmoid window with varying steepness parameters can be seen in Fig. 2.8.

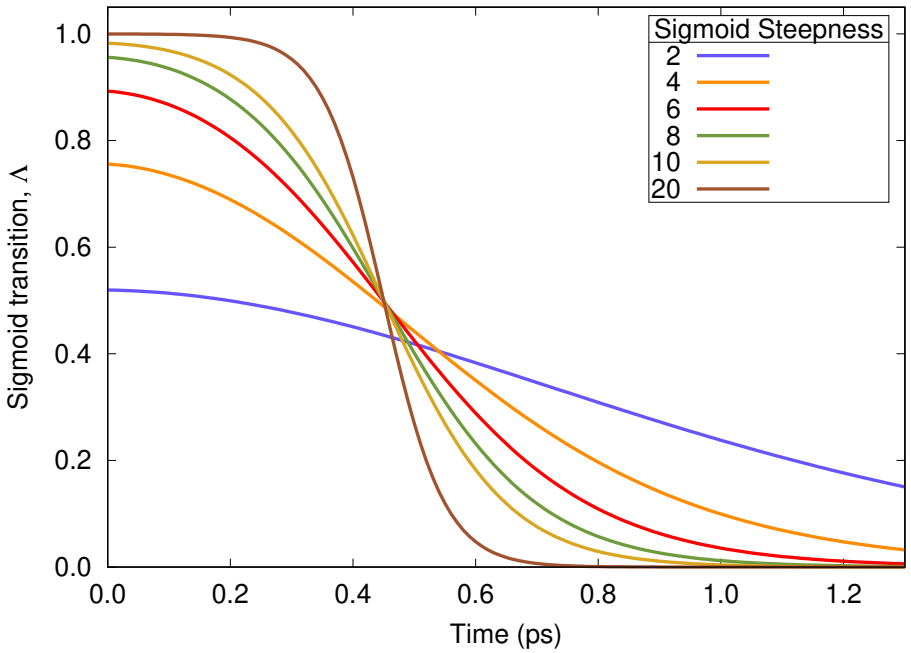

Figure 2.8: Shape of the sigmoid window transition with varying steepness parameter.

2.2 Attenuated Total Reflection

Having now discussed the generation and detection of THz light, as well as TDS signal collection and processing, we now turn to optical methods for mitigating absorptions from solvents and ambient humidity, as these can lead to erroneous absorptions that greatly impede characterization. Attenuated total reflection (ATR) is a technique commonly used in spectroscopy that allows incident EM radiation to be tangentially applied to a sample by passing the beam through a transparent prism on which the sample resides. Unlike other types of spectroscopy, EM radiation is not actually transmitted through the sample. Instead, the internal reflection of the beam at the top interface creates an evanescent wave that extends normal to the prism face. An example of a prism can be seen in Fig. 2.9, showing the geometry that allows for internal reflection of the transmitted beam and the resulting evanescent wave. The beam is attenuated when its frequency components are absorbed by a sample placed at the point of formation of the evanescent wave. This technique offers numerous advantages over transmission and reflection experiments, including the ability to scan samples that require little to

no preparation or in conditions that would not normally be permitted, such as in highly absorbing media. ATR has found use in IR spectroscopy for many decades and is a well established technique for evaluating samples in which transmission experiments are prohibited. A full, in-depth description of the technique can be found in Griffiths *Fourier Transform Infrared Spectrometry*.[65]

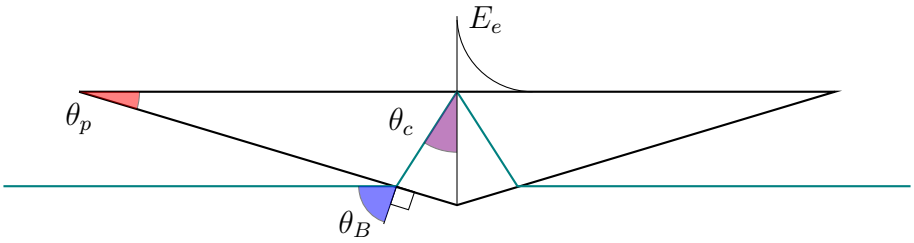

Figure 2.9: Cross-section of an ATR prism made out of HRFZ Si, showing important angles. With carefully chosen θ_p, the refracted beam will satisfy total internal reflection and become polarized.

As previously discussed, many polar solvents such as water have strong absorptions in the THz region due to polarization effects and hydrogen bonding between molecules. These absorptions can strongly attenuate the signal and prohibit transmission measurements as data of interest becomes overshadowed by the absorption peaks of the solvent. While there is great interest in understanding low energy phenomena in the liquid state, such as solvent cage interactions of photocatalytic species[66] or DNA interactions,[67] these require scans to be completed with the species of interest dissolved in appropriate solvents. Contamination from polar solvents in the resulting spectra greatly impedes characterization of these types of interactions. When these scans are performed using ATR, peak amplitudes of highly absorbing solvents reduce to the same scale as the analytes of interest. This reduction is due to the interaction of the beam with the sample being reduced from the volume of detection to the cross-sectional area of detection. While there are reports of the use of ATR in THz-TDS scans of organic species in water[68] and heavily carrier doped semiconductors,[69] these often use geometries which lead to ease of use rather than optimized for THz light.

The following subsections outline the theory of how the beam is internally reflected and the penetration depth of the resulting evanescent wave, as well as the optimization of prism geometry for THz light. With these advantages, an efficient model for ATR in the THz region is formed.

2.2.1 Evanescent Field and Penetration Depth

When a beam passes through an interface from an optically dense medium to an optically rare medium, the direction of the beam's propagation is refracted. Snell's law describes how the angle of the beam is altered at this interface as

$$\frac{\sin\theta_1}{\sin\theta_2} = \frac{n_2}{n_1} \tag{2.16}$$

where n_1 and n_2 are the refractive indices of the optically dense and rare media, respectively. The critical angle, θ_c, is defined as the angle in which the beam is refracted 90° to the normal of the interface and is written $\theta_c = \sin^{-1}(n_2/n_1)$. When the angle of incidence is greater than the critical angle, $\theta_i \geq \theta c$, the beam is said to be internally reflected. Fig. 2.10 shows how increasing the angle of incidence leads to internal reflection of the beam. If a beam undergoes internal reflection in a non-absorbing medium, there is no energy transfer as the beam is totally reflected and confined to the internal reflecting element. However, since the electric and magnetic fields of photons oscillate perpendicular to the direction of propagation, they can couple to surrounding environment just beyond the interface. This phenomena is known as an evanescent wave and is the basis for how ATR operates.

The term evanescent is used to describe something fading away. In this case, it refers to the exponential decay of the electric/magnetic fields that extend beyond the interface. If the electric field of the beam lies in the plane of incidence, also referred to as p-polarized, the electric field will be perpendicular to the the boundary and its evanescent field E_e will decays as

$$E_e = E_0 e^{z d_p} \tag{2.17}$$

for a beam propagating in the z direction. The penetration depth, d_p, of E_e into the sample is defined as the distance at which the exponential is equal to one, or when the field has decayed to $1/e$ of its surface intensity.[70] This depth is written as

$$d_P = \frac{\lambda}{2\pi n_1 \sqrt{\sin^2\theta_i - \left(\frac{n_2}{n_1}\right)^2}} \tag{2.18}$$

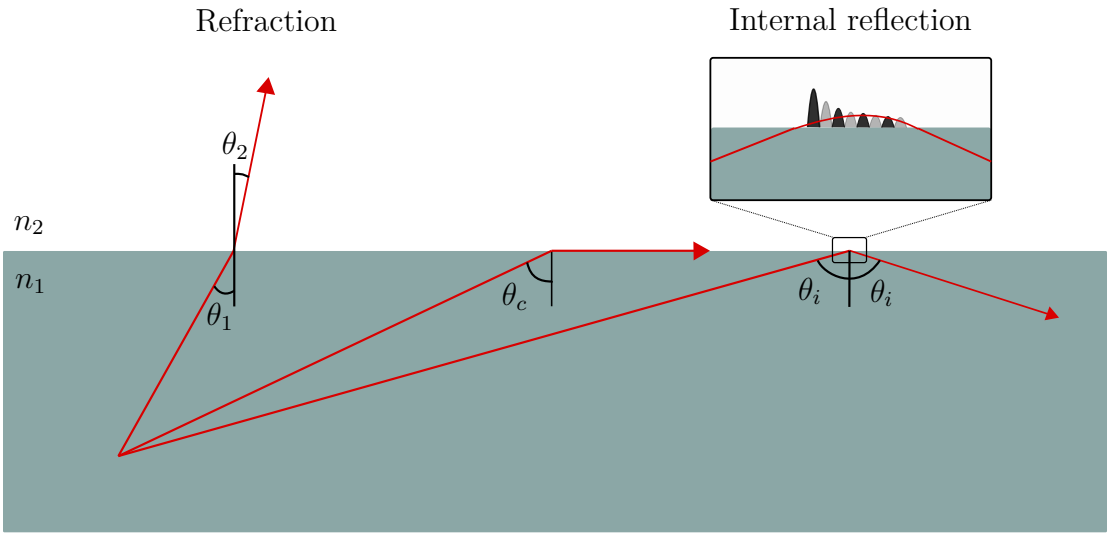

Figure 2.10: As light moves through the interface between two media with different indices of refraction, the beam is either refracted or internally reflected. The angle at which this occurs depends on the ratio of the refractive index of both materials as $\theta_c = \sin^{-1}\left(\frac{n_2}{n_1}\right)$. The inset image shows how total internal reflection leads to a non-uniform plane wave, as longer wavelengths penetrate further beyond the surface. Also shown here is the Goos-Hänchen shift which describes the lateral displacement of the point of reflection.

where λ is the wavelength in the denser medium, θ_i is the angle of incidence with respect to the normal of the interface, and $n_{1,2}$ refer to the index of refraction of the prism and the sample in which the evanescent field propagates, respectively. As equation 2.18 shows, the penetration depth of the evanescent wave into this material depends directly on the wavelength of light passing through. This leads to the generation of a non-uniform plane wave that occurs at the point of formation of the evanescent wave which propagates parallel along the interface as a surface wave with a polarization that matches that of the incident THz beam.[71]

Theoretically, one should be able to scan an area as small as the focal point within the diffraction limit, however, refraction and the Goos-Hänchen shift skew the minimum possible spot size. As previously discussed, refraction is the change of direction of the beams propagation and leads to divergence of the beam due to dispersion of different wavelengths, while the Goos-Hänchen shift is the lateral shift of the point of reflection at the boundary. As the light passes through the interface of the prism, the constituent wavelengths are refracted at different angles leading to a lateral smearing of the focus at the point of formation of the evanescent wave. This dispersion leads to a loss of

collimation and spread of wave vectors, $\vec{k}$, based on frequency.

The expanded portion of Fig. 2.10 shows how the lateral smearing of frequencies in the evanescent wave leads to a nonuniform plane wave, since d_p changes based on wavelength. While ATR spectra commonly resemble transmission spectra, it is important to note that longer wavelengths penetrate deeper into the sample, and therefore absorption bands at longer wavelengths are stronger than those at shorter wavelengths.[71] One interesting feature of the evanescent wave propagating as a plane wave along the interface of the prism is the change in selection rules available for coupling. When TE polarized light arrives as p-polarized, surface plasmon-polaritons are formed along the boundary, making it possible to access longitudinal modes that are normally prohibited in transmission experiments.[71]

Due to longer penetration depth of THz light, different configurations of ATR experiments can be utilized to allow for scanning to occur without contact of the sample. The Otto configuration refers to when the sample is in direct contact with the prism,[72,73] while the Kretschmann configuration refers to the inclusion of a dielectric gap between the sample and the prism,[74] usually in the form of an air gap. The presence of an air gap in the Kretschmann configuration allows for non-contact analysis and can also be used for tuning of the frequencies involved in the experiment based on the distance of the gap.[75]

2.2.2 Brewster's Angle Optimization

Internal reflection within the prism depends not only on the index of refraction of the prism, but also on that of the sample. Internal reflection can only occur when the sample has a lower index of refraction than that of the prism material. Subsequently, there is interest in using a material with a high index of refraction to construct the prism as this would allow for a much broader range of samples in which internal reflection is permitted. This becomes problematic however, as THz sources are often highly inefficient and reflective losses due to a high refractive index material can greatly reduce the power of the beam.

The Fresnel coefficients describe how light of different polarizations is reflected or transmitted at material interfaces. The reflection and transmission coefficients for s-

and p-polarization are written as

$$r_s = \frac{n_1 \cos\theta_1 - n_2 \cos\theta_2}{n_1 \cos\theta_1 + n_2 \cos\theta_2}; \quad t_s = 1 + r_s$$

$$r_p = \frac{n_1 \sec\theta_1 - n_2 \sec\theta_2}{n_1 \sec\theta_1 + n_2 \sec\theta_2}; \quad t_p = (1 + r_p)\frac{\cos\theta_1}{\cos\theta_2}$$

These coefficients give the ratio of the power of the beam that is transmitted or reflected as a function of the angle of incidence with respect to the optical axis. Fig. 2.11 shows the value of reflection power for p-polarized light versus angle of incidence for various candidate prism materials. As seen in Fig 2.11, each of these materials have a specific angle of incidence at which the reflected power is minimized. This angle depends on the materials index of refraction and is known as Brewster's angle.

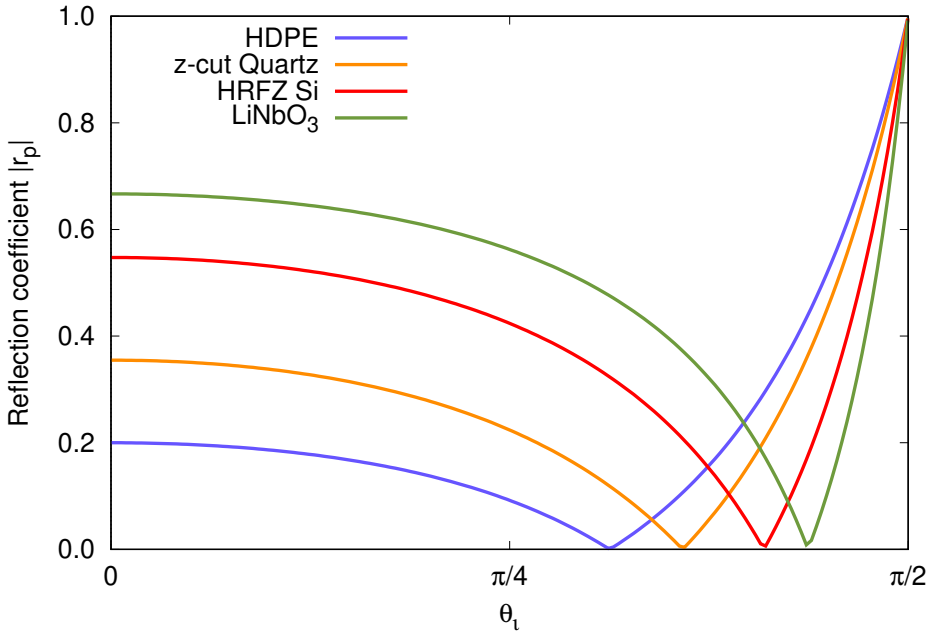

Figure 2.11: A plot of TE reflection r_p as a function of θ_i, showing p-polarized reflection for the interface of the materials in table 2.3 and air, with minimized reflected losses at Brewster's angle.

Many ATR designs implement a prism angle of 45° in an attempt to reduce changes in alignment due to refraction.[68,76,77,78,79] When the prism angle is set to 45° and the angle of incidence is 0°, $r = \frac{(n_1 - n_2)}{(n_1 + n_2)}$ and there is no refraction of the beam. If the internal reflection element is made out of a material with a low refractive index, such

as HDPE, the reflective loss at 45° is fairly minimal, about 1/5 of the incident power. However if the prism material has a high refractive index, such as $LiNbO_3$, the beam will lose roughly 2/3 of power to reflections. This is an important point since total internal reflection will only occur if the sample has a refractive index that is less than that of the prism. So, while reflection loss is minimal for prism material with low refractive index, so to is the number of samples one can scan, however, the reflective losses of a prism made out of a material with a refractive index are substantial. However, if the angle of the incident beam is set to Brewster's angle for a given prism material, the reflective losses will be minimized and the prism angle θ_p can be determined. For high-resistivity float-zone silicon (HRFZ Si), $n_{Si} = 3.42$, these angles are

$$\theta_c = \sin^{-1}\left(\frac{n_{air}}{n_{Si}}\right) = \sin^{-1}\left(\frac{1}{3.42}\right) = 17.02^\circ$$
$$\theta_B = \tan^{-1}\left(\frac{3.42}{1}\right) = 73.70^\circ$$
$$\theta_p = 90 - \theta_B = 16.30^\circ$$

Table 2.3 shows the index of refraction n_{THz}, critical angle θ_c, and resulting prism angle θ_p for different eligible prism materials.

Table 2.3: Indices of refraction for different candidate prism materials, along with the angles needed for prism geometry to satisfy both critical and Brewster's angles.

Material	n_{THz}	$\theta_c(^\circ)$	$\theta_p(^\circ)$
Teflon	1.4	46°	35.54
HDPE	1.55	40.18	32.83
z-cut Quartz	2.1	28.44	25.46
HRFZ Si	3.42	17.02	16.30
$LiNbO_3$	5	11.54	11.31

EOS is also highly sensitive to polarization, so it is beneficial to ensure the beam is polarized before scanning the sample and collecting the spectral data with EOS. A prism cut to Brewster's angle will act as a Brewster polarizer to the beam, and therefore ensure proper polarization of the beam for EOS. This also offers the advantage of allowing the choice of how the beams TE or TM polarization will couple to the prism interface by

simply rotating the prism 90° around the optical axis. Therefore, the selection rules can be easily manipulated by simple rotation of the prism.

The choice of prism angle such that incident light will arrive at Brewster's angle is advantageous with regard to penetration depth as well. For HRFZ Si cut to Brewster's angle ($\theta_i = 72.98°$), $d_p = 36.6$ μm and 9.14 μm for 1 THz and 4 THz (wavelengths 300 μm and 74.95 μm), respectively[¶]. At $\theta_i = 45°$, $d_p = 30.6$ μm and 7.66 μm for 1 THz and 4 THz, respectively. So with a prism cut to Brewster's angle, there is a 20% increase in penetration depth.

One consideration to be aware of is the attenuation of the beam through the prism. In selecting the prism angle θ_p it is necessary to weigh the difference between the advantage of Brewster's angle vs losses from attenuation through material. In most materials where Brewster's angle occurs at a prism angle, $\theta_p \leq \theta_c$, the path length of the beam through the prism is shorter than it would be at $\theta_p = 45°$, and therefore, the attenuation is reduced.

[¶]The penetration depth of 1 THz this is roughly the length of a human skin cell (30 μm), while average a4 printer paper thickness is approx. 100 μm

Real travel requires a maximum of unscheduled wandering, for there is no other way of discovering surprises and marvels, which, as I see it, is the only good reason for not staying at home.

Alan Watts

3 Experimental Methods

This chapter details the experimental design and physical parameters of the THz-TDS system constructed in this work, including the power calibration as compared to a commercial THz detector, as well as methods for determining instrument performance. The instrument was built in such a way that allows for measurements to be made with either collimated or focused THz light. One benefit of this setup is the ability to perform both transmission and ATR experiments without major modifications to the apparatus, thus facilitating rapid characterization of samples in different beam profiles.

3.1 Instrument Parameters

Time domain spectroscopy requires a time trace to be collected by comparing two separate beam paths within the instrument. The beam is initially split into two beams, the pump and probe, using a 90/10 beam splitter. The pump side of the beam utilizes a mechanical delay stage which changes the path length relative to that of the probe. This allows for the temporal scanning to be done with spatial stepping. The pump itself is never directly detected, instead the probe beam is steered to the detector and has its polarization modulated as it passes through the EOS crystal, which in turn has its

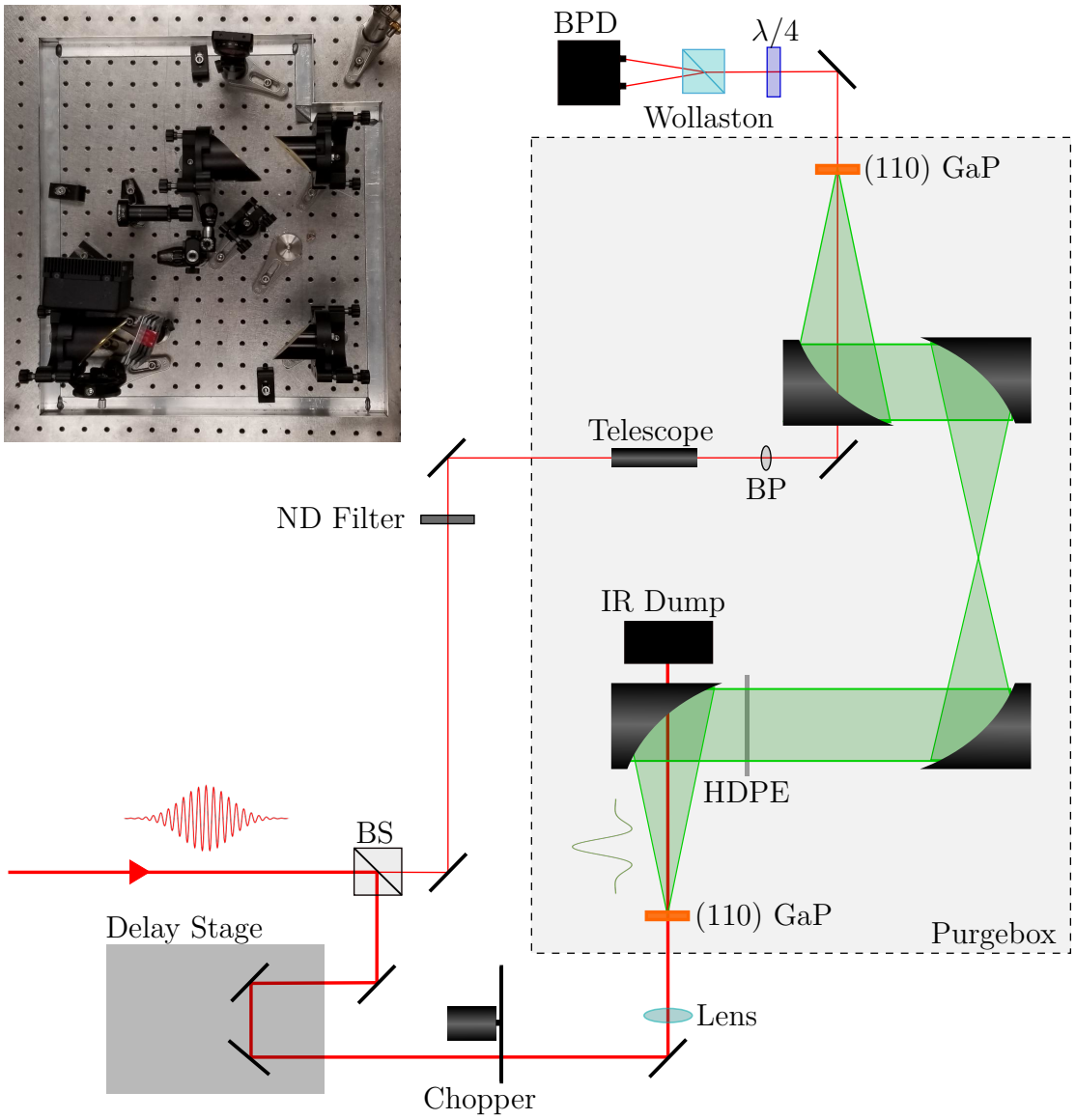

Figure 3.1: Diagram of the full THz-TDS spectrometer, with IR depicted as red rays and THz depicted by green. The beam is initially passed through a 90/10 beam splitter (BS) where the higher power beam (pump) goes on to generate the THz pulse, and the lower power beam (probe) is sent to the balanced photodetector (BPD). Before reaching the detector, the probe is first polarized with a Brewster polarizer (BP), and then steered through (110) GaP collinearly with the generated THz pulse which changes its polarization via the Pockels effect. It is this change in polarization that is ultimately measured. The THz section of the physical instrument can be seen in the top left corner.

birefringence altered through the application of incident THz EM radiation.

Fig. 3.1 depicts the THz-TDS apparatus designed and constructed for this work using the theory outlined in the previous chapter. A 1040 nm ytterbium-doped pulsed fibre laser (KMLabs Y-Fi HP) with 131 fs* pulse duration (FWHM NIR bandwidth 40 nm, 10 MHz repetition rate, 1 μJ pulse energy) illuminated a 0.3 mm thick (110) GaP crystal in order to generate THz through optical rectification. Detection was performed using an additional 0.3 mm GaP crystal to modulate the polarization of the probe through the electro-optic effect. The resulting changes in polarization were split into orthogonal components using a Wollaston prism (Thorlabs) and measured using a balanced photodetector (New Focus inc. Nirvana model 2007). The signal was demodulated using a lock-in detector (Stanford Research Systems Model SR830 DSP, 30 ms time constant, 997 Hz chopper frequency, 18dB roll off) and subsequently collected with a National Instruments USB 6212 DaQ.

On the pump side of the instrument, the generation GaP is placed at the focus of a 2 inch focal point off-axis parabolic (OAP) mirror, which collects and collimates the THz light. After collimation, a 1 mm thick piece of PTFE set to Brewster's angle acts as a Brewster's polarizer as well as a filter to remove any stray IR light. The THz beam is subsequently steered to another 4 inch focal point OAP mirror which focuses the light before sending it to another OAP mirror, recollimating the light. Finally, another OAP mirror with a through-hole focuses the THz onto the detection GaP while also passing through the probe beam collinearly through the detection crystal.

3.1.1 Power Calibration

In order to calibrate the instrument, the beam power measured by EOS must be compared to a known detector. Power is defined as

$$P = \int I \cdot dA = \int E^2 \cdot dA \tag{3.1}$$

where I, A, and E are intensity, area, and electric field strength, respectively. In this work, the THz power was measured with a homemade far IR detector that had been calibrated against a commercial THz power meter (Gentec THZ5B-BL-DZ-D0). An

*This value has been confirmed via FROG measurements from the KM Labs performance report.

example of the focused THz beam captured with a 32x32 pixel thermopile IR camera (Heimann HTPA32x32d) can be seen in Fig. 3.2. The aperture of this camera was 2.6 mm, indicating the FWHM of the beam is roughly 0.5 mm, which is close to the diffraction limit of ∼0.3 mm. Also shown in this figure is a plot of the normalized THz intensity signal vs average laser power. Using values collected with the calibrated detector, the average THz power was determined to be 27.5 μW (3.05×10^{-6} conversion efficiency). This value can then be compared to the power calculated from EOS.

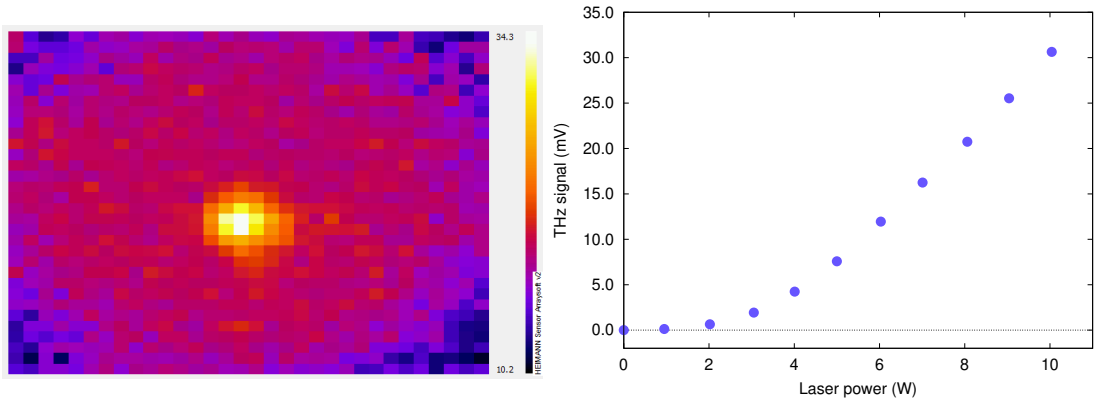

Figure 3.2: Left: Beam profile of the first THz focus where the sample resides, collected with 32x32 pixel infrared thermopile array. The aperture size of the camera is 2.6 mm, indicating FWHM $\leq$ 0.5 mm, while the beam power was measured to be roughly 27.5 μW. Right: the normalized THz intensity signal as measured by BPD vs the incident laser power.

EO electric field strength measured by the BPD signal is due to the EO effect,[42,80] where the EO induced ellipticity of the beam is detected after the incoming beam is split into two perpendicularly polarized beams. The signal $S(t) = \Delta I/I_0 = (I_x - I_y)/(I_x + I_y)$ is the normalized difference in intensity measured by BPD. This ratio is a direct measure of the ellipticity of the beam and is recorded as a function of the temporal delay between the THz and the probe.[49]

Since the THz electric field strength is proportional to the phase delay $\Delta\phi$ seen by the photodiodes, the signal can be related to the electric field as a function of the response of the detection crystal, $\Delta I/I_0 \propto \Delta\phi$. Jepsen *et al.* have reported that the phase delay of the horizontally polarized component of the beam is[81]

$$\Delta\phi = \sin\left(\frac{2\pi n_{GaP}^3 r_{41} t_{GaP} E_{THz} L}{\lambda_0}\right) \approx \frac{2\pi n_{GaP}^3 r_{41} t_{GaP} E_{THz} L}{\lambda_0} \tag{3.2}$$

where $n_{GaP} = 3.34$ is the index of refraction of GaP at 1040 nm,[62] $r_{41} = 0.88$ pm/V is the EO coefficient of GaP,[82] $L = 0.3$ mm, and $\lambda_0 = 1040$ nm. Here t_{GaP} has been included to account for transmission losses at the EO crystal face and is calculated from Fresnel coefficient at normal incidence ($t_{GaP} = 0.46$). Since r_{41} is so small, equation 3.2 can be simplified using the small angle approximation. Therefore, $E_{THz} = \beta_\phi \times \Delta I/I_0$, where

$$\beta_\phi = \frac{\lambda_0}{2\pi n_0^3 r_{41} t_{GaP} L} \tag{3.3}$$

For 0.3 mm thick GaP with normal incidence $\beta_\phi = 365.8$ kV/cm. This leads to a peak electric field strength of $E_{THz} = 1.15$ kV/cm within the GaP for signals on the order of 40 mV. This, however, is the instantaneous power at the peak of the pulse and in order to find the full THz power to compare to the calibrated detector one would need to integrate over time. Equation 3.1 then becomes

$$\int\int E^2 \cdot dAdt = \int_0^{2\pi} dA \cdot \int_{t_1}^{t_2} \left(\beta_\phi \times \frac{\Delta I}{I}\right)^2 dt \tag{3.4}$$

relating the two detection methods. Given that the area of detection on the EO crystal does not vary with time, the first integral becomes a constant and is equal to the FWHM of the THz beam on the EO crystal. Taking the area of detection of the FWHM to be 0.4 mm^2, the second integral in equation 3.4 can be calculated over the time trace. The power calculated by EOS with this method is equal to 19.9 μW, however since the fraction of the Gaussian beam profile contained within the FWHM is 0.76, the total adjusted beam power becomes 26.3 μW.[†] Comparing the two methods of power measurements shows that they are close in value, within 95%.

3.1.2 Signal-to-Noise and Dynamic Range

Noise is an ever present obstacle when detecting low power signals. When collecting spectral data for samples it is important to mitigate noise, as it is quite often easier to reduce noise than it is to increase signal power. Sources of noise can be attributed to the variation in laser stability,[58] fluctuations in air currents, or even vibrations present

[†]The calibrated detector sensor is square and has an area of 0.51 mm^2, therefore calibrated power measurement is actually overestimated compared to circular EOS signal by $a^2 - (a/2)^2\pi = 1 - \pi/4$.

in the optics table itself. Of these, changes in the laser spectrum over time quite often lead to the largest variations in the resulting spectra. Fig 3.3 shows two different reference scans taken approximately 5 hours apart. The increase in amplitude of the THz spectrum can be attributed to the fluctuations in laser power as well as drifting of the spectral content. These changes and the resulting effect on the THz spectrum are expanded upon in Appendix A. Since it is impossible to avoid variations between scans, it is useful to average over numerous scans. In Gaussian statistics, variability is proportional to $1/\sqrt{N}$, and therefore the easiest way to reduce errors is to increase N. This is done by averaging over many scans, sometimes as many as 100s or 1000s.

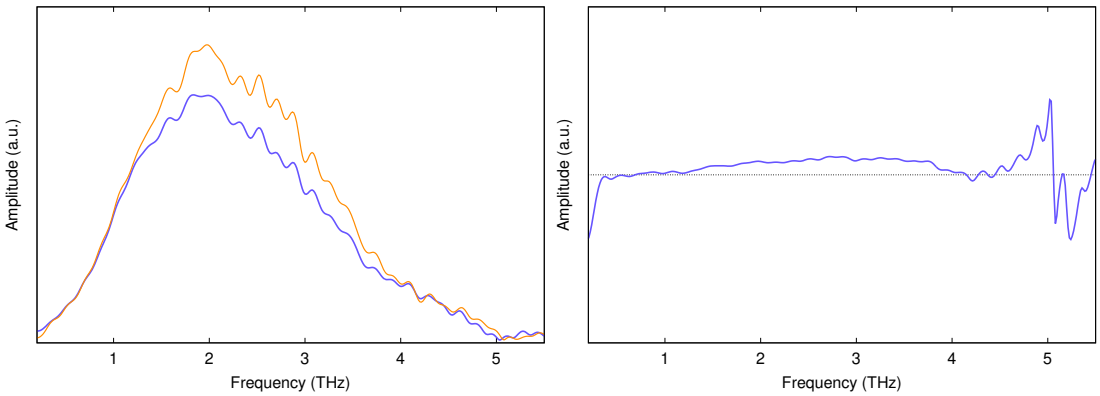

Figure 3.3: The plot on the left shows two reference scans taken ∼5 hours apart. The plot on the left shows the changes in the resulting absorption spectra due to drifting in laser power and spectral content.

Two useful metrics in determining instrument performance are the signal-to-noise ratio (SNR) and the dynamic range (DR). While these quantities are distinct, both of these values relate how the instrument's signal is distinct from the background variability in two subtly different ways. SNR measures the minimum quantifiable signal and is the ratio of mean peak signal over the standard deviation of the peak between scans, while DR indicates the maximum detectable signal and is the ratio of peak signal to the standard deviation of the background noise.[83] Formally written, these take the form

$$SNR = \frac{\bar{E}}{\sqrt{\frac{1}{N}\sum_{i=1}^{N}(x_i - \mu_{peak})}} \tag{3.5}$$

$$DR = \frac{E_{peak}}{\sqrt{\frac{1}{N}\sum_{i=1}^{N}(x_i - \mu_{noise})}} \tag{3.6}$$

where $\mu_{peak,noise}$ are the mean values of the peak and noise, respectively. Table 3.1 contains the maximum SNR and DR values for both domains. It should be noted that, while there is a single peak electric field point in the time domain, the frequency spectrum does not contain a single corresponding point. Unfortunately, there is no concise analytical way to relate SNR and DR from the time domain to the frequency domain,[83] therefore these values need to be calculated for each domain independently. This leads to a strong frequency dependence for the SNR, as can be seen in Fig. 3.4. Interestingly, here we see that the highest SNR value in the time trace occurs during the first FP reflection instead of during the main pulse. This can be attributed to how rapidly the signal changes during the collection of the main pulse. Any slight spatial deviation caused by the delay stage can lead to a significant variation between scans.

Table 3.1: The maximum SNR and DR values for both time and frequency domains for a typical reference scan, averaged over 5 scans.

	Time	Frequency
SNR	173	307
DR	579	412

As stated above, one way of reducing noise in the data is to average over multiple scans. This can be done in either the time domain or frequency domain by averaging the time trace or by averaging the resulting spectra after Fourier transformation. The quality of the delay line has a direct correlation to the quality of the spectra that can be obtained from the instrument. If the delay line has significant backlash, this can lead to slight broadening in the pulse, and subsequent variation in low frequency data.[83] This effect can be seen in Fig. 3.5. Shown here are two spectra, one produced from data that had been averaged in the time domain and one that had been averaged in the frequency domain. Overlayed on these is the ratio between time averaged data and frequency averaged data, clearly showing the advantage of time averaging for resolving low frequency features and reducing noise in this instrument.

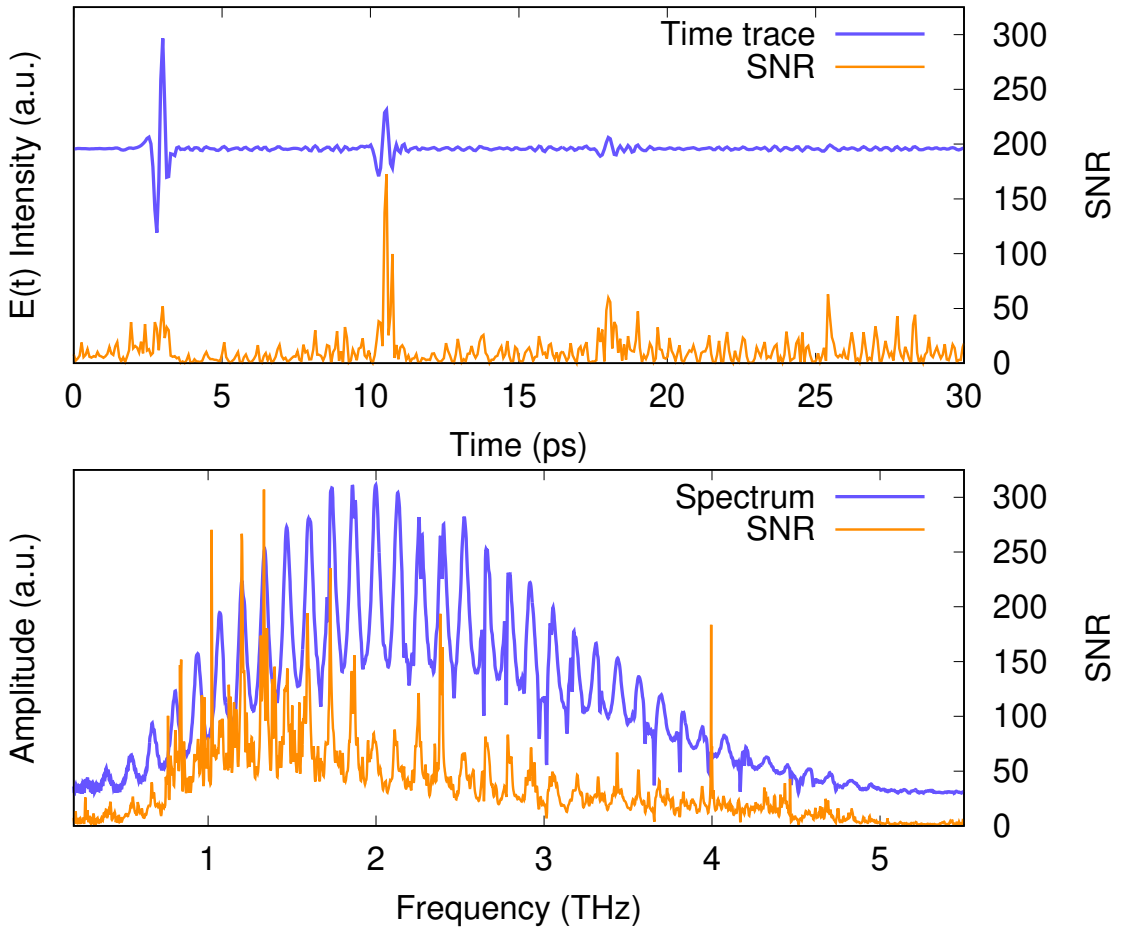

Figure 3.4: Top: The THz time trace with calculated SNR. Bottom: The resulting spectrum from above time trace with associated SNR, showing the frequency dependence of the SNR.

3.2 Sample Preparation and Data Analysis

All of the samples collected in this work are reported in absorbance (a.u.) rather than percent transmission (%T) or absorption coefficient (m^{-1}). While absorption measurements can yield more information ($n + i\kappa$) about the sample of interest, it requires accurate knowledge the interaction volume of the beam through the sample which can be difficult to gauge with mixed powder pellets or in ATR experiments. It should be noted however, that absorbance, unlike the absorption coefficient, includes information not only about physical absorption events, but also attenuation of the light by the sample

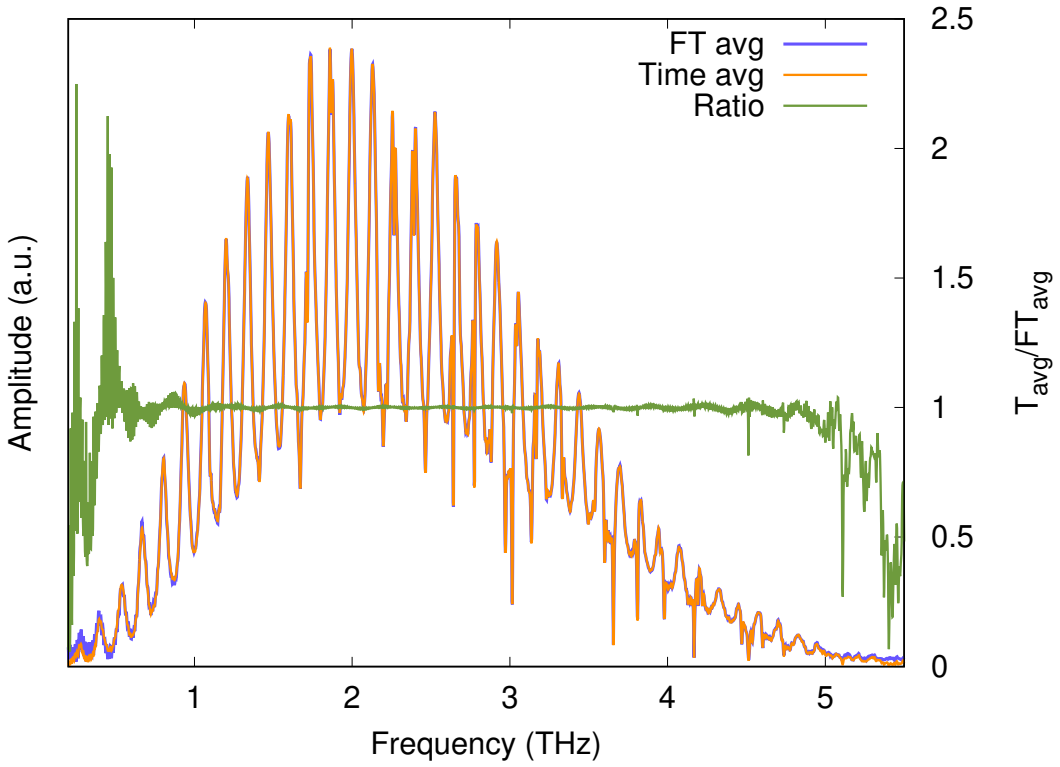

Figure 3.5: This plot depicts the difference between averaging in the time domain versus averaging in the frequency domain. Time domain averaging aids in resolving low frequency features and reducing noise, as can be seen in the ratio between time averaged and FT averaged spectra overlayed on the plot.

from additional processes such as scattering (*eg.*, Mie scattering). Absorbance is defined as the negative logarithm of the ratio of transmitted intensities, and is calculated by comparing the sample spectrum with a reference spectrum ideally taken immediately before or after the sample spectra is collected. This is to prevent erroneous features arising from variations of the environment or from stability of the laser. Absorbance is written as

$$A = -\log\left(\frac{I_{samp}}{I_{ref}}\right) \tag{3.7}$$

where $I_{samp,ref}$ are the intensities of the sample and reference spectra, respectively. The use of absorbance is beneficial over using %T in that it makes small features much easier to distinguish.

Given that absorbance is directly calculated from the ratio of intensities, the unit most

often given for these measurements is that of arbitrary units (a.u.). This unit is what will be used henceforth in this work. Although it is possible to calculate these values in decibels (dB), this is, by definition, only a factor of 10 different then a.u., since dB $\equiv -10\log_{10}(I_{samp}/I_{ref})$. The use of dB is convenient when exact path lengths of the beam through the sample are known as it can yield dB/m which is useful in communications devices, however, the use of a.u. is perfectly adequate when qualitatively analyzing materials in spectroscopy.

3.2.1 Transmission Scans

Transmission experiments describe when the THz light is passed directly through a sample, as can be seen in Fig. 3.6. Here is it possible to see the free induction decay (FID) occurring directly after the main pulse that has been transmitted through a sample. The presence of FID arises from the excitation of some fundamental process in the sample emitting THz light after the pulse has passed. The spectral content of this FID contains information about these processes and is extracted during the Fourier transform. One caveat to consider when attempting transmission scans is the generation of additional surface reflections caused by the sample that are not attributed to the instrument itself.

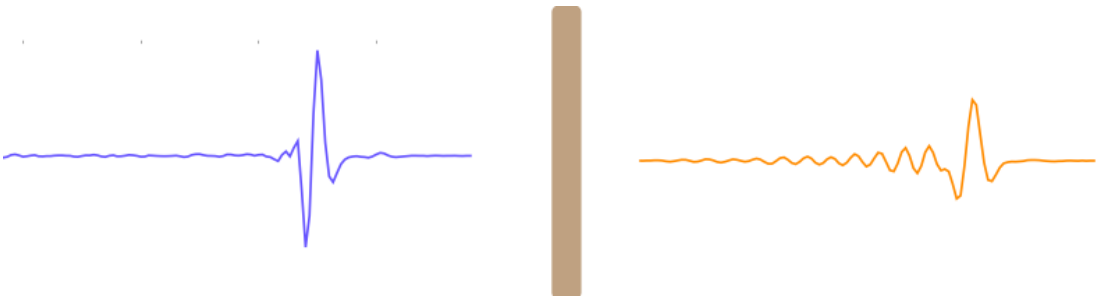

Figure 3.6: An example of the reference pulse compared to the same pulse having been transmitted through $BiFeO_3$, showing the free induction decay of the pulse.

As discussed in the previous chapter, FP etalons are a troublesome hurdle in generating clean sample spectra. If either the sample or the mounting substrate are thicker than the wavelength of the highest frequency, internal reflections can occur at these interfaces and therefore create FP fringes in the spectra. If the substrate is thick enough to

cause reflections, the reference spectrum can be taken with the substrate present, which will remove substrate reflections with the removal of the reference spectrum. However, reflections from the sample cannot be accounted for in the reference and can still lead to FP fringes. There are two main avenues for removing sample reflections. First, the previously mentioned window functions can be utilized to remove the reflections from the time trace, however this leads to potential artifacts being formed and sample data being lost. The second way is to use powdered samples which can lead to diffuse scattering of the beam and therefore, no measurable reflections. If the sample is placed in the Rayleigh range of the beams focal point, the THz radiation acts as a plane wave and most of the diffusely scattered light can be collected and recollimated with an OAP mirror. Residual artifacts can still occur due to noise and other variations of the laser though. Such artifacts can arise from local changes in humidity and subsequent changes in the index of refraction of the air the IR beam passes through.

Transmission samples scanned in this work were mounted on 18±2 μm thick polyolefin film, which is significantly thinner than the highest frequency wavelength of 5 THz. All sample spectra collected were compared to a reference scan collected with the polyolefin film present. This allows for the absorption power to be calculated without the need to remove FP reflections, provided the sample does not introduce any additional reflections that are not present in the reference scan.

3.2.2 ATR Scans

A prototype Brewster's angle ATR prism was initially cut out of a 1 mm thick HRFZ Si wafer. This prism was used to confirm the ability of HRFZ Si to be used as a satisfactory material for the construction of the ATR prism. The time trace with and without the prototype prism can be seen in Fig. 3.7, showing the delay of the main pulse by roughly 17 ps which confirms a path length of 1.5 mm using equation 2.14. Fig. 3.7 also shows that, although the prism appears to work, it does not adequately capture the full beam, as indicated by the presence of the main pulse at 0 ps. Therefore, a larger HRFZ Si prism was fabricated from HRFZ Si stock (BATOP GmbH). Images of cutting the prism and subsequent polishing can be seen in the right and middle images of Fig 3.8. The prism was cut to a geometry that allows for all incoming THz light to be captured, and polished to $<\lambda/4$ for 5 THz. The prism was then mounted in a 3 axis stage to allow for

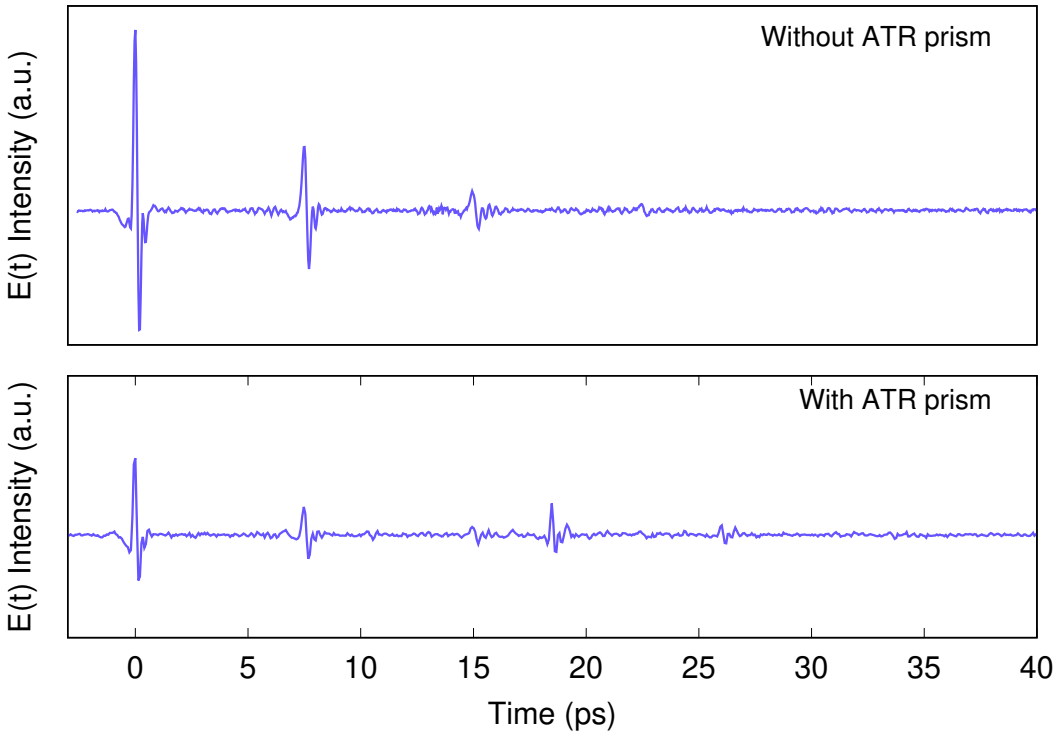

Figure 3.7: A plot of the waveform of the ATR signal. The main THz pulse can be seen at 0 ps, with 3 etalon modes successively occurring every 7.5 ps. A smaller, inverted copy of the main pulse occurring at 17 ps is the ATR signal. A delay of 17 ps corresponds to a path length of 1.5 mm through the HR Si prism ($n_{Si} = 3.42$)

fine manipulation, as can be seen in the image on the right in Fig. 3.8

Figure 3.8: A series of images showing the fabrication of the ATR prism. The image on the left shows the prism being cut from a block of HRFZ Si, while the middle image shows polishing of the prism. The image on the right shows final prism mounted in a 3 axis stage.

ATR also allows for the prism to be built into the side of the purgebox, meaning that

samples can be exchanged without introducing ambient humid air into the instrument. As previously stated, this instrument has the additional advantage of allowing for both transmission and ATR experiments to be run in either focused or collimated light. When using an ATR prism cut the Brewster's angle, experiments have the inherent benefit of the internal reflecting element acting as a Brewster polarizer, which is beneficial for EOS. Having the ability to polarize the THz before collecting a sample spectrum also allows for the selection between electric or magnetic coupling with a sample by choosing whether TE or TM polarized light arrives as p-polarized.

3.3 Humidity and Inert Gas Purging

One pervasive obstacle in generating a clean THz spectra for analysis is that of ambient atmospheric humidity. Due to strong THz absorptions by water vapour, not only is the overall signal intensity reduced, but there exists numerous absorption peaks not attributed to any sample, which can lead difficulty or even inability to interpret the sample spectra. Fig. 3.9 a) shows multiple THz spectra with varying values of relative humidity (R_H) from 20% down to 0% measured with the GaP spectrometer constructed in this work, along with the absorbance spectrum of water in Fig. 3.9 c). Absorptions from water vapour between 0.5 - 2.4 THz have been identified by Xin *et al.* to largely be a mixture of rotational modes of ortho- and para-configurations in water monomers, as well as hydrogen bonding between dimers and trimers.[84] There are hundreds of absorptions due to water vibrations and rotations that are known to be present in the THz region.[32]

Normal operating procedure for analyzing the spectrum of a sample requires the initial collection of a background spectrum of the instrument for reference. This reference spectrum can then be removed from the sample spectrum as I_{samp}/I_{ref}, however, the presence of large water peaks will not be accounted for if the $\%R_H$ has changed between the reference and the sample. Dividing out the reference scan removes reflections better than windowing, and can account for water vapour present in the scan, provided the humidity during the sample scan is consistent with the reference. Minor changes in humidity between scans can lead to the presence of strongly absorbing erroneous peaks in the resulting spectra. In order to combat this, an aluminum inert gas purgebox was constructed around the THz beam path that allows dry N_2 gas to be pumped in

to displace any humid air. The purgebox is equipped with a humidity sensor (Bosch BME280) that ensures scans will only start if the purgebox humidity is below a set threshold. All experiments in this work were collected with $1.0 \pm 0.1\%$ R_H at 19°C.

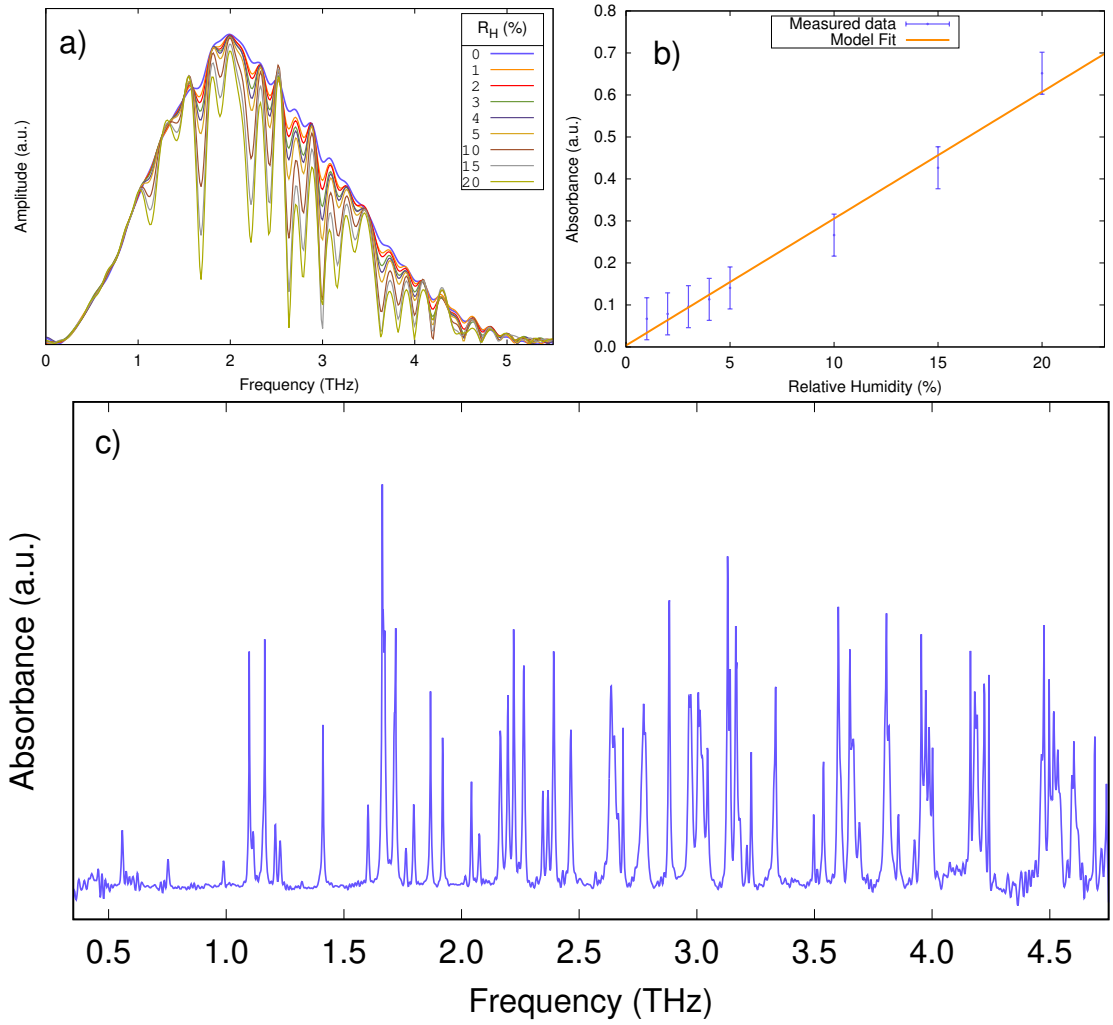

Figure 3.9: Top: a) shows THz spectra with relative humidity varying from 20% down to 0%, while b) shows how the absorbance of the peak at 1.68 THz changes with relative humidity. Bottom: c) shows the absorbance spectra of ambient humidity (R_H = 20%).

The plot in Fig. 3.9 b) shows how the water absorption peak at 1.683 THz changes with R_H, which allows for the absorbance due to humidity to be calibrated. The model fit of this data is $y = 0.0302x + 0.0036$. Given that the absorbance should be zero when

there is no water vapour present, the 0.0036 offset is likely due to slight underestimation of the humidity measured by the sensor, and can considered zero. Knowing this absorbance calibration can allow one to gauge how much water vapour contamination is present in the sample spectra.

One interesting advantage in having water vapour absorptions present in the sample spectrum is that it can be used as an internal standard in determining the amount of sample interacting with the beam, provided the humidity level in accurately known. If a sample with a known interaction volume is scanned in the presence of water vapour, the ratio of absorbance between water peaks and sample peaks can then be used to facilitate gauging the amount of material present in unknown samples or in heterogeneous mixtures. This can be useful for measuring water content in food and minerals,[85] or in determining small traces of samples of interest.

It is also possible to detect the humidity level using Beer's law and the ideal gas law.[18] Using Beer's law, the absorbance can be related to the concentration of water vapour in the air, c, as

$$A = -log_{10}\left(\frac{I_s}{I_0}\right) = \epsilon c \ell \tag{3.8}$$

where ϵ is attenuation coefficient[‡], and $\ell = 610$ mm is the path length of the THz beam. Since $c = n/V = A/\epsilon\ell$, the ideal gas law $PV = nRT$ can be rewritten and equated to the absorbance due to R_H through the linear fit from Fig. 3.9 b),

$$\frac{P}{RT} = \frac{0.302 R_H}{\epsilon \ell} \tag{3.9}$$

which now relates the absorption of water vapour to the ambient conditions in the lab. This can be rearranged to give relative humidity as a function of pressure P and temperature T

$$R_H(P,T) = \frac{\epsilon \ell}{0.302 R}\frac{P}{T} \tag{3.10}$$

where $R_H(P,T)$ is linearly related to P/T by the constant $\epsilon\ell/0.302R$.

[‡]This is also commonly referred to as the molar absorptivity, however this name is discouraged by IUPAC.

There are two possible outcomes: if the result confirms the hypothesis, then you've made a measurement. If the result is contrary to the hypothesis, then you've made a discovery.

Enrico Fermi

4

Material Characterization Using THz-TDS

Having now outlined the theory behind THz-TDS as well as the experimental apparatus that has been constructed, the capability of the instrument needs to be tested to show that it is able to scan samples of interest. The development of this instrument was based around the need to characterize magnetic compounds suited for spintronics applications, however the development of an optimized ATR prism now extends the range of samples that the instrument is able to scan to include polar liquids, solutions, and highly absorbing media. The following sections show how the THz-TD spectrometer described in the previous chapters lends itself to the study of two distinct classes of materials, namely magnetic metal oxides and chiral organic species. These two series of measurements provide a host of low energy phenomena that make them prime candidates for future technologies and therefore, are a good starting point for testing the instrument.

The spectrometer was used to analyze numerous nanoparticle, bulk powder, organic molecule samples with the goal of supporting research efforts focused on nanoparticle

growth, development of solid state fuel cells, and in demonstrating the power of ATR spectroscopy as a characterization tool for differentiation isomeric species. The following sections give a detailed effort in using THz-TDS as a means to elucidate details of low energy interactions from specific categories of materials of interest. The compounds found in these sections were chosen as important samples that stuck out during these endeavours.

As mentioned in the previous chapter, the SNR of THz spectrometers frequently requires averaging over many scans in order to reduce noise in the spectra. This is especially true when attempting to pick out features that are not strongly absorbing. In order to expedite the discovery of materials that exhibit useful low energy features, there is a need for the creation of methods for rapid characterization of samples to facilitate the research process. Therefore, it is pertinent to be able to collect scans with minimal time spent on changing samples and purging. Some of these samples, largely those found in Appendix C, were chosen in order to test the high throughput capability of the apparatus and to provide reference scans for comparison to similar samples.

4.1 Magnetic Metal Oxides

Transition metal oxides (TMOs) offer a simple, yet effective class to start with as these are commonly used in many types of solid state devices and offer a rich array of low energy phenomena to study at THz energies. Certain minerals have been known since antiquity to have special properties that have been utilized to advance our technologies, such as the ferromagnetism displayed by magnetite (Fe_3O_4) and the development of the magnetic compass. TMOs give rise to many different interesting phenomena due to the vast array of possible crystal structures and electron configurations they can take, which are both largely attributed to the presence of d- and f-electrons.[87] It is now known that ferromagnetism is predominantly due to unpaired electrons in partially filled orbitals, while other phenomena like ferroelectricity originate from the presence of a permanent electric dipole moment that arises from distorted (usually perovskite) lattice geometry. Recently, phenomena such as giant magnetoresistance, which won the 2007 Nobel prize in physics,[88] and high temperature superconductivity have renewed research interest in pure and mixed metal oxides.

TMOs have found use in numerous different fields and have proven to offer plenty of

different properties of interest, notably those that lead to the presence of quasiparticles. Landau first conceptually introduced the idea of quasiparticles in the form of phonons and rotons in 1941.[89] Since then, many new types of collective excitations have been defined. This includes those that emerge from ensembles of individual particles, such as the complex magnetic ordering of magnons/skyrmions and local electron resonance of plasmons, or the coupling between different particles like that of electron-phonon coupling (polarons) or electron-photon coupling (polaritons). Many of these structures have fundamental frequencies in the THz range,[90] as can be seen in Fig. 1.1. These properties have allowed for numerous new applications and have paved the way for technologies such as computational elements and solid state fuel storage.

This section shows how THz-TDS can be used to detect low energy phenomena such as (electro-)magnons, phonon-polaritons, and lattice dynamics/non-covalent interactions in various different metal oxides. While this section details numerous distinct samples, not all samples that were scanned are included for the sake of brevity. Appendix C contains the spectra of all the TMO samples that were scanned during this work. All samples in this section were measured using transmission spectroscopy. Samples were prepared by pulverizing the oxides into fine powders then creating a slurry with isopropanol and depositing ∼5-10 mg onto polyolefin film. The film was included in all reference scans, although it is sufficiently thin and has a low enough index of refraction that there was no detectable internal reflection.

4.1.1 Multiferroics

The term multiferroic refers to materials that exhibit two or more properties that are considered *ferroic* (*e.g.*, ferroelectric, ferromagnetic, ferroelastic, *etc.*). These materials are purported to offer marked technological advantages to devices that combine electric and magnetic properties, such as spintronics[27] and data storage devices.[91] The disadvantage of this class of materials is that it is still relatively new and there is much work still needed to fully understand why these properties coexist.

Multiferroics can be classified into two main groups: type I and type II. Type I refers to materials that have their magnetism and ferroelectricity occurring at different temperatures and phases, and emerge from largely different mechanisms that are independent of each other. Type II describes materials in which the magnetic ordering breaks inver-

sion symmetry and leads to the presence of ferroelectricity. The ferroelectric phase in distorted perovskites can arise from different sources that form the required permanent dipole moment, including lone pair, geometric, and charge ordered distortions.[92] The multiferroic class is often extended to include non-primary types magnetic order, *i.e.*, antiferromagnetic or ferrimagnetic order, which leads to the inclusion of the coupling between magnetic and electric properties, also known as the magnetoelectric effect.

Unfortunately, materials that exhibit both magnetism and ferroelectricity are rare. This is due to the fact that, to date, all conventional ferroelectric perovskite oxides have d^0 electron configurations located at their B-sites[93] which leads to the distorted geometry that gives rise to their electric dipole moment.[94] Magnetism, on the other hand, requires the presence of partially filled orbitals. So, while these properties are not mutually exclusive, they are often inhibited by local chemistry.

Although multiferroics are uncommon, there is great interest in discovering and characterizing new multiferroics as this can lead to the creation of devices that are able to operate at THz frequencies. This is especially important when creating logical devices using antiferromagnets as these materials have resonance frequencies much higher than traditional ferrite ferromagnets[111] and can facilitate spin currents through otherwise insulating materials. Devices made with these properties can utilize the Rashba effect, which describes the loss of electron degeneracy in materials that lack inversion symmetry due to asymmetrical spin-orbit coupling. This means that systems with a Rashba term in the Hamiltonian allow for direct electric manipulation of electrons spins without the presence of a magnetic field. It should be noted however, that the Rashba effect only exists in materials that lack inversion symmetry, *e.g.*, material with noncentrosymmetric symmetry or in a 2D plane such as heterostructures or the surface boundary of a material.[95]

The following subsections explore numerous multiferroic compounds and attempt to use THz-TDS in order to examine low energy magnetic interactions. Initially we investigate $BiFeO_3$, a multiferroic with known interactions in the THz region that has previously been characterized in this lab with a similar, albeit lower bandwidth techniques.[37,101] Next we explore the first material predicted to have coexisting ferromagnetic and ferroelectric properties, Cr_2O_3, as well as another known multiferroic, CuO. Following this, we analyze ϵ-Fe_2O_3 nanoparticles which have been reported to have potential use in high frequency communications devices. The last two compounds are

TMO samples proposed for solid state fuel storage through oxygen capture in fluorite-like superstructures. With this, the research conducted for this thesis shows that THz-TDS can be used as a way of characterizing materials that are of interest for current technologies.

Bismuth Ferrite

Bismuth Ferrite ($BiFeO_3$, or BFO) is a lone pair distorted multiferroic perovskite with a rhombohedral structure of the $R\bar{3}c$ space group. It is a G-type helical antiferromagnet with $T_C \approx 1100K$, $T_N = 643K$, and has a spontaneous polarization $P_s \approx 100\mu C/cm^2$ along the [111] axis.[93] The canting of the antiferromagnetic structure originates from the Dzyaloshinksii-Moriya interaction where interactions between neighbouring spins in the $(\bar{1}2\bar{1})$ plane lead to a helical spin wave, also known as a spin cycloid, with a period of 62 nm that propagates along the $[10\bar{1}]$ axis.[96,97] This spin cycloid takes the form of three electromagnon modes at 0.53, 0.555 and 0.72 THz that propagate along different crystallographic axes and can be tuned with the application of an external electric field.[98] Additionally, there is a known TO phonon mode that occurs at 2 THz.[99]

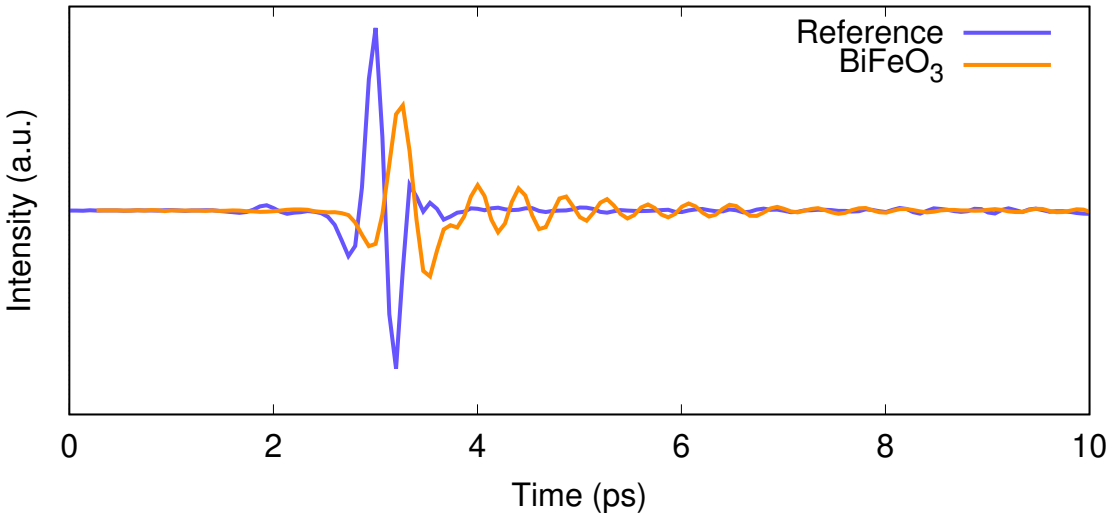

Figure 4.1: An example of the reference pulse compared to the same pulse having been transmitted through $BiFeO_3$, showing the reduction in magnitude accompanied by the resulting free induction decay (FID) of the pulse.

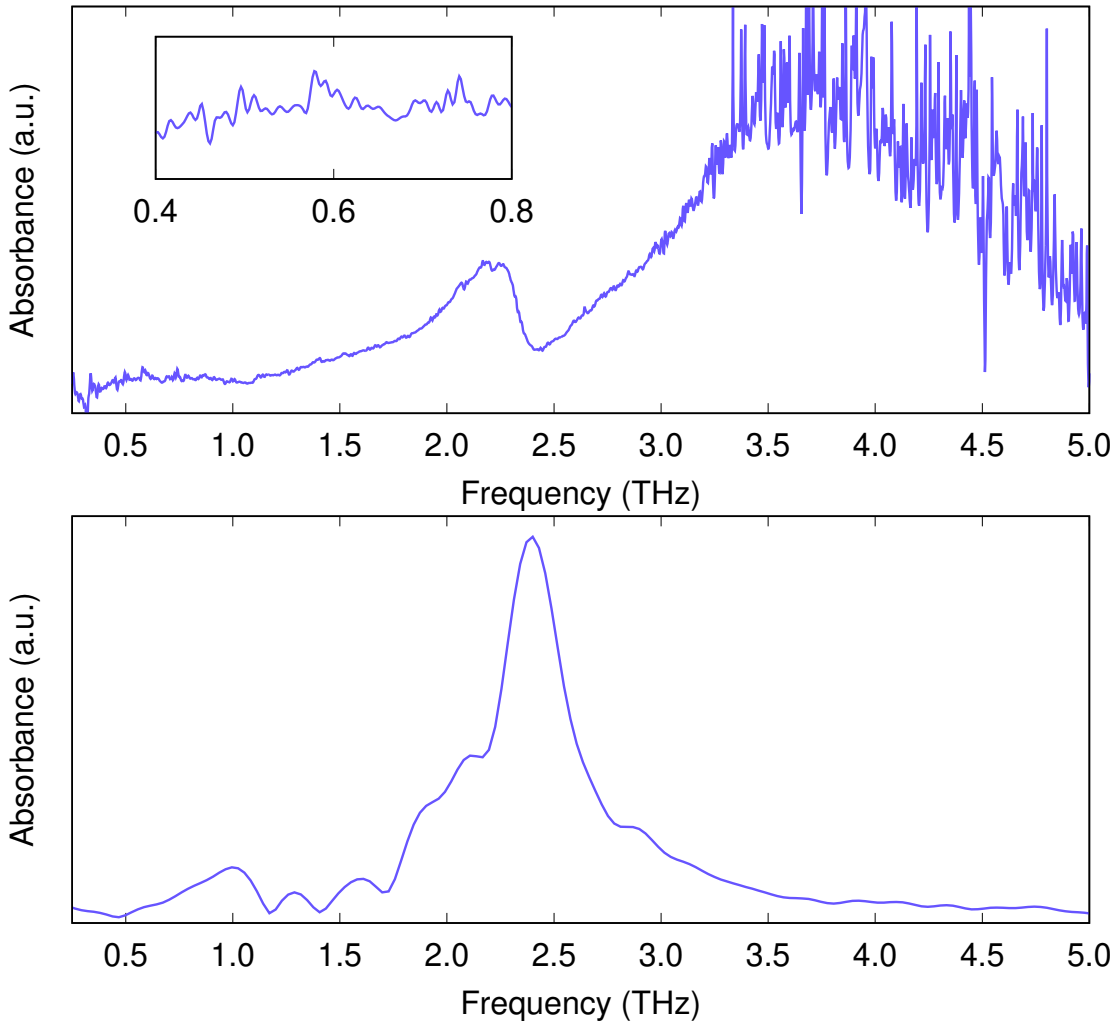

Figure 4.2: Top: the absorbance spectrum of the $BiFeO_3$ time trace, with a magnified inset between 0.4 - 0.8 THz. Bottom: the FT of the isolated FID.

Fig. 4.1 shows the transmission waveform in the time domain, clearly showing the FID immediately following the main THz pulse in the $BiFeO_3$ scan. This FID contains the information of processes that occur as a result of the excitation of the THz pulse. The resulting absorption spectrum can be seen in the top plot in Fig. 4.2, showing a variety of peaks between 0.5 - 2.5 THz. Here we expect to find the electromagnon modes between 0.5 - 0.75 THz (enhanced with inset) described in previous work,[37] however the DR in the low frequencies is to small to allow distinction of these peaks. In addition

to these excitations, there exists a TO phonon mode between 2 - 2.5 THz, as can be seen by the peak centered around 2.3 THz. The bottom plot shows the FT of the isolated FID response after the main pulse. Here it is possible to see the frequency components of the resulting processes excited by the THz pulse, in this case largely dominated by the phonon mode around 2.3 THz. The existence and tunability of the electromagnon modes have been previously discussed in research done in this lab, where the hybridization of THz light with a cavity magnon mode has been described.[37,101] However, these measurements have been restricted by the bandwidth of spectrometer used. The instrument described in this work allows for measurements roughly double the bandwidth, which can facilitate the study of TO phonons and other excitations unavailable with the previous instruments.

Chromium Oxide

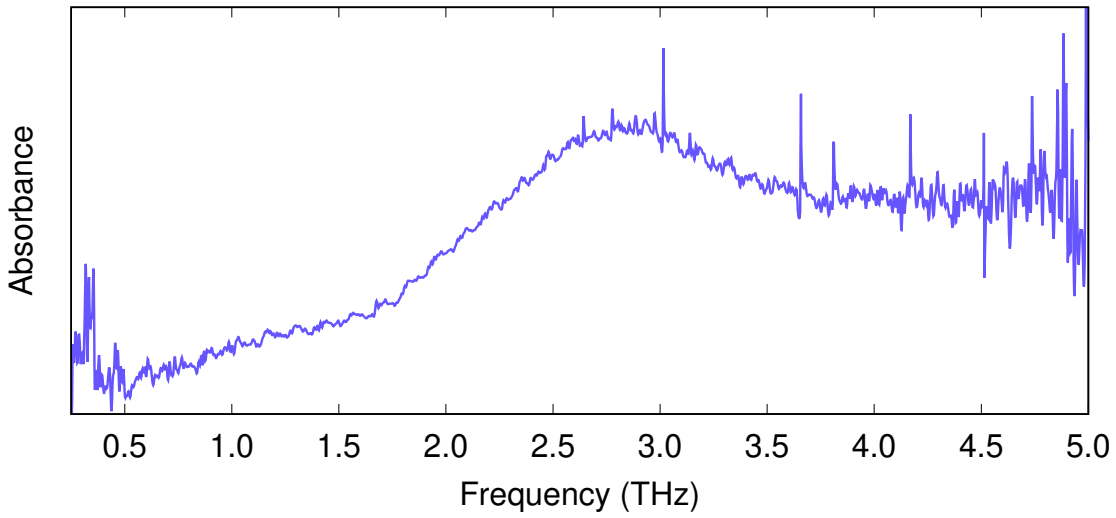

Figure 4.3: THz spectrum of multiferroic Cr_2O_3. While it is possible to resolve feature below 0.5 THz, numerical noise can easily dominate the low signal amplitude.

Since the preliminary data collected for BFO shows positive results, we now turn to the first material predicted to be multiferroic. Chromium oxide (Cr_2O_3) is the prototypical material predicted by Dzyaloshinskii[102] to have ferroelectric and ferromagnetic properties coexisting in the same phase. This phenomena was experimentally confirmed by Astrov soon after.[103] The structure of Cr_2O_3 is corundum with the $R\bar{3}c$ space group

and has antiferromagnetic ordering (T_N = 307.6 K).[104] Phonon modes have been predicted as low as 9 - 16 THz in Cr_2O_3 using density functional theory,[105] although a characterization of Cr_2O_3 in the THz region appears to be needed, therefore, it is a appropriate next candidate material.

Fig. 4.3 shows the absorption spectrum of Cr_2O_3 after removing the background spectrum. Here we hope to see absorption peaks due to phonon modes or the magnetoelectric effect based on the generation of a net dipole moment within 0.5 - 5 THz. There are notably sharp absorption peaks present between 3 - 4.25 THz, in addition to a large broad peak spanning roughly 2 - 3.75 THz, however these do not match phonon frequencies predicted.[106] It is possible that an increased lower end bandwidth suggests a difference with literature and suggests variability in powder size might be responsible for the change in this feature. The absence of definitive Gaussian or Lorentzian peaks that can be attributed to magnetic or ferroelectric modes yields no definitive results and calls for the need of other types of analysis.[37,101]

Copper Oxide

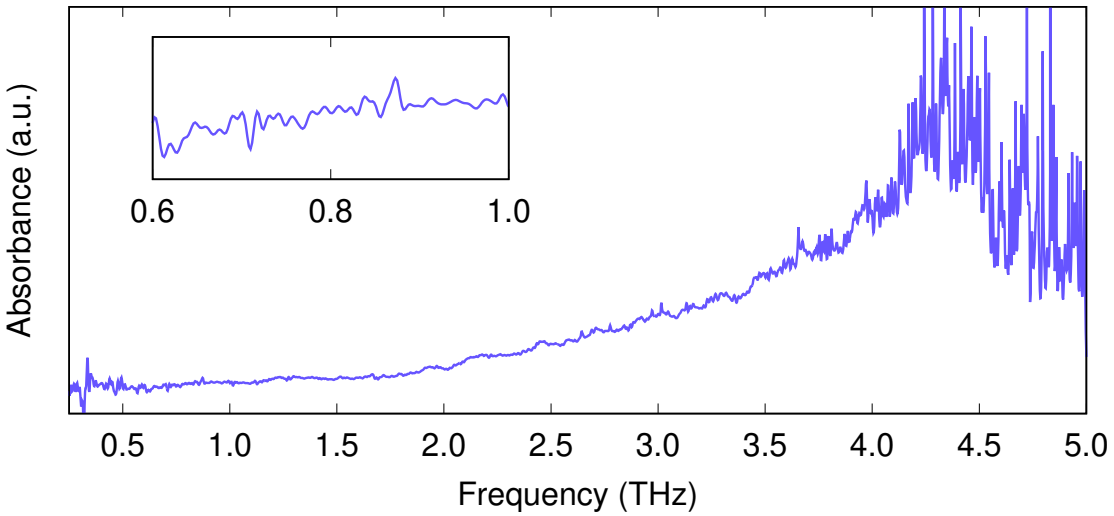

Figure 4.4: The absorbance spectrum showing the THz energy interactions in multiferroic CuO. Inset plot focuses on the known electromagnon mode in CuO.[110]

Copper (II) oxide (CuO) is also reported to be multiferroic and has phonon modes around 4.5 THz[106], and therefore, it is another prime candidate for use in testing the

instrument. CuO has a monoclinic structure with the $C2/c$ space group and takes on an antiferromagnetic order ($T_N \approx 210 - 230$ K)[107] along the $[10\bar{1}]$ axis and ferromagnetic order along the [101] with a spontaneous polarization of $P = 160$ μCm^2 along the b-axis.[108] It is a magnetically induced ferroelectric, and therefore a type II multiferroic, as well as a p-type semiconductor. The complex magnetic structure of CuO allows for the excitation of an electromagnon, which is a magnon that is excited by the electric field of incident EM radiation as opposed to the traditional magnon which is excited the magnetic field of the EM wave.[109] CuO is reported to have an electromagnon mode at 0.702 THz that can be tuned with the application of a static electric field.[110]

From the data collected, it is difficult to see electromagnon at 0.702 THz, however based on BFO data, picking out narrow absorbance peaks in this range on the GaP appears to be challenging in this region and are subsequently hard to detect. This is in part likely due to ambient conditions being higher than the Néel temperature of the antiferromagnetic order. There also exists a low power absorption peak around 0.86 THz, however this is difficult to differentiate from background noise. Another important point is that the instrument is not optimized for the range we expect to find the reported electromagnon mode and signal loss due to low SNR may require many scans to be collected to confirm the presence of electromagnon mode. Given that the electromagnon mode at 0.702 THz does not appear to be present, this warrants to use of other instruments to confirm these results.[37] Of note, however, are the small absorption peaks present 2.5 - 4 THz, above which the signal attenuates and the absorbance becomes saturated. Overall, the results obtained are inconclusive in terms of analyzing the electromagnon mode. This is an example of compound that would benefit from analysis in a DBR cavity with higher THz power in the region of interest[37,101]

ϵ-Iron Oxide Nanoparticles

Ferrite magnets have been known since the 7^{th} century BC and have since led the way in the development of magnetic devices.[111] As stated above, with the push to increase operating frequencies of communications and logic devices into the high GHz - low THz range, there is need for the development of magnetic devices that can couple to and operate at these frequencies. The next application of this instrument led to the characterization of ϵ-Fe_2O_3 nanoparticles (NPs) with the intention of quantifying their

ability to absorb THz light which could lead to their use in THz frequency antennas and sensors. The size and shape of these NPs are strongly dependent on the conditions used during their synthesis, and therefore, THz-TDS can also be used as a method to verify the geometry of the NPs based on spectral response.

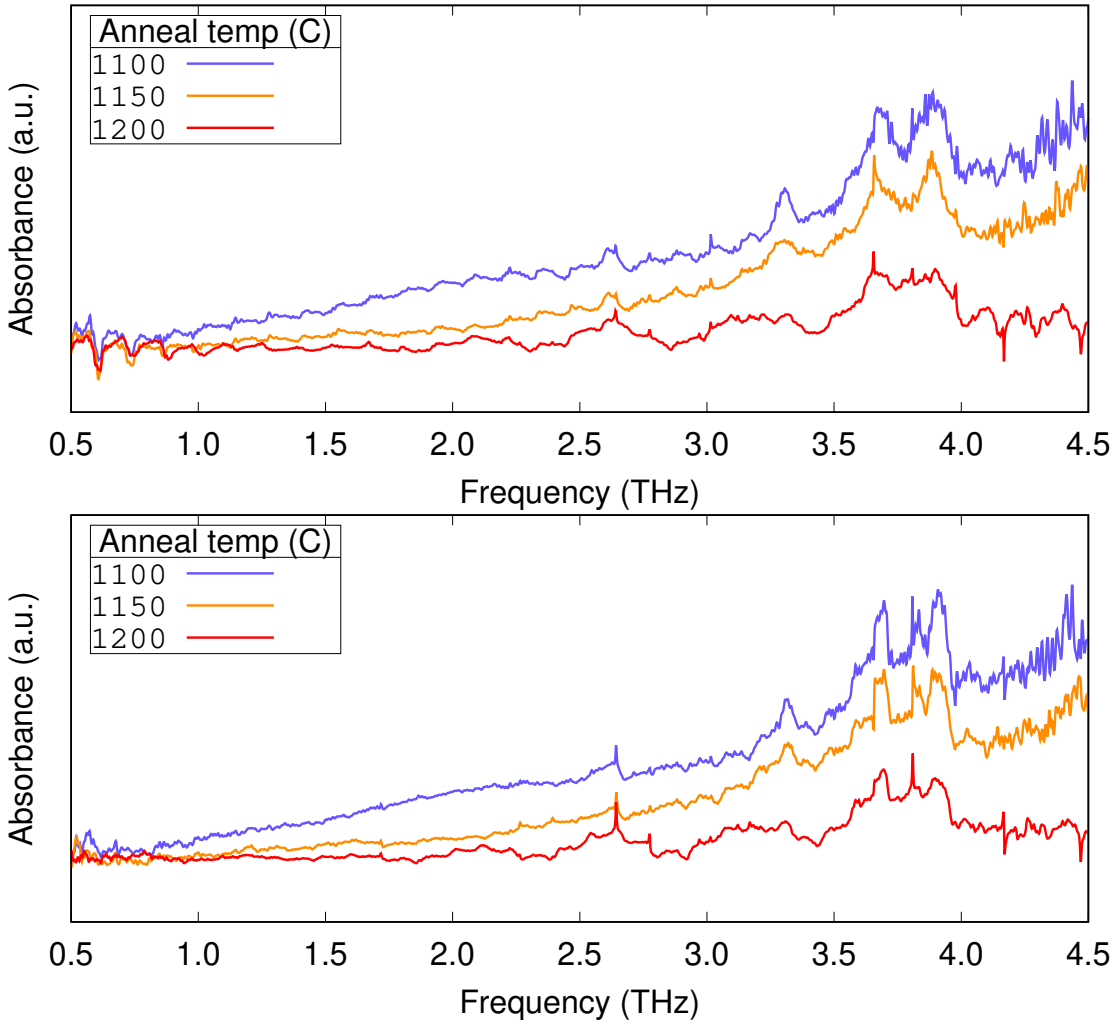

Figure 4.5: Top: The THz absorbance spectra of the ϵ-Fe_2O_3 NPs. Bottom: The same ϵ-Fe_2O_3 NPs absorbance spectra with the GaP etalon mode removed.

Four unique phases of Fe_2O_3 are known to exist. α-Fe_2O_3, also known as common rust, is weakly ferromagnetic, as is γ-Fe_2O_3. Both of these phases exist in nature, however, the other two phases, β-Fe_2O_3 and ϵ-Fe_2O_3, do not and must be artificially

synthesized. ϵ-Fe_2O_3 has been shown to have a significantly large magnetic coercivity[112] and can be made from γ-Fe_2O_3 when its particle size is reduced to 5 - 40 nm, otherwise it converts back to α-Fe_2O_3.[111] The space group of ϵ-Fe_2O_3 is $Pna2/1$, while the space group of α-Fe_2O_3 is $R3c$. Fig 4.5 shows the THz absorption spectrum of ϵ-Fe_2O_3 NPs that have been annealed at different temperatures, ranging from 1100 - 1200°C. The notable absorptions between 3 - 4 THz agree with phonon modes reported by Tokoro *et al.* which are attributed to the rod shaped structure. Here they report that the phonon mode at 2.51 THz is due to the vibration of the Fe atom along the a-axis.[111]

In the top plot of Fig 4.5 there appears slight oscillations in the spectra. These oscillations are due to the presence of FP etalons in the sample spectra. The bottom plot in Fig 4.5 shows the spectra of ϵ-Fe_2O_3 NPs after the removal of the spurious reflection via sigmoidal windowing. One caveat in the reflection removal process is that the removal of reflections can lead to the generation of artifacts in the spectra, which here take the form of the sharp peak at 2.64 and 3.81 THz. While data exists within region, as can be seen by the presence of peaks between the raw data and the data with the etalon removed, the extra sharp peaks are likely due to artifacts that arise from the reflection removal process. Additionally, since these spectra are calculated in absorbance (a.u.) rather than absorption coefficient (m^{-1}), the spectra do not take into account the amount of sample the beam has passed through, therefore the amplitude of absorption peaks may not be completely comparable. This being said, there does appear to be a trend in the different annealing temperatures.

The top plot in Fig 4.6 shows the spectra of a sample that had been synthesized almost 2 years prior to scanning. It can be seen here that exposure to ambient conditions for extended periods likely leads to the general degradation of NPs, as can be confirmed by the reduced intensity of the phonon modes around 3.5 - 4.0 THz. Furthermore, it has been reported that excessively high annealing temperatures lead to the conversion of ϵ-Fe_2O_3 to α-Fe_2O_3. This indicates that THz-TDS could be used as an *in situ* method for determining NP geometry, as well as a qualitative test for degradation of NPs. The absorbance spectra for α-Fe_2O_3 can be seen in the bottom plot in Fig. 4.6.

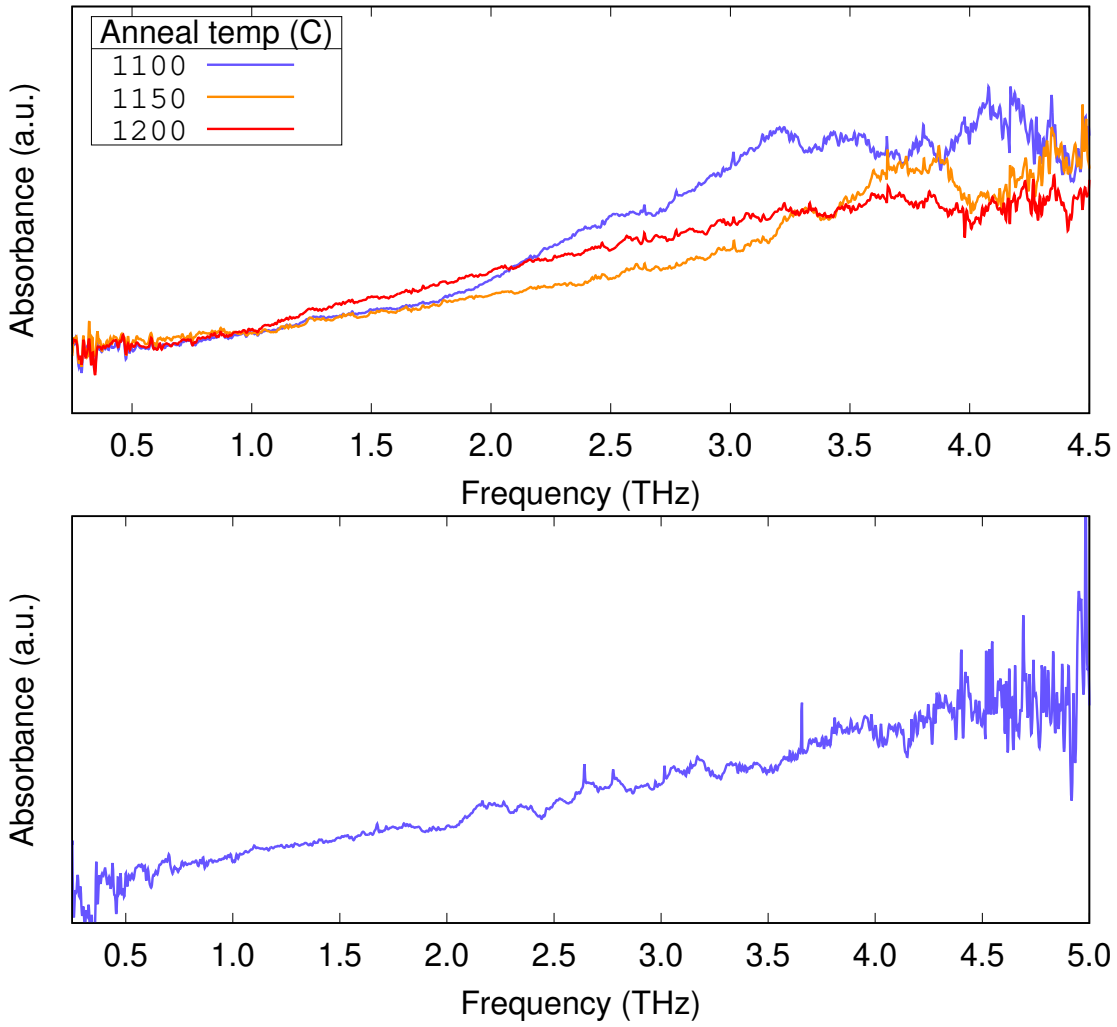

Figure 4.6: Top: The THz absorbance spectra of degraded ϵ-Fe_2O_3 NPs. Bottom: The THz absorbance spectra of bulk α-Fe_2O_3.

Scandium Vanadates

Further application of the spectrometer led to the characterization of novel scandium vanadate compounds being tested for their ability to facilitate ion conduction for a solid state fuel storage medium. Having a fluorite-like superlattice, these compound are interesting due to their ability to passively store fuels and oxidants.[113] Upon exposure to an oxidizing atmosphere, $ScVO_4$ can be converted to Sc_2VO_5, and in the process,

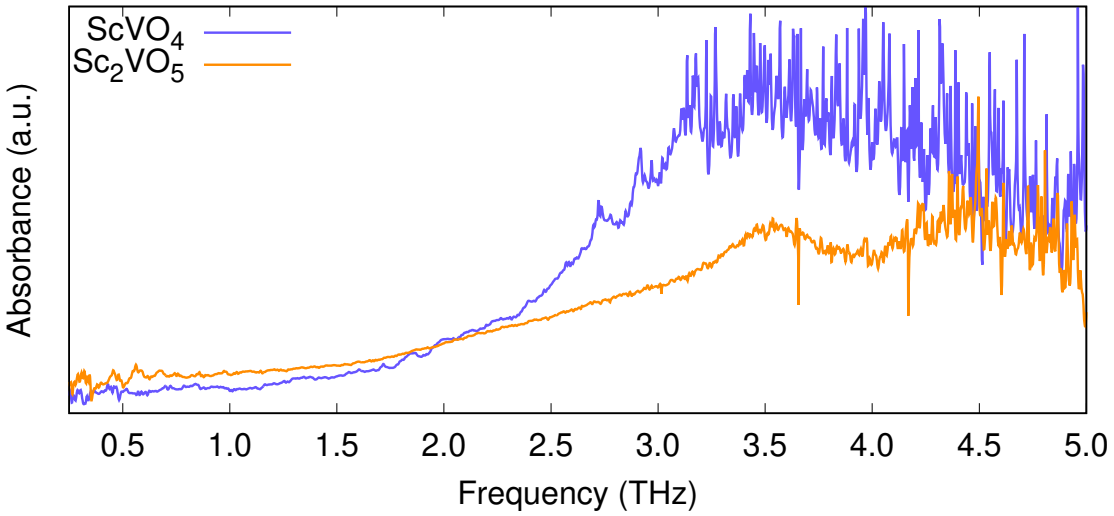

Figure 4.7: The THz-TDS spectra of $ScVO_4$ and Sc_2VO_5.

changes to its atomic ordering and space group. $ScVO_4$ is diamagnetic and of the $I4_1/amd$ space group, while Sc_2VO_5 takes on an antiferromagnetic order with the $I\bar{4}$ space group.

Since THz is sensitive to the change of mode in lattice vibrations, it is able to analyze changes in phonon modes to detect if structure is changing. When $ScVO_4$ absorbs oxygen and changes to the Sc_2VO_5 conformation, the subsequent change in lattice arrangements leads to a change in phonon modes that can exist, as can be seen in Fig. 4.7. Here it is possible to see the change in spectra after oxidation of $ScVO_4$ to Sc_2VO_5. The sharp peaks between 2.5 - 3.0 THz in $ScVO_4$ are likely due to TO phonons.[114]

Given the ability to distinguish between Sc_xVO_y compounds based on the presence of phonon modes, it could be possible to analyze oxidation progress *in situ* with a gas cell using THz spectroscopy. Furthermore, given that the signal between 3 - 4 THz is fully saturated in $ScVO_4$ as opposed to Sc_2VO_5, this could allow for the development of a phase-based optical switch.

4.1.2 Other interesting materials

While the first half of this chapter focused on materials that were scanned for outside collaborations in order to test the high-throughput capability, there were numerous compounds that were scanned that showed interesting features worth mentioning. Most

notably, Bi_2O_3, which, like other bismuth chalcogens and halides, has shown to offer a rich array of properties useful for THz frequency logical devices.[115,116,117] The absorbance spectra for Bi_2O_3 can be seen in the top plot of Fig. 4.8. Work done by Betsch *et al.* has shown that there is an acoustic phonon mode present at 108 cm^{-1} that roughly coincides with the large broad peak centered around 3.3 THz.[118]

Appendix C contains all of the metal oxide spectra that were collected in this work. These spectra were omitted from this chapter as not of all the spectral data could be fully interpreted, however, they were included as an appendix for the sake of completeness.

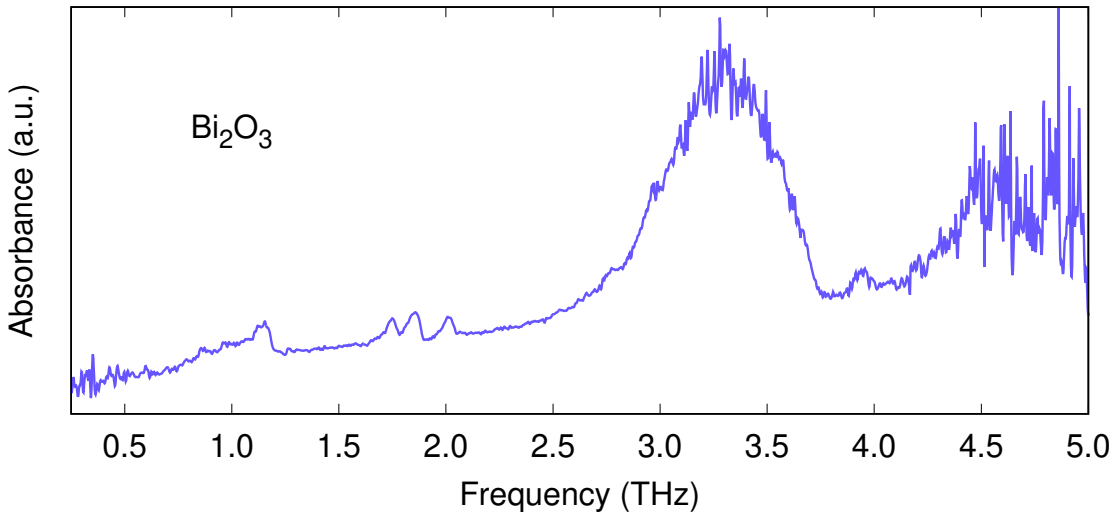

Figure 4.8: The THz absorbance spectra of Bi_2O_3.

4.2 Isomer Differentiation

In addition to characterizing solid state compounds, the ability to detect low energy molecular vibrations and rotations indicates that THz-TDS has potential for characterizing numerous interactions that arise in organic species. The following section addresses how THz-TDS can be used to identify different chiral species and differentiate heterogeneous mixtures of isomers.

4.2.1 Chirality

Chirality is a property of nature to have non-superimposable mirror images of the same object. This can manifest differently depending on the medium in which is being described. In terms of circularly polarized EM radiation or the generation of quasiparticles such as magnons, chirality takes form in the direction in which they rotate with respect to the direction of propagation. Chirality can also be attributed to the different conformations that certain molecules, which are called isomers, can take relative to each other. In molecular species that contain so-called chiral-centers, different conformations of the same molecule can exist depending on how the different moieties protrude from the chiral center. There are numerous types of isomers, some as simple as sharing the same molecular formula like in constitutional and conformational isomers, while others contain much more subtle differences, like in that of enantiomers and diastereomers (arrangement of atoms around chiral center) or tautomers (arrangement of one or more bonds around chiral center). Molecular chirality is an crucial concept in many areas, ranging from drug design to polymer manufacturing. This is exemplified in Fig. 4.9 where this figure shows how two different enantiomers can have significantly different effects on the symptoms they are able to treat. However, due to similarities between the isomeric species, they are often very challenging to separate and measure in relative ratios.

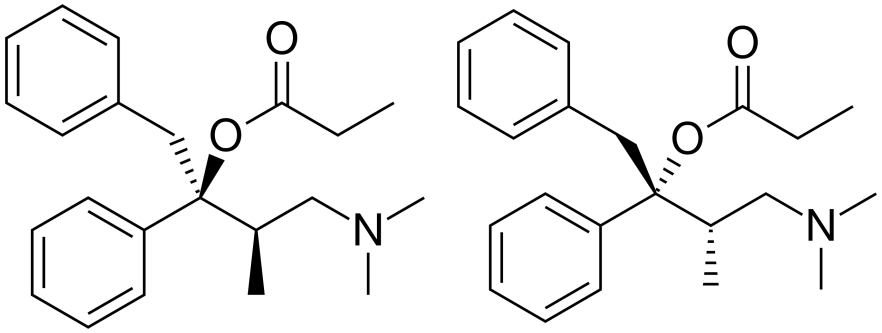

Figure 4.9: Two enantiomers of propoxyphene. The molecule on the left is dextropropoxyphene, a painkiller, and on the right is levopropoxyphene, a cough suppressant

Current schemes for identifying chiral species present in a sample originate from early attempts to separate and identify different enantiomers through their ability to rotate

the polarization of transmitted light.* This type of analysis is still widely used today as the *de facto* method for analysis in determining isomer purity, however there is no direct way to to relate the rotation of polarized light to a given isomer or the ratio of concentrations in heterogeneous mixtures. While this method is outdated and rife with issues, it remains the main method of identification as enantiomers generally have similar enough physical properties to prohibit separation through conventional chemical separation techniques. Though there are high performance liquid chromatography instruments capable of isolating different enantiomers based on certain chemical affinities, these instrument are usually costly and can require long elution times. Given THz-TDS can detect changes in vibrational and rotational modes on the whole molecule scale, it offers a quick and reliable method for the distinction of isomeric species.

Since vibrational modes in the THz region are largely comprised of complex, full molecule flexing and molecular rotations, THz-TDS can be a useful technique in analyzing mixtures of isomers and could find use in applications like quality control in pharmaceutical manufacturing.[119] Given that any minor structural change can lead to wholly different vibrational modes between isomers and inter-/intramolecular noncovalent interactions like hydrogen bonding that can be formed in different tautomers, analysis done with THz-TDS can non-destructively examine these type of low energy interactions. This indicates that THz spectroscopy can offer a rapid alternative to analyze isomers and mixtures of isomers in order to identify which conformations are present and in what ratio.

4.2.2 Amino Acids

When evaluating a new form of analysis it is prudent to start with relatively simple analytes. Amino acids are small molecules that exhibit chirality and are widely available as the precursors to numerous different species including pharmaceuticals and catalysts. While the use of THz-TDS in isomer analysis has been shown to distinguish simple amino acids, it has still been largely unexplored and could stand to benefit from a rigorous evaluation of how materials respond to THz light. Most current work in this area often only analyzes amino acids that are in the solid state. While this is a valid proof of

*In IUPAC naming conventions, each chiral center in a given species is assigned an R or S in order to delineate the orientation of its conformation. For the sake of brevity, this work will resort to using the older D/L notation derived from optical, or Faraday, rotation.

concept, crystal structures of isomers commonly have completely different space groups and lattice ordering which means that they would have different vibrational/phonon modes, and therefore is not a suitable proof of isomer differentiation, merely that of crystal structure detection.

As King *et al.* point out, many changes in vibrational modes due to changes on molecular orientation can lead to subtle shifts in peaks position, therefore it is relevant to supplement empirical data with computational simulations.[122] Multiple studies have been conducted using both THz analysis and density functional theory (industrial isomer determination of D/L-glutamic acid + DFT,[121] serine THz + DFT,[122] Leucine and methionone THz + DFT,[123] and hydroxyglutarate acid disodium salt + DFT.[124]) Other amino acid studies: tyrosine,[125] histidine THz,[126] alanine THz,[127,128] serine and cysteine,[129] tryptophan,[130] valine and norvaline.[131,132] As well as other simple chiral molecules, such as tartaric acid THz + DFT.[133]

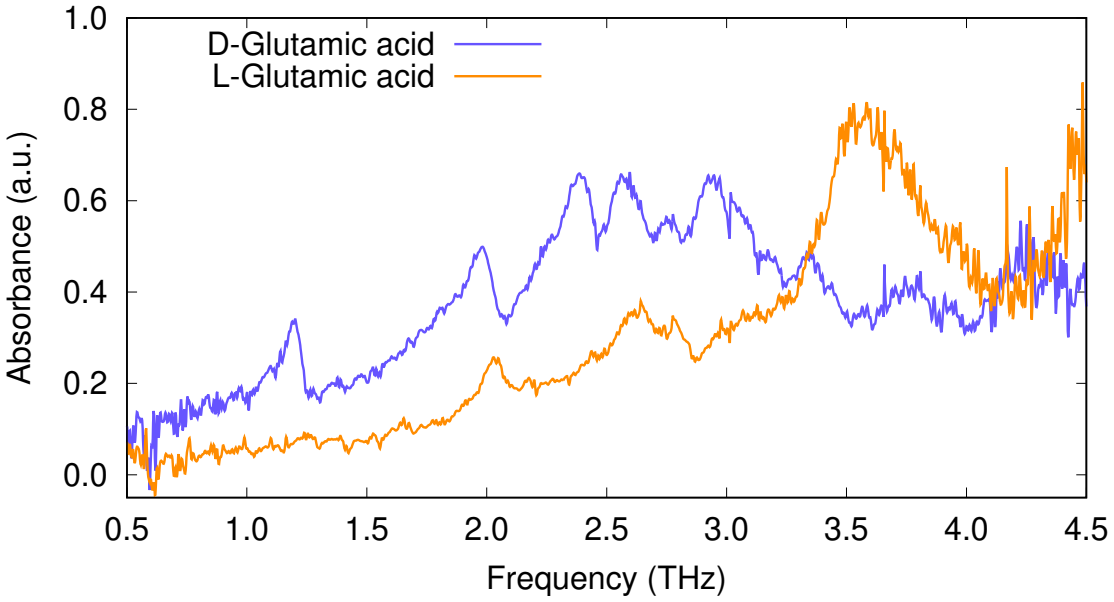

Figure 4.10: THz spectra of both the D and L enantiomers of glutamic acid

In order to show that the spectrometer introduced in this work is capable of scanning and differentiating unique isomers, different isomers of glutamic acid were scanned to evaluate the ability of THz-TDS to detect the subtle changes in vibrational modes. The absorbance spectra for the D and L enantiomers of glutamic acid can be seen in

Fig. 4.10. Here it is seen that the different configurations lead to significantly different THz spectra, allowing for identification by spectra alone.

THz spectroscopy has also been expanded beyond the analysis of simple amino acids to include more complex molecules. THz-TDS has been shown to be useful in determining concentrations of sugars,[134] including natural[135] and artificial.[136] It has also found use in measuring the presence of pesticides in organic samples.[137] Furthermore, studies which utilize ATR experiment shave shown the detection of single base mutation in DNA oligonucleotides,[138] however, not using ATR geometry optimized for THz light.

As previously discussed, often times it is necessary to analyze organic compounds that are dissolved in solvents which can lead to issues involving erroneous THz absorptions due to polar or protic interactions. Instances such as these are what lead to the development of the ATR prism. Initial measurements with the prototype prism indicated potential for the technology to work, however, application of small amounts of water as a test sample fully quenched the signal. The fabrication of a larger ATR prism was completed in order to properly collect all incident light. Unfortunately, issues with alignment prevented the full incorporation of the new ATR prism into the spectrometer. This is due to the fact that the ATR prism was mounted in 3 axis stage which is not appropriate for the alignment of such a sensitive optic, as described by Soltani *et al.*.[79] Here they discuss how errors in alignment in the pitch and yaw of an ATR prism can lead to the propagation errors getting exponentially worse with minor deviations of the alignment of the prism. Therefore, a 6 axis stage that includes yaw, pitch, and roll is needed to properly address misalignment issues.

The beauty of a living thing is not the atoms that go into it, but the way those atoms are put together.

Carl Sagan

5 Summary and Outlook

Spectroscopy is the study of how energy and waves interact with materials of interest. In practice, it is accomplished by applying EM radiation to samples through transmission, reflection, or by an evanescent wave that is formed during internal reflection. Using a single-cycle pulse of THz light, THz-TDS allows one study temporal effects on the order of picosecond to nanoseconds. The THz region of the EM spectrum spans from 0.1 - 10 THz and is comprised of energies on the order of 0.4 - 40 meV, therefore THz-TDS is able to probe slow, complex molecular vibrations/rotations, coherent waves of collective excitations (*e.g.*, magnons, phonons, *etc.*), and hydrogen bonds, among other low energy dipole moments. THz-TDS is still a relatively new technology that many different research areas could stand to benefit from. Unfortunately, due to complications in generation and detection schemes, as well as excitations caused by atmospheric humidity, THz-TDS is faced with numerous difficulties in the identification and analysis of materials.

The aim of this work has been to design a broadband THz-TD spectrometer for high-throughput measurements and to optimize ATR for THz light to allow this technology to find use in rapid characterization of low energy phenomena. This document has shown not only the theory behind THz generation and detection schemes using nonlinear optics,

but also the determination of ideal generation and detection material for use with a 1040 nm NIR laser, namely (110) cut gallium phosphide (GaP). This thesis also describes how data is collected and processed in THz-TDS experiments, in addition to the handling of spurious reflections through customizable window functions. The ATR prism geometry and choice of material were determined in order to optimize its functionality when used with THz light. Using HRFZ Si as the prism material ensures a high enough index of refraction that allows for various samples to satisfy total internal reflection. Furthermore, when using an ATR prism cut to Brewster's angle, significant reflective losses are avoided. The prism also then acts as a Brewster polarizer which allows for the choice of electric or magnetic coupling in experiments by simply rotating the prism in the beam. For materials with higher indices of refraction, such as HRFZ Si, the smaller prism angle also leads to an increase in penetration depth.

The practical construction of a THz-TD spectrometer is outlined, which includes all of the optical components as well as a custom aluminum purgebox. The THz power generated by this spectrometer was measured and calibrated against a commercial power meter, as well as the analysis of its performance through common metrics. Finally, having shown that the instrument is capable of collecting the absorbance spectra of materials of interest, samples from various classes of materials were analyzed with the instrument as a proof of concept to confirm its functionality and evaluate how THz-TDS can be used to further develop our understanding of how materials behave in response to THz EM radiation.

The instrument built in this work utilizes THz EM radiation generated by optical rectification of 1040±20 nm NIR light in 0.3 mm (110) GaP, and the subsequent detection of THz light through the Pockels effect in an additional 0.3 mm (110) GaP. The modulation of polarization due to the Pockels effect is then measured by balanced photodetection and the spectral content is extracted using the Fourier transform. The instrument was built in a way to allow for experiments to be run with either collimated or focused light and therefore has space to allow for the installation of extra optics including the prototype ATR prism constructed in this work. In addition, the purgebox was fitted with a humidity sensor connected to solenoid valve that controls the flow of dry N_2 gas to ensure consistent humidity levels during scans.

The instrument was used in the characterization of multiple classes of materials where it was shown that the apparatus can be used to study numerous low energy phenomena,

such as magnetic excitations and vibrational modes of material. It was shown that this apparatus can be used to allow researchers to probe systems intended for telecommunications and computing devices, as well as pharmaceuticals and organic catalysts. Given that THz frequencies are able to excite lattice dynamics and complex molecular motion, this technology also lends itself to the rapid identification of different isomeric species. With the ability to investigate many different types of material in multiple different phases, THz-TDS has been shown that it is a incredibly useful technique comparable to IR spectroscopy. This indicates that this technology will help pave the way for many low power alternatives to current technologies.

Immediate next steps with this instrument are to overcome the alignment issues faced with the ATR prism as these deviations in alignment can lead to errors that propagate throughout the apparatus.[79] Once that is complete, a motorized stage can be utilized to allow for the automatic insertion/removal of the prism from the beam. This allows for the reference and sample spectra to be completed in the same purge, further expediting the collection process. One additional interesting feature that arises with the inclusion of a motorized stage is that it allows for the deliberate translations of the prism in the beam and can be used to create a raster image of spectral data, also known as a hyperspectral image. Hyperspectral imaging is a technique in which an image is produced by collecting spectral data at every pixel and can be done with an ATR setup. The sample is first mounted on the ATR prism and the prism is then mechanically translated through the beam thereby generating a multidimensional image with pixel resolution defined by the diffraction limit and the Goos-Hänchen shift.

Looking forward, the author believes this technology has potential to offer unique insight into low energy interactions in many different areas, including the manufacturing of medicinal compounds and solid state device development. With the incorporation of ATR, THz-TDS can be used for built-in quality control for inline manufacturing. This would allow for pseudo real-time analysis of certain analytes of interest, such as isomers present in pharmaceutical manufacturing. Furthermore, with a carefully tuned air gap, the Kretschmann configuration for ATR allows for non-contact analysis which has already been empirically shown to work.[6,140]

A

IR Effects on THz Generation

While optical rectification (OR) is analogous to difference frequency generation (DFG), it is its own unique phenomena in which two photons of monochromatic light are simultaneously absorbed. The energy of both photons sum together to excite an electron occupying a σ bond in a nonlinear media to accelerate it along its bond. The resulting acceleration of charge leads to the generation of THz photons as the electron subsequently decelerates and releases energy. This displacement causes a local distortion of charge, and therefore, electric polarization within the material.

Optical rectification is a second order polarization effect, and as such is proportional to E^2. Since 1040 nm light has a frequency of 288 THz, oscillations of the IR pulse

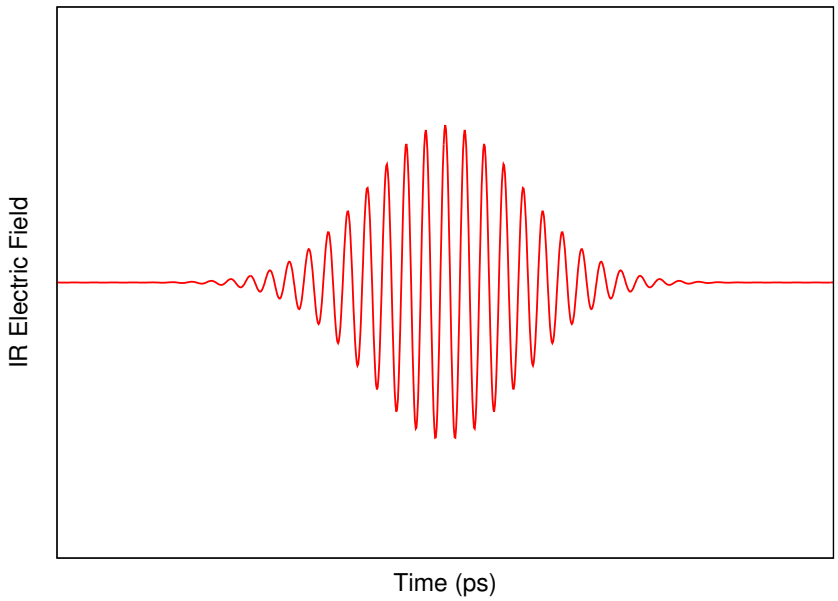

Figure A.1: Example IR pulse as generated by the laser

are hundreds of times faster than that of THz light. The radiated amplitude of THz light is proportional to polarization, and therefore, it is often beneficial to refer to the pulse envelope traced out by the pulse rather than the pulse itself.[141] An example of the NIR pulse from the laser can be seen in Fig. A.1. When the pulse is squared it becomes positive, as can be seen in Fig. A.2, where the bottom plot shows E^2 and the top plot depicts the resulting pulse envelope. Using the far field limit of the dipole approximation can allow for E_{THz} to be approximated as $\partial^2 P/\partial t^2$,[33] where the shape of the THz pulse is simulated by taking the second time derivative of the pulse envelope. Fig. A.3 shows how taking the 2^{nd} derivative of the pulse creates the same form as the THz pulse.

Unfortunately, this is not the same shape we see when taking scans of the real pulse collected with the instrument. The nonsymmetric pulse collected by the apparatus is a result of the skewing of the IR pulse that can be attributed to the non-uniform distribution of wavelengths within the chirped pulse, as well as temporal broadening of the pulse associated with dispersion through nonlinear materials. In reality, the generation of THz light is not easily attributed to a single process and is likely generated by multiple different nonlinear interactions, including both OR and DFG.[142] This leads

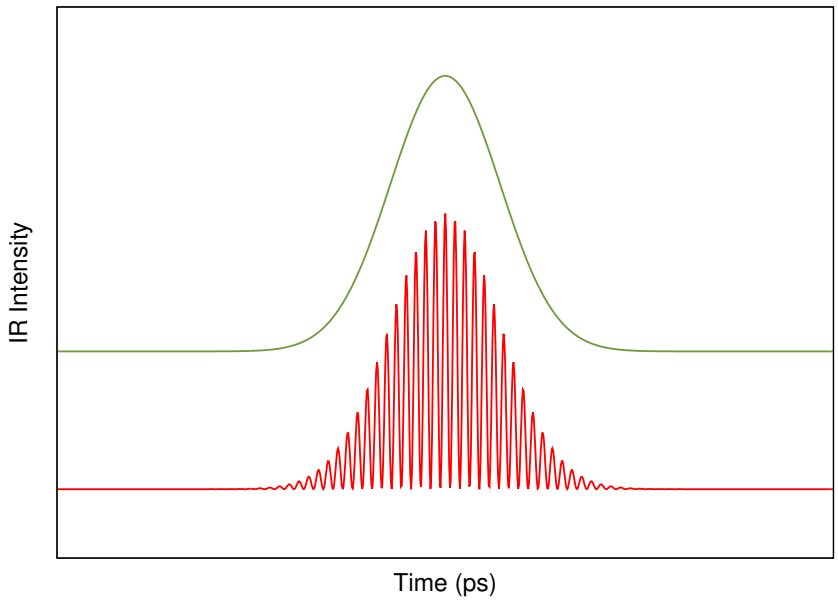

Figure A.2: Intensity of the IR (bottom) and its pulse envelope (top)

to a variety of different pulses that overlap leading to a skewed pulse. The plot on the left of Fig. A.4 shows a simulated skewed Gaussian pulse while the plot on the right shows the 2^{nd} derivative of the skewed pulse, showing a THz pulse that more closely matches that of what is collected by the instrument. Lee talks about pulse shape and the resulting spectral bandwidth and relates how as the pulse becomes increasingly non-uniform the spectral content of the diminishes.[35]

When trying to maximize THz generation it is important to consider the wavelength of IR that leads to phase matching within the material. For GaP phase matching occurs at 1060 nm light, so as more 1060 nm spectral content is generated by the laser, the power of THz light is maximized. The plot on the left in Fig. A.5 shows the IR spectrum produced by the laser. THz generation is maximized when the 1060 nm spectral content is maximized due to group and velocity phase matching in GaP. This effect can be seen in the right plot of Fig. A.5, where the laser spectrum with more 1060 nm light leads to a larger amplitude of THz generation. Altering the spectral content of the laser spectrum is possible by altering the settings of the laser in the software that control it.

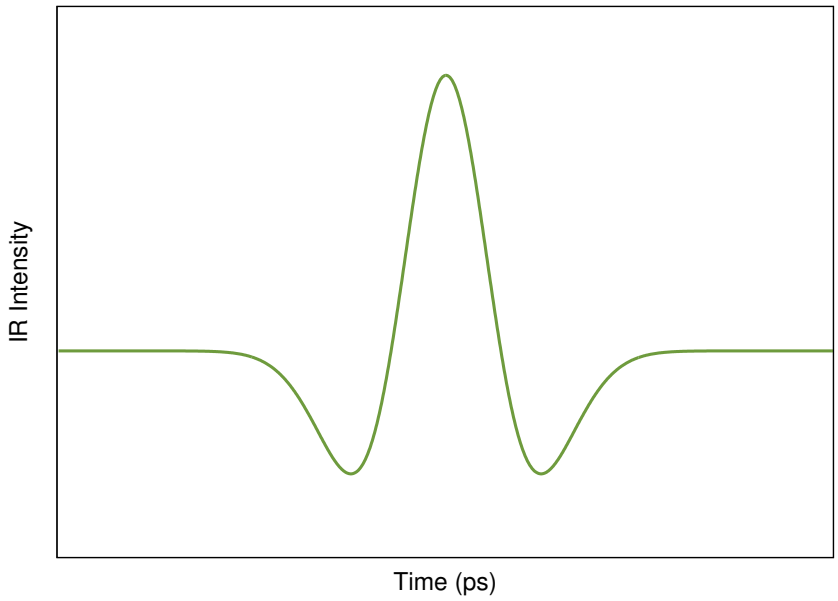

Figure A.3: 2^{nd} derivative of the IR pulse envelope, showing the rough outline of the THz pulse ($E_{THz} \sim \frac{\partial^2 P}{\partial t^2}$)

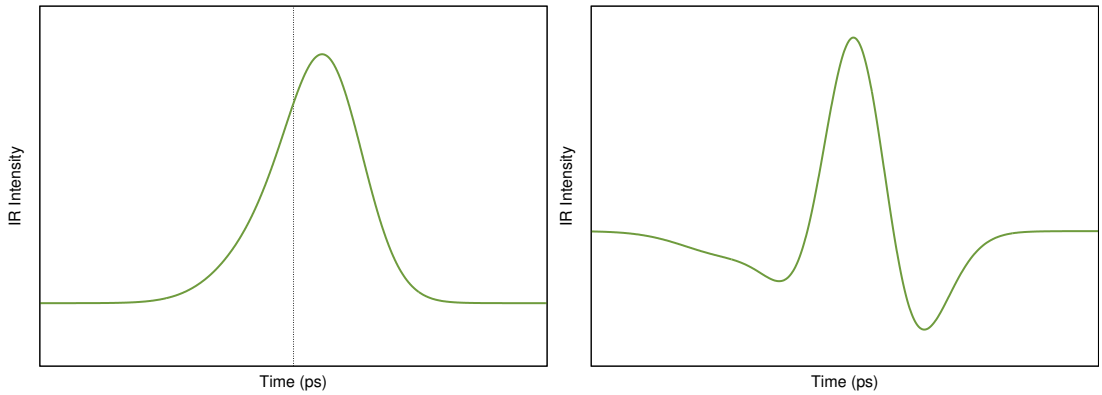

Figure A.4: A skewed IR pulse envelope (left) and the resulting 2^{nd} derivative THz pulse shape. This pulse shape is closer to what is actually measured and can be attributed to dispersion in the generation/detection crystals.

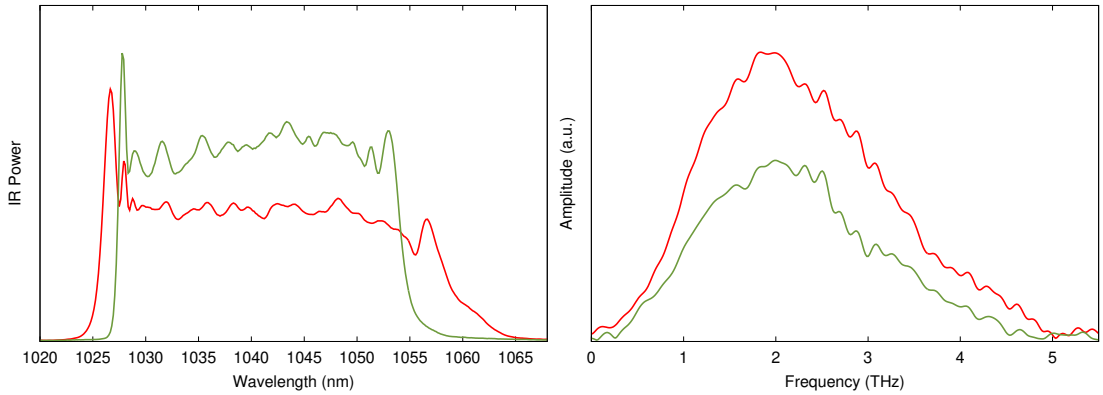

Figure A.5: The plot on the left shows two different IR spectra for the laser used in THz generation. On the right is the resulting THz spectra, colour matched to the corresponding IR spectra.

B

Data Analysis

In spectroscopy, an absorption peak results from the absorption of energy by a system undergoing some type of transition. Absorption peaks are not infinitesimally sharp however, and energy of the transition dictates the size and shape of the peak. In ideal conditions, these take the shape of Gaussian, Lorentzian, or Voigt functions, although they usually take on more complex configurations. Furthermore, peaks can undergo broadening related to energy changes in the system present while collecting data, *eg* thermal (Doppler), pressure or collision, and proximity broadening. Often times when collecting the spectroscopic response of a given material, the spectrum contains many peaks that are convolved together, and therefore, it is necessary to employ special methods in order to recover all possible information from the system.

B.1 First and Second Derivatives

Sometimes peaks are located too close together to fully resolve even when collecting long scans. In order to distinguish spectral features, one can take the derivative of the spectrum to deconvolve overlapping peaks. Taking the first derivative helps to separate the peaks, and further taking the second derivative displays the constituent peaks as negative peaks. One must be careful in this approach however, as peak widths and

intensities are changed in the process.

Fig B.1 shows two Gaussian peaks (dashed lines) convolved together (solid red line). Below are the first and second derivatives of the combined peaks, showing how this method can aid in differentiating peaks to close to resolve.

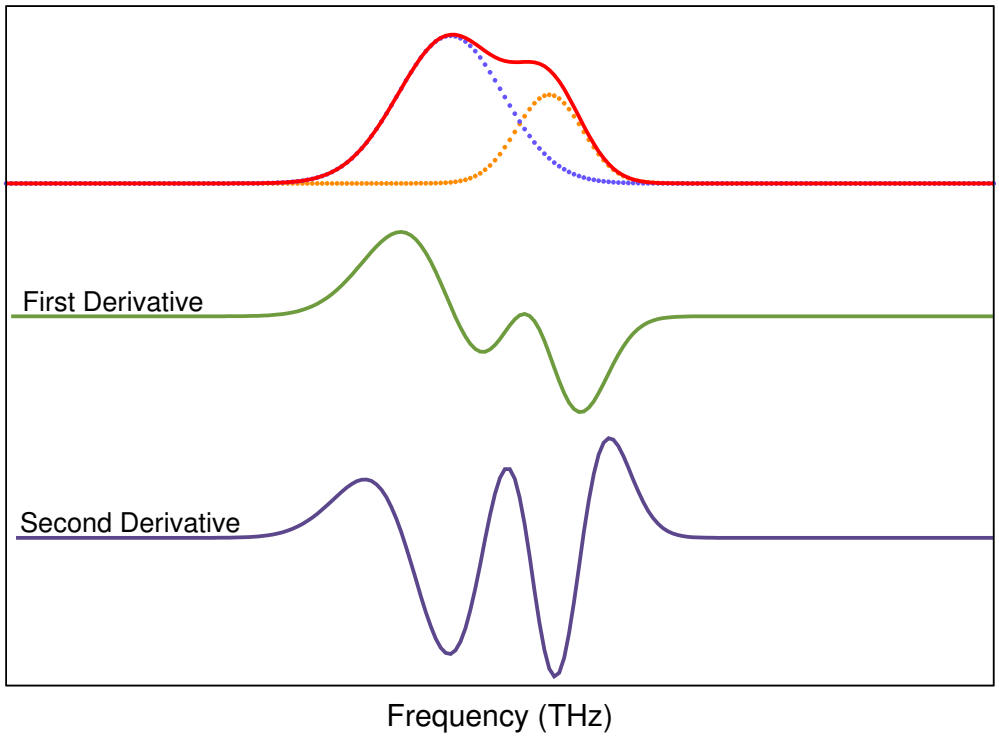

Figure B.1: Top plot is an example peak that is a convolution of two Gaussian peaks. Middle plot is the first derivative, showing the separation of the peaks much more clearly. Bottom plot show the second derivative, allowing individual peaks to be seen as negative peaks.

C

Transition Metal Oxide Spectra

This appendix contains all of the transition metal oxides (TMOs) that were scanned during the work done for this thesis. Not all of the spectra were able to be fully interpreted, however, these results were added for the sake of completeness. At the time of publication there are very few databases of THz spectra that are publicly available, and of those, many are quite sparse (and done with literally anything found around the office, looking at you NIST). There are currently many databases for XRD, UV-Vis, FTIR, and NMR spectra for thousands of different compounds in order to help expedite the research process. As this work was publicly funded, the author believes this data should therefore be made publicly available.

need for reference database in potential materials - to see if there are features present in precusors that wouldn't be attirbuted to materials of interest

Table C.1 contains all of the TMOs along with the oxidation state of the metal ions, their magnetic ordering, and the space group of the phase that was scanned. The following list categorizes the TMOs based on common structures and provides more information on their electronic environment.

Rutiles: ($P42/mnm$), octahedral environment

- TiO_2 (4+, d0)

- CrO_2 (4+, d2)
- SnO_2 (4+, p0)

Corundums: ($R\bar{3}c$), octahedral environment

- V_2O_3 (3+, d2)
- Cr_2O_3 (3+, d3)
- Al_2O_3 (3+, p0)

Spinels: ($Fd\bar{3}m$), octahedral and tetrahedral environments

- Co_3O_4 (2+/d7 oct, 3+/d6 tetr)
- Fe_3O_4 (2+/d6 and 3+/d5 in oct, 3+/d5 in tetr)

Bixbyites: ($Ia\bar{3}$), two octahedral environments

- In_2O_3 (3+, p0)
- Mn_2O_3 (3+, d4)
- Y_2O_3 (3+, d0)
- Pr_4O_{11} (3+, f)
- Sc_2O_3 (3+, d0)

Table C.1: A list of all d-orbital containing species which had the THz spectrum collected.

Material	Oxidation state(s)	Magnetic Ordering	Space Group
Sc_2O_3	3+	diamagnetic	$Ia\bar{3}$
V_2O_3	3+	antiferromagnetic	$R\bar{3}c$
VO_2	4+	ferromagnetic	$P2_1/c$
V_2O_5	5+	—	$Pmmn$
Cr_2O_3	3+	antiferromagnetic	$R\bar{3}c$
CrO_2	4+	ferromagnetic	$P4_2/mnm$
MnO	2+	antiferromagnetic	$Fm\bar{3}m$
Mn_3O_4	2+,3+	ferrimagnetic	$I4_1/amd$
Mn_2O_3	3+	ferrimagnetic	$Ia\bar{3}$
MnO_2	4+	—	$P4_2/mnm$
Fe_2O_3	3+	antiferromagnetic	$R3c$
Co_3O_4	2+,3+	antiferromagnetic	$Fd\bar{3}m$
CoO	2+	antiferromagnetic	$Fm\bar{3}m$
NiO	2+	antiferromagnetic	—
Cu_2O	1+	—	$Pn\bar{3}m$
CuO	2+	antiferromagnetic	$C2/c$
Y_2O_3	3+	diamagnetic	$Ia\bar{3}$
MoO_3	2+	—	$Pnma$
Sb_2O_3	3+	—	$P2_1/c$
BaO	2+	—	$Fm\bar{3}m$
Bi_2O_3	3+	—	$P2_1/c$
$BiFeO_3$		antiferromagnetic	$R3c$
$ScVO_4$		diamagnetic	$I4_1/amd$
Sc_2VO_5		antiferromagnetic	$I\bar{4}$

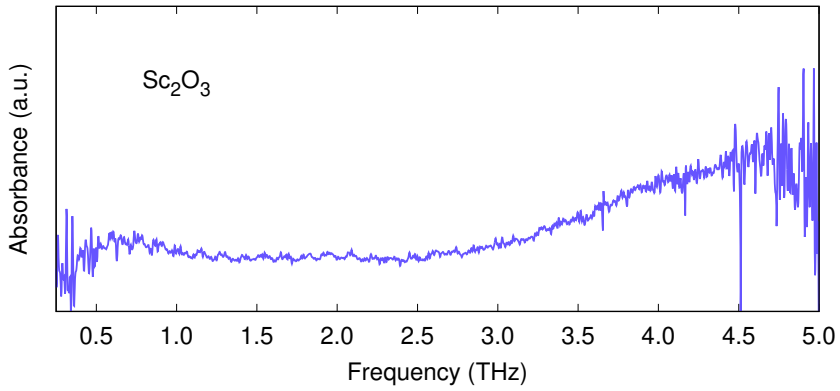
Sc2O3
Absorbance (a.u.)
0.5
1.0
1.5
2.0
2.5
3.0
3.5
4.0
4.5
5.0
Frequency (THz)

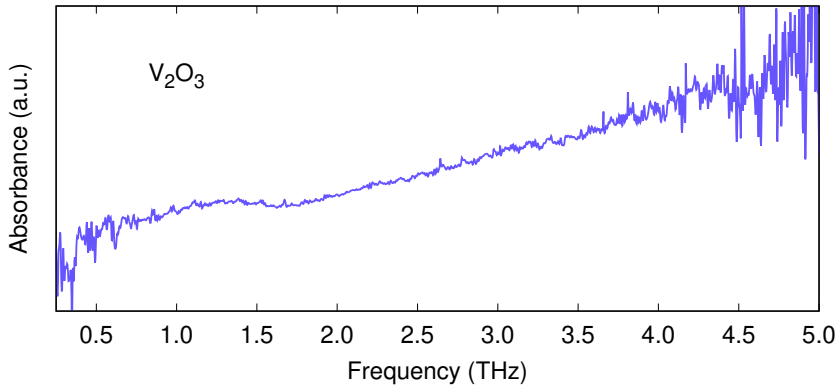
V2O3
Absorbance (a.u.)
0.5
1.0
1.5
2.0
2.5
3.0
3.5
4.0
4.5
5.0
Frequency (THz)

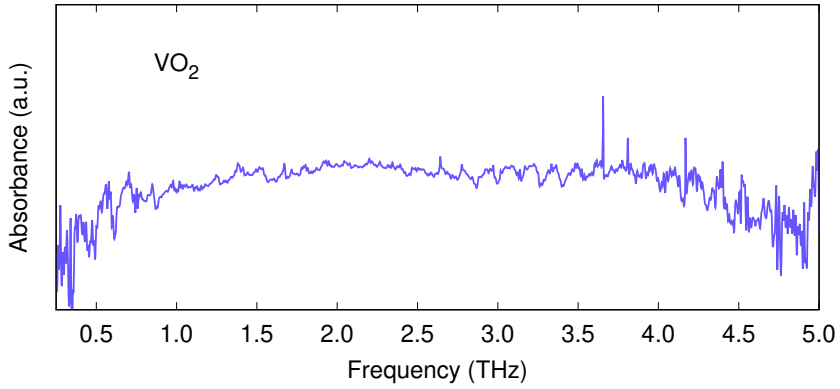
VO2
Absorbance (a.u.)
0.5
1.0
1.5
2.0
2.5
3.0
3.5
4.0
4.5
5.0
Frequency (THz)

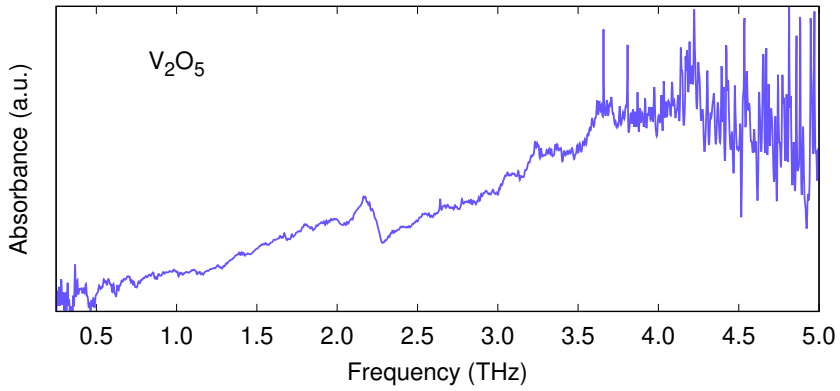
V_2O_5
Absorbance (a.u.)
0.5
1.0
1.5
2.0
2.5
3.0
3.5
4.0
4.5
5.0
Frequency (THz)

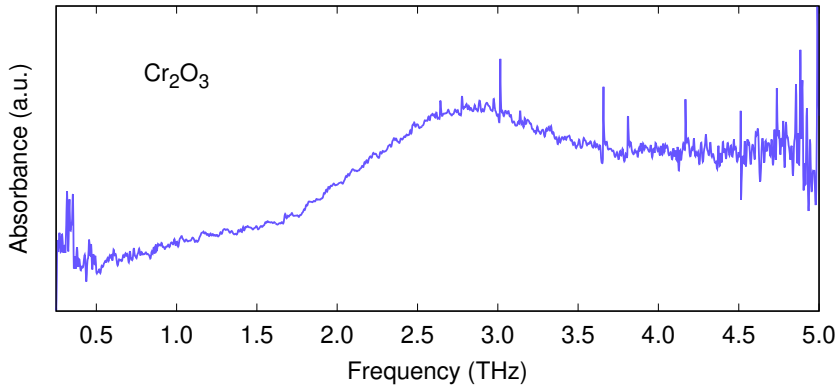
Cr_2O_3
Absorbance (a.u.)
0.5
1.0
1.5
2.0
2.5
3.0
3.5
4.0
4.5
5.0
Frequency (THz)

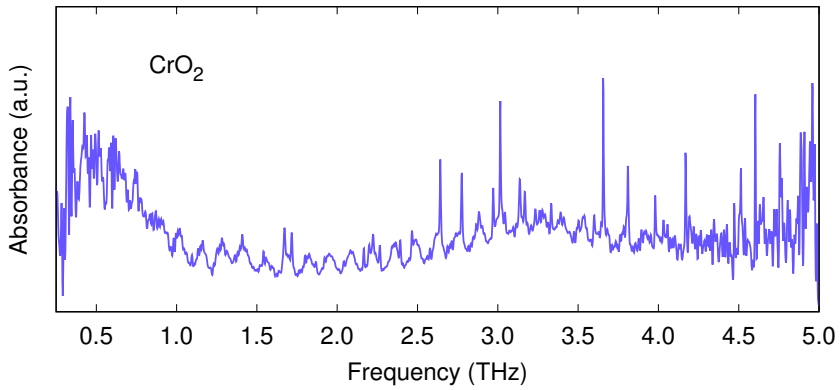
CrO_2
Absorbance (a.u.)
0.5
1.0
1.5
2.0
2.5
3.0
3.5
4.0
4.5
5.0
Frequency (THz)

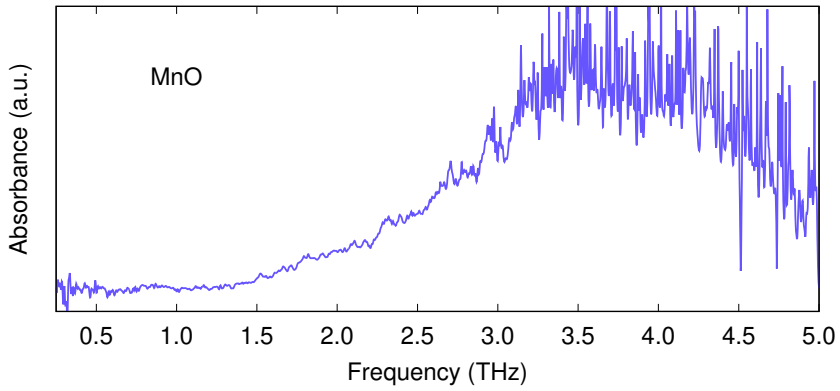
MnO
Absorbance (a.u.)
0.5
1.0
1.5
2.0
2.5
3.0
3.5
4.0
4.5
5.0
Frequency (THz)

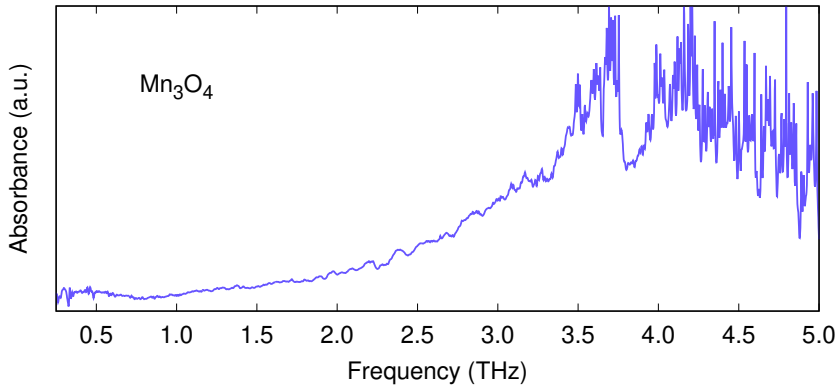
Mn3O4
Absorbance (a.u.)
0.5
1.0
1.5
2.0
2.5
3.0
3.5
4.0
4.5
5.0
Frequency (THz)

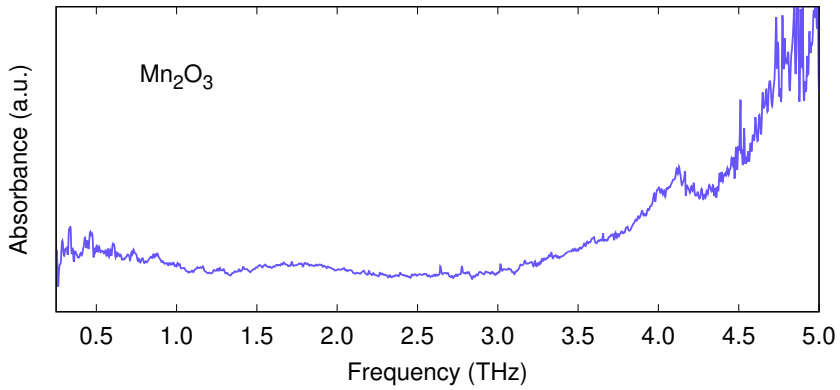
Mn2O3
Absorbance (a.u.)
0.5
1.0
1.5
2.0
2.5
3.0
3.5
4.0
4.5
5.0
Frequency (THz)

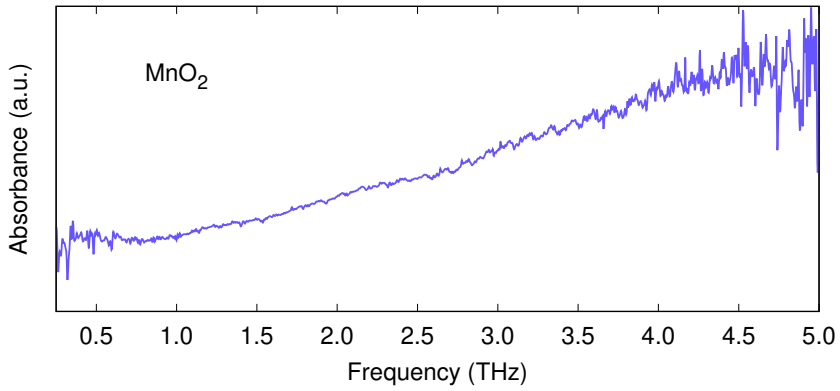
MnO2
Absorbance (a.u.)
0.5
1.0
1.5
2.0
2.5
3.0
3.5
4.0
4.5
5.0
Frequency (THz)

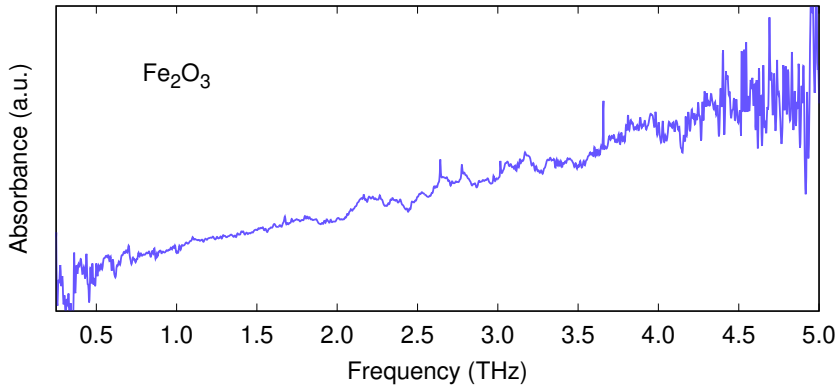
Fe2O3
Absorbance (a.u.)
0.5
1.0
1.5
2.0
2.5
3.0
3.5
4.0
4.5
5.0
Frequency (THz)

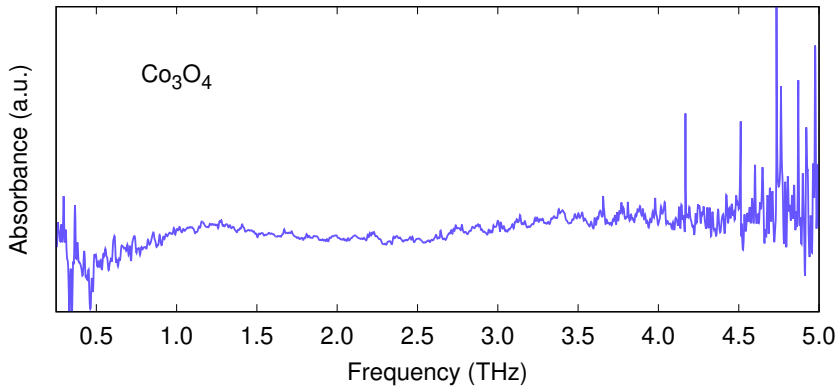
Co3O4
Absorbance (a.u.)
0.5
1.0
1.5
2.0
2.5
3.0
3.5
4.0
4.5
5.0
Frequency (THz)

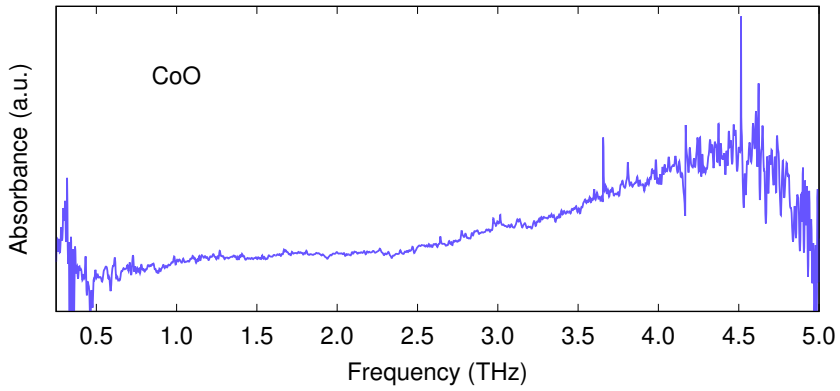
CoO
Absorbance (a.u.)
0.5
1.0
1.5
2.0
2.5
3.0
3.5
4.0
4.5
5.0
Frequency (THz)

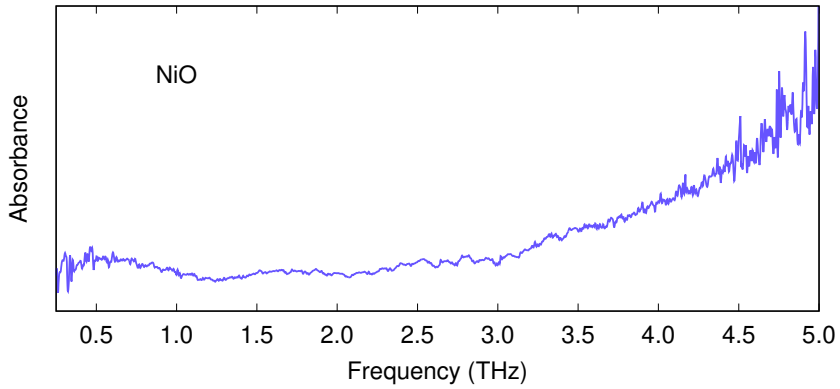
NiO
Absorbance
0.5
1.0
1.5
2.0
2.5
3.0
3.5
4.0
4.5
5.0
Frequency (THz)

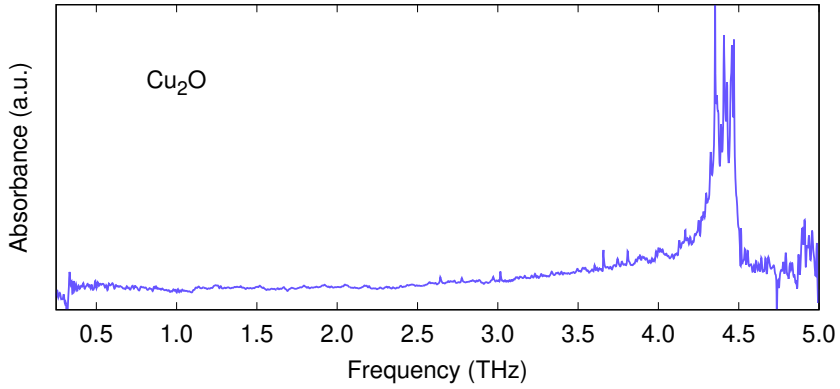
Cu2O
Absorbance (a.u.)
0.5
1.0
1.5
2.0
2.5
3.0
3.5
4.0
4.5
5.0
Frequency (THz)

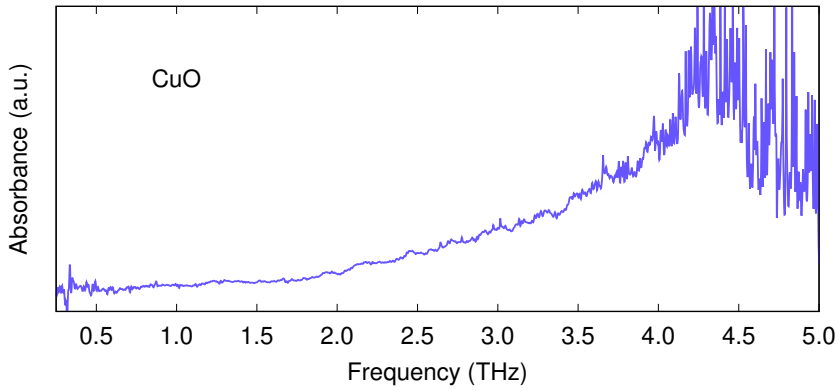
CuO
Absorbance (a.u.)
0.5
1.0
1.5
2.0
2.5
3.0
3.5
4.0
4.5
5.0
Frequency (THz)

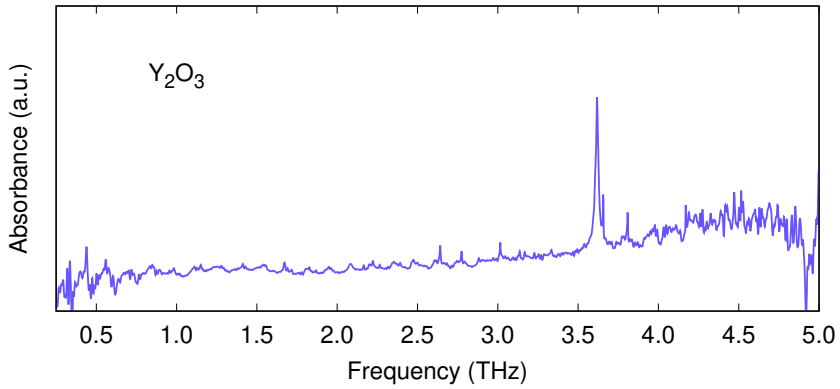
Y_2O_3
Absorbance (a.u.)
0.5
1.0
1.5
2.0
2.5
3.0
3.5
4.0
4.5
5.0
Frequency (THz)

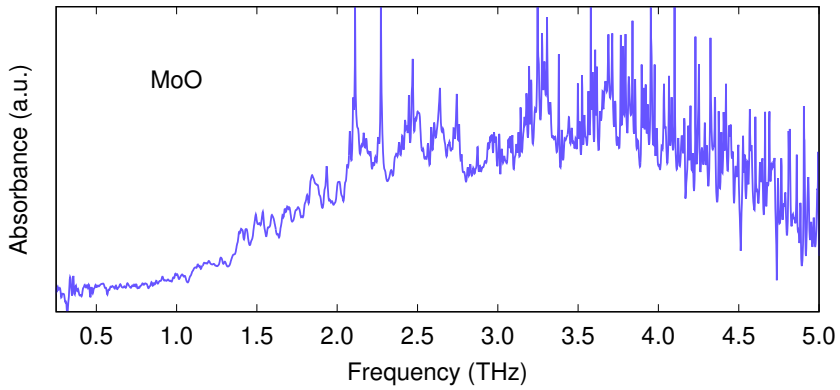
MoO
Absorbance (a.u.)
0.5
1.0
1.5
2.0
2.5
3.0
3.5
4.0
4.5
5.0
Frequency (THz)

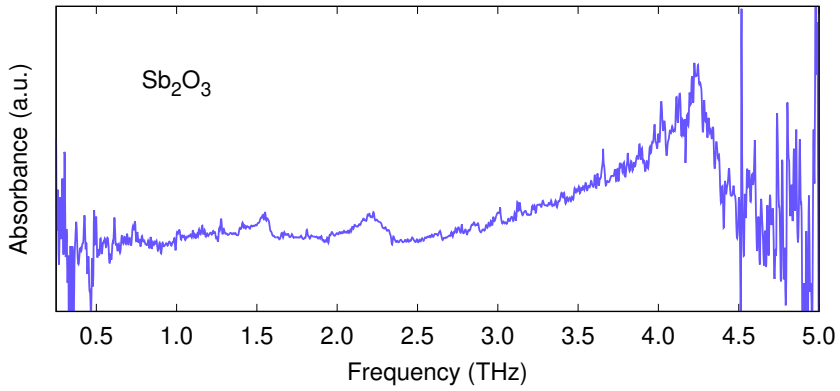
Absorbance (a.u.)
Sb_2O_3
0.5
1.0
1.5
2.0
2.5
3.0
3.5
4.0
4.5
5.0
Frequency (THz)

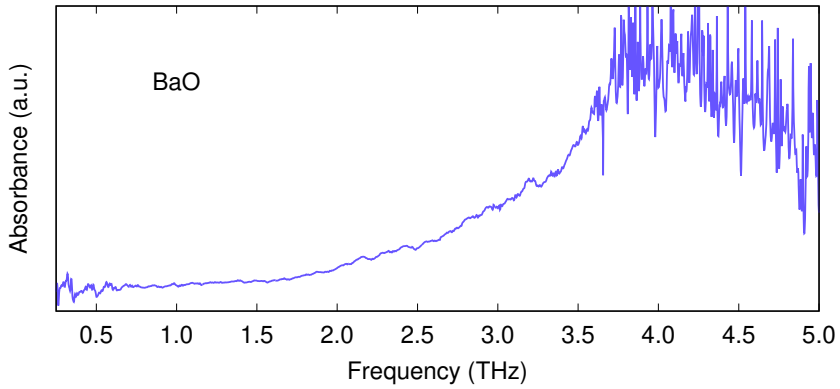
Absorbance (a.u.)
BaO
0.5
1.0
1.5
2.0
2.5
3.0
3.5
4.0
4.5
5.0
Frequency (THz)

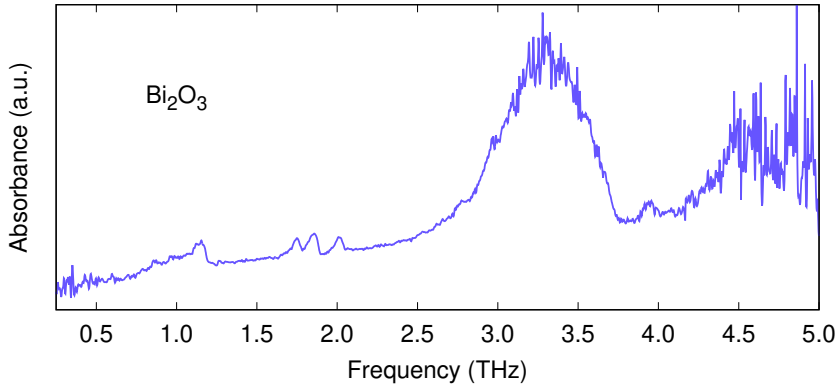
Absorbance (a.u.)
Bi_2O_3
0.5
1.0
1.5
2.0
2.5
3.0
3.5
4.0
4.5
5.0
Frequency (THz)

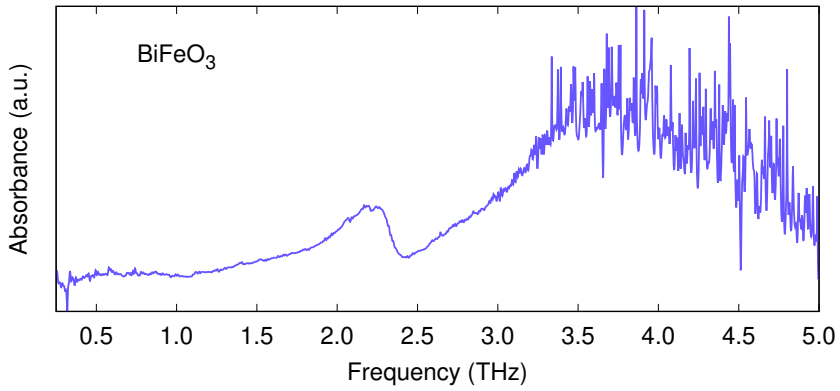
BiFeO3
Absorbance (a.u.)
0.5
1.0
1.5
2.0
2.5
3.0
3.5
4.0
4.5
5.0
Frequency (THz)

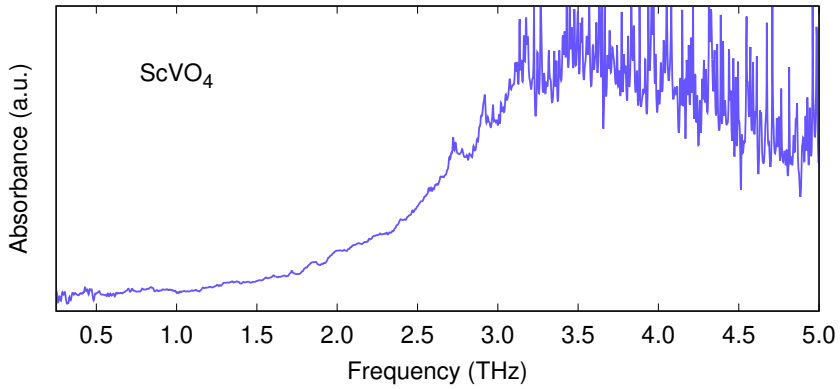
ScVO4
Absorbance (a.u.)
0.5
1.0
1.5
2.0
2.5
3.0
3.5
4.0
4.5
5.0
Frequency (THz)

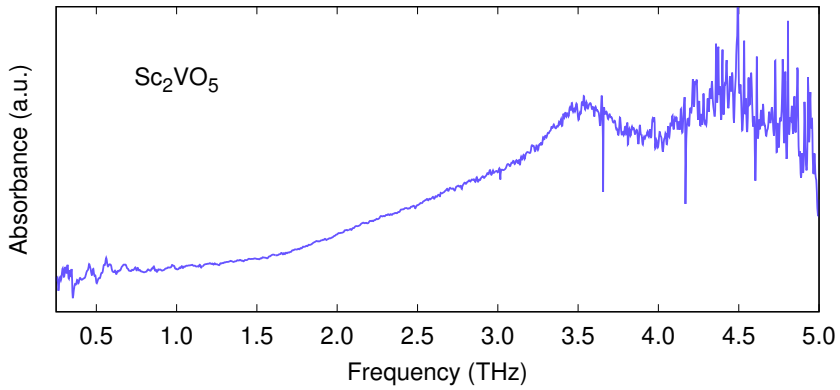
Sc2VO5
Absorbance (a.u.)
0.5
1.0
1.5
2.0
2.5
3.0
3.5
4.0
4.5
5.0
Frequency (THz)

This thesis was typeset using LaTeX, originally developed by Leslie Lamport and based on Donald Knuth's TeX. A template that can be used to format a PhD dissertation with this look & feel has been released under the permissive AGPL license, and can be found online at github.com/suchow/Dissertate or from its lead author, Jordan Suchow, at suchow@post.harvard.edu.

References

[1] Y. Ueno, K. Ajito "Analytical terahertz spectroscopy." *Analytical Science* **185**, 92, (2008) | doi:10.2116/analsci.24.185.

[2] B. Jin, C. Zhang, P. Wu, S. Liu "Recent Progress of Terahertz Spectroscopy on Medicine and Biology in China" *Terahertz Science and Technology* **3** (2010)

[3] S. S. Dhillon *et al* "The 2017 terahertz science and technology roadmap" *J. Phys. D. Appl. Phys.* **50**, 043001 (2017)

[4] M. D. King, P. M. Hakey, T. M. Korter "Discrimination of Chiral Solids: A Terahertz Spectroscopic Investigation of l- and dl-Serine." *J of Phys Chem A*, **114**(8), 2945–2953. (2010) | doi:10.1021/jp911863v

[5] Y.-C. Shen, P. F. Taday "Development and Application of Terahertz Pulsed Imaging for Nondestructive Inspection of Pharmaceutical Tablet." *IEEE Journal of Selected Topics in Quantum Electronics* **14**, 2, 407–415 (2008) | doi:10.1109/jstqe.2007.911309

[6] D. Markl, M. Ruggiero, J. Zeitler "Pharmaceutical applications of terahertz spectroscopy and imaging." **21**, 45-50 (2016)

[7] M. Kemp, P.F. Taday, B. Cole, *et al.* "Security applications of terahertz technology." *Proc Spie* 5070 (2003)

[8] C. Baker, T. Lo, W. R. Tribe, *et al.* "Detection of Concealed Explosives at a Distance Using Terahertz Technology." in *Proceedings of the IEEE* **95**, 8, 1559–1565 (2007) | doi:10.1109/jproc.2007.900329

[9] J. F. Federici, B. Schulkin, F. Huang, *et al.* "THz imaging and sensing for security applications—explosives, weapons and drugs." *Semiconductor Science and Technology* **20**, 7 (2005) | doi:10.1088/0268-1242/20/7/018

[10] M. O. Alnabooda, R. M. Shubair, N. R. Rishani, G. Aldabbagh "Terahertz,spectroscopy and imaging for the detection and identification of Illicit drugs" *Sensors Networks Smart and Emerging Technologies (SENSET)* (2017) | doi:10.1109/senset.2017.8125065

[11] K. Kawase, Y. Ogawa, Y. Watanabe, H. Inoue "Non-destructive terahertz imaging of illicit drugs using spectral fingerprints." *Optics Express* **11**, 20, 2549 (2003) | doi:10.1364/oe.11.002549

[12] W. Liu, Y. Zhang, S. Yang, D. Han "Terahertz time-domain attenuated total reflection spectroscopy applied to the rapid discrimination of the botanical origin

of honeys." *Spectrochim Acta A Mol Biomol Spectrosc.* **196**, 123-130. (2018) | doi:10.1016/j.saa.2018.02.009.

[13] S.-T. Han, W. K. Park, Y.-H.Ahn, *et al.* "Development of a compact sub-terahertz gyrotron and its application to t-ray real-time imaging for food inspection." in *37th International Conference on Infrared, Millimeter, and Terahertz Waves* (2012) | doi:10.1109/irmmw-thz.2012.6380390

[14] J. Hesler, R. Prasankumar, J. Tignon "Advances in terahertz solid-state physics and devices" *J. App. Physics* **126**, 110401 (2019) | doi:10.1063/1.5122975

[15] J.M. Chamberlain, R.E. Miles, C.E. Collins, D.P. Steenson "Introduction to Terahertz Solid-State Devices" (eds) New Directions in Terahertz Technology. NATO ASI Series (Series E: Applied Sciences), **334** Springer, Dordrecht doi:10.1007/978-94-011-5760-5_1

[16] J. Hesler, R. Prasankumar, and Jerome Tignon "Advances in terahertz solid-state physics and devices" *J of App Phys* **126** 110401 (2019) | doi:10.1063/1.5122975

[17] J.S. Rieh, D.H. Kim, K. Kim, H. Kim "Recent Advances in Solid-State Electronic Terahertz Systems" *Convergence of Terahertz Sciences in Biomedical Systems* Springer, Dordrecht (2012) | doi:10.1007/978-94-007-3965-9_6

[18] B. Stuart; "Infrared Spectroscopy: Fundamentals and Applications" *John Wiley & Sons ltd*, (2004)

[19] H. Hoshina, Y. Saito, T. Furuhashi, *et al.* "Terahertz Spectroscopy for Characterization of Hydrogen Bonding and Cross-linked Structure Dynamics in Polyurethane" *J of Infrared, Millimeter, and Terahertz Waves* **41**, 265–275 (2020)

[20] H. Hoshina, "Noninvasive mail inspection using terahertz radiation." *SPIE Newsroom* (2009) | doi:10.1117/2.1200902.1505

[21] H. Zhong, A. Redo-Sanchez, X.-C Zhang "Identification and classification of chemicals using terahertz reflective spectroscopic focal-plane imaging system." *Optics Express* **14**, 20, 9130 (2006) | doi:10.1364/oe.14.009130

[22] A. J. L. Adam, P. C. M. Planken, S. Meloni, J. Dik "Terahertz imaging of hidden paint layers on canvas." in *34th International Conference on Infrared, Millimeter, and Terahertz Waves* (2009) | doi:10.1109/icimw.2009.5324616

[23] K. Fukunaga, I. Hosako "Innovative non-invasive analysis techniques for cultural heritage using terahertz technology." *Comptes Rendus Physique* **11**, 7-8, 519–526 (2010) | doi:10.1016/j.crhy.2010.05.004

[24] P.M. Yarbrough, K.L. Livesey, R.E. Camley, R. Macêdo "Far-Infrared Reflection from Heterostructures Made of Ultrathin Ferromagnetic Layers" *Phys. Rev. Applied* **12** 024004 (2019)

[25] D. Hicks, C. Toher, D.C. Ford, *et al.* "AFLOW-XtalFinder: a reliable choice to identify crystalline prototype" *NPJ Comp. Mat.* **7**, 1 (2021) | doi:10.1038/s41524-020-00483-4

[26] G. Pilania, C. Wang, X. Jiang, *et al.* "Accelerating materials property predictions using machine learning." *Sci Rep* **3**, 2810 (2013) | doi:10.1038/srep02810

[27] V. Baltz A. Manchon, M. Tsoi, *et al.* "Antiferromagnetic spintronics" *Rev. Mod. Phys.* **90**, 015005 (2018) | doi:10.1103/RevModPhys.90.015005

[28] S.M. Rezende, A. Azevedo, R.L. Rodríguez-Suárez "Introduction to antiferromagnetic magnons" *J. Appl. Phys.* **126**, 151101 (2019) | doi:10.1063/1.5109132

[29] M.R. Wasielewski, M.D.E. Forbes, N.L. Frank, *et al.* "Exploiting chemistry and molecular systems for quantum information science." *Nat Rev Chem* **4**, 490–504 (2020) | doi:10.1038/s41570-020-0200-5

[30] H. Hoshina, Y. Saito, T. Furuhashi, *et al.* "Terahertz Spectroscopy for Characterization of Hydrogen Bonding and Cross-linked Structure Dynamics in Polyurethane." *J Infrared Milli Terahz Waves* **41**, 265–275 (2020) | doi:10.1007/s10762-019-00667-0

[31] The Nobel Prize in Chemistry 2021. NobelPrize.org. Nobel Prize Outreach AB 2022. Mon. 11 Apr 2022. https://www.nobelprize.org/prizes/chemistry/2021/summary

[32] D.M. Slocum, E.J. Slingerland, R.H. Giles, T.M. Goyette "Atmospheric absorption of terahertz radiation and water vapor continuum effects" *J Quant Spec and Rad Trans* **127**, 49-63 (2013)

[33] Q. Chen, X.-C. Zhang "Polarization modulation in optoelectronic generation and detection of terahertz beams." *Applied Physics Letters*, **74**, 23, 3435–3437 (1999) | doi:10.1063/1.124119

[34] R. W. Boyd "Nonlinear Optics" Academic Press (2003) ISBN:0121216829

[35] Y. Lee "Principles of Terahertz Science and Technology" (1ed) Springer (2009)

[36] M. Hoffman, K.L. Yeh, J. Hebling, K. Nelson "Efficient terahertz generation by optical rectification at 1035 nm", *Optics Express* **15**, 11706 (2007)

[37] A. Ahmed "A Terahertz Spectrometer for the Study of Multilayered Optics & Complex Materials" M.Sc. Thesis (2021)

[38] J.-P. Negel, R. Hegenbarth, A. Steinmann, *et al.* "Compant and cost-effective scheme for THz generation via optical rectification in GaP and GaAS using novel fs laser oscillators" *Appl Phys B* **103**, 45-50 (2011)

[39] A. Jose, A. Montecillo, A. De Los Reyes, *et al.* "Enhanced terahertz emission of a gallium arsenide thin film on a porous silicon distributed Bragg reflector designed at 800nm wavelength" *Optical Materials* **92**, 335–340 (2019)

[40] S. Deb, A. Saha "Broadband Second-Harmonic Generation in the Mid-Infrared Region in a Tapered Zinc Telluride Slab Using Total Internal Reflection Random Quasi-Phase Matching" *IPCSIT* **28** (2012)

[41] A. Schneider, M. Stillhart, P. Günter "High efficiency generation and detection of terahertz pulses using laser pulses at telecommunication wavelengths" *Optics Express* **14**, 12, 5376 (2006)

[42] Z. Zhao, A. Schwagmann, F. Ospald, *et al.* "Thickness dependence of the terahertz response in ⟨110⟩-oriented GaAs crystals for electro-optic sampling at 1.55 μm" *The Optics Society of America* **18**, (2010)

[43] B. Wu, L. Cao, Q. Fu, *et al.* "Comparison of the Detection Performance of Three Nonlinear Crystals For the Electro-optic Sampling of a FEL-THz Source" In *Proceedings of IPAC*, Dresdan, Germany (2014)

[44] W. Cui, K. M. Awan, R. Huber, *et al.* "Broadband and High-Sensitivity Time-Resolved THz System Using Grating-Assisted Tilted-Pulse-Front Phase Matching" *Adv. Optical Mater* 2101136 (2021) | doi:10.1002/adom.202101136

[45] Q. Wu, X.-C. Zhang, "Free-space electro-optics sampling of mid-infrared pulses." *Appl. Phys. Lett.* **71**, 10, 1285–1286 | doi:10.1063/1.119873 (1997)

[46] A. Leitenstorfer, S. Hunsche, J. Shah,*et al.* "Femtosecond Charge Transport in Polar Semiconductors" *Appl. Phys. Lett.* **74**, 1516 (1999)

[47] J. Huang, Y. Li, Y. Gao, *et al.* "High efficient terahertz generation from cryogenic gallium phosphide based on collinear difference frequency" in *Proceedings Volume 11046, Fifth International Symposium on Laser Interaction with Matter* 1104631 (2019) | doi:10.1117/12.2524100

[48] X. Zheng, C. McLaughlin, V. Colin,*et al.* "Organic broadband Terahertz sources and sensors" *J of Nanoelectronics and Optoelectronics*, **2**, 19, 58-76 (2007) | doi:c10.1166/jno.2007.005

[49] T. Kampfrath, J. Nötzold, M. Wolf "Sampling of broadband terahertz pulses with thick electro-optic crystals." *Applied Physics Letters* **90**, 23, 231113 (2007) | doi:10.1063/1.2746939

[50] Q. Wu, X.-C. Zhang "Free-space electro-optic sampling of terahertz beams." *Appl. Phys. Lett.* **67**, 3523–3525 (1995)

[51] A. Leitenstorfer, S. Hunsche, J. Shah, *et al.* "Detectors and sources for ultra-broadband electro-optic sampling: experiment and theory." *Appl. Phys. Lett.* **74**, 1516–1518 (1999).

[52] B. E. A. Saleh, M. C. Teich "Fundamentals of Photonics" John Wiley & Sons, Inc. (1991) | doi:10.1002/0471213748 ISBN:9780471839651

[53] F. Pockels *Goettinger Abhandl* **39** (1894)

[54] F. Pockels *Lehrbuch der Kristalloptik* Leipzig (1906)

[55] P. Steglich, C. Mai, C. Villringer, A. Mai "Direct observation and simultaneous use of linear and quadratic electro-optical effects" *J. Phys. D: Appl. Phys.* **53**, 125106 (2020)

[56] G. Hagn "Electro-optic effects and their application in indium phosphide waveguide devices for fibre optic access networks" Doctoral Thesis (2001)

[57] B. Pradarutti, G. Matthäus, S. Riehemann, *et al.* "Highly efficient terahertz electro-optic sampling by material optimization at 1060 nm", *Optics Communications* **281**, 5031–5035 (2008)

[58] J. Neu, C. Schmttenmaer, "Tutorial: An introduction to terahertz time domain spectroscopy (THz-TDS)" *J of Appl. Phys.* **124**, 231101 | doi:10.1063/1.5047659 (2018)

[59] J. F. Doyle "Wave Propagation in Structures: Spectral Analysis Using Fast Discrete Fourier Transforms" *Springer-Verlag* (1997) | ISBN: 978-1-4612-7304-2,978-1-4612-1832-6

[60] M. Boas "Mathematical Methods in the Physical Sciences" (3ed) *John Wiley & Sons, Inc*

[61] L. Duvillaret, F. Garet, J.L. Coutaz, "A Reliable Method for Extraction of Material Parameters in Terahertz Time-Domain Spectroscopy" *IEEE J of Selected Topics in Quantum Electronics*, **2**, 3 (1996)

[62] E. Palik "Handbook of Optical Constants of Solids" (3ed) *Elsevier*

[63] A. Ahmed, A. Braconnier, J. Gibbs and J. A. J. Burgess, "Low-cost antireflection coatings for terahertz light employing multilayered polymer films and adhesives," in *2021 Photonics North (PN)* 1-1 (2021) | doi:10.1109/PN52152.2021.9597923.

[64] M. Naftaly, R.E. Miles "A method for removing etalon oscillations from THz time-domain spectra" *Optics Communications* **280**, 291–295 (2007)

[65] P.R. Griffiths and J.A. de Haseth "Fourier Transform Infrared Spectrometry" (2ed) *John Wiley & Sons, Inc.* (2007)

[66] P.N. Nguyen, H. Watanabe, Y. Tamaki, et al. "Relaxation dynamics of [Re(CO)2(bpy)P(OEt)32](PF6) in TEOA solvent measured by time-resolved attenuated total reflection terahertz spectroscopy" *Sci. Rep.* **9**, 11772 (2019) | doi:10.1038/s41598-019-48191-4

[67] T. R. Globus, D. L. Woolard, T. Khromova, *et al.* "THz-Spectroscopy of Biological Molecules" *J Biol Phys* **29** 2-3, 89-100 (2003) | doi:10.1023/A:1024420104400

[68] T. Tanabe, A. Kenmochi, Y. Oyama, *et al.* "Attenuated Total Reflection Spectroscopy of Liquids using GaP-Raman Terahertz Spectrometer." in *Joint 30th International Conference on Infrared and Millimeter Waves and 13th International Conference on Terahertz Electronics.* (2005)| doi:10.1109/icimw.2005.1572401

[69] H. Hirori, K. Yamashita, M. Nagai, and K. Tanaka, "Attenuated Total Reflection Spectroscopy in Time Domain Using Terahertz Coherent Pulses" *Jap. J. of Appl. Phys.* **43**, 10A, 1287–1289 (2004)

[70] G. Gauglitz, T. Vo-Dinh; "Handbook of Spectroscopy", (Wiley-VCH, 2003)

[71] S. Ramani "Metamaterial Radiation From Attenuated Total Reflection at Terahertz Frequencies" Doctoral Thesis (2006)

[72] A. A. Otto "A new method for exciting non-radioactive surface plasma oscillations." *Phys. Stat. Sol.* **26**, K99-K101 (1968)

[73] A. A. Otto "Exitation of nonradiative surface plasma waves in silver by the method of frustrated total reflection." *Z Phys* **216**, 398-410 (1968)

[74] E. Kretschmann, H. Reather "Radiative decay of nonradiative surface plasmon excited by light" *Z. Naturf.* **23A**, 2135-2136 (1968)

[75] J. Moore, C.Davis, M. Coplan, "Building Scientific Apparatus: A Practical Guide to Design and Construction" (3ed) Westview Press (2003)

[76] https://www.americanlaboratory.com/913-Technical-Articles/1457-Attenuated-Total-Reflection-Explores-the-Terahertz-Region/ (Accessed March 2022)

[77] Y. Huang, R. Singh, L. Xie, Y. Ying "Attenuated Total Reflection for Terahertz Modulation, Sensing, Spectroscopy and Imaging Applications: A Review" *Appl. Sci.* **10**, 4688 (2020)| doi:10.3390/app10144688

[78] H. Hirori, K. Yamashita, M. Nagai, and K. Tanaka, "Terahertz time-domain attenuated total reflection spectroscopy in water and biological solution" *Jpn. J. Appl. Phys.* **43**, L1287 (2004)

[79] A. Soltani, D. Jahn, L. Duschek, *et al.* "Attenuated Total Reflection Terahertz Time-Domain Spectroscopy: Uncertainty Analysis and Reduction Scheme," *IEEE Transactions on Terahertz Science and Technology* **6**, 1, 32-39 (2016) | doi:10.1109/TTHZ.2015.2505909.

[80] H. Hirori, A. Doi, F. Blanchard, K. Tanaka "Single-cycle terahertz pulses with amplitudes exceeding 1 MV/cm generated by optical rectification in $LiNbO_3$" *App. Phys. Lett.* **98**, 091106 (2011)

[81] P.U. Jepsen, D.G. Cooke, M. Koch "Terahertz spectroscopy and imaging – Modern techniques and applications" *Laser Photonics Rev.* **5**, 1, 124–166 (2011) | doi:10.1002/lpor.201000011

[82] Y. Berozashvili et. al., *J. Phys. D Appl. Phys.* **22**, 682 (1989)

[83] M. Naftaly, R. Dudley "Methodologies for determining the dynamic ranges and signal-to-noise ratios of terahertz time-domain spectrometers" *Optics Letters* **34**, 8, 1213 (2009)

[84] X. Xin, H. Altan, A. Saint, *et al.* "Terahertz absorption spectrum of para and ortho water vapors at different humidities at room temperature" *J Of Applied Phys.* **100**, 094905 (2006)

[85] M. T. Ruggiero, T. Bardon, M. Strlič, *et al.* "Assignment of the Terahertz Spectra of Crystalline Copper Sulfate and Its Hydrates via Solid-State Density Functional Theory" *J. Phys. Chem. A* **118**, 43, 10101–10108 (2014)

[86] C. Kittel, "Introduction to Solid State Physics" (8ed) *Wiley, New York* (2005)

[87] S. Maekawa, T. Tohyama, S.E. Barnes, *et al.* "Physics of Transition Metal Oxides" (Springer-Verlag Berlin, 2004)

[88] The Nobel Prize in Physics 2007. NobelPrize.org. Nobel Prize Outreach AB 2022. Thu. 21 Apr 2022. https://www.nobelprize.org/prizes/physics/2007/summary

[89] L. Landau "Theory of the Superfluidity of Helium II." *Physical Review*, **60** (4), 356–358. (1941) | doi:10.1103/physrev.60.356

[90] K. S. Kumar, G. L. Prajapati, R. Dagar, *et al.* "Terahertz Electrodynamics in Transition Metal Oxides." *Advanced Optical Materials* 1900958 (2019) | doi:10.1002/adom.201900958

[91] N.A. Spaldin "Multiferroics beyond electric-field control of magnetism". *Proc. Roy. Soc. A.* **476**, 2233 0542. arXiv:1908.08352 (2020) | doi:10.1098/rspa.2019.0542.

[92] M. Fiebig, T Lottermoser, M. Trassin "The evolution of multiferroics" *Nature Reviews Materials* **1**, 16046 (2016)

[93] S. Ivanov "Multiferroic complex metal oxides: Main features of preparation, structure, and properties" *Science and Technology of Atomic, Molecular, Condensed Matter & Biological Systems* Elsevier **2**, 163-238 (2012) | doi:10.1016/B978-0-44-453681-5.00007-8

[94] P. Barone, B. Sanyal, S. Picozzi "Multiferroics: theory, mechanisms, and materials" *Science and Technology of Atomic, Molecular, Condensed Matter & Biological Systems* **2**, 129-161 (2012)

[95] L. Petersen, P. Hedegård "A simple tight-binding model of spin–orbit splitting of sp-derived surface states" *Surface Science* **459**, 1–2 49-56 (2000)

[96] C. Caspers, V. P. Gandhi, A. Magrez, *et al.* "Sub-terahertz spectroscopy of magnetic resonance in $BiFeO_3$ using a vector network analyzer," *Applied Physics Letters*, **108**, 24, 106–111 (2016)

[97] M. Bialek, T. Ito, H. Rønnow, and J. P. Ansermet, "Terahertz-optical properties of a bismuth ferrite single crystal" *Physical Review B* **99**, 6, 25–31 (2019)

[98] A. Kumar, J. F. Scott, and R. S. Katiyar, "Electric control of magnon frequencies and magnetic moabsorbancement of bismuth ferrite thin films at room temperature," *Applied Physics Letters* **99**, 6, 2–4 (2011)

[99] G. A. Komandin, V. I. Torgashev, A. A. Volkov, *et al.* "Optical Properties of BiFeO3 Ceramics in the Frequency Range 0.3–30.0 THz" *Physics of the Solid State* **52**, 4, 734–743 (2010)

[100] M. Bialek, A. Magrez, A. Murk, and J. P. Ansermet, "Spin-wave resonances in bismuth orthoferrite at high temperatures," *Phys Rev B*, **97**, 5, 1–5 (2018)

[101] A.J. Braconnier "Terahertz Scanning Fabry-Pérot Cavity" M.Sc. Thesis (In Progress) (2022)

[102] I. E. Dzyaloshinskii *Sov. Phys. JETP* **37**, 881 (1959)

[103] D. N. Astrov "Magnetoelectric Effect in Chromium Oxide" *Sov Phys. JETP* **13**, 4, 729-733 (1961)

[104] J.E Greedan "Magnetic oxides in Encyclopedia of Inorganic chemistry" R. Bruce King, Ed. *John Wiley & Sons* (1994) ISBN 0-471-93620-0

[105] M. Fechner, A. Sukhov, L. Chotorlishvili, *et al.* "Magnetophononics: Ultrafast spin control through the lattice" *Phys. Rev. Materials 2*, 064401 (2018) | doi:10.1103/PhysRevMaterials.2.064401

[106] C. Vogel, J. Stemann, K. Holldack, *et al.* "Thermal Treatment of Chromium(III) Oxide with Carbonates Analyzed by Far-Infrared Spectroscopy." *Applied Spectroscopy* **69** (10) 1210-1214 (2015) | doi:10.1366/15-07878

[107] K. Brajesh, R. Bhunia, S. Gupta, *et al.* "Low temperature magnetic and dielectric properties correlation in Fe-doped copper (II) oxide ceramics for potential device application" *arXiv* (2021) | doi:10.48550/ARXIV.2112.11874

[108] Avishek Maity, Steffen Schwesig, Fabian Ziegler, *et al.* "Magnons in the Multiferroic Phase of Cupric Oxide" **257**, 5, 1900704 (2020) | doi:10.1002/pssb.201900704

[109] V. Krivoruchko, "Electrically active magnetic excitations in antiferromagnets" *Low Temp Phys.* **38**, 807-818 (2012)

[110] S. Knight, D. Prabhakaran, M. Schubert, "Electromagnon excitation in cupric oxide measured by Fabry-Pérot enhanced terahertz Mueller matrix ellipsometry" *Sci Rep* **9**, 1353 (2019)

[111] H. Tokoro, K. Nakabayashi, S. Nagashima, *et al.* "Optical Properties of Epsilon Iron Oxide Nanoparticles in the Millimeter- and Terahertz-Wave Regions" *Bull. Chem. Soc. Jpn.* **95**, 538–552 (2022) | doi:10.1246/bcsj.20210406

[112] Ohkoshi, Si., Namai, A., Yamaoka, T. *et al.* "Mesoscopic bar magnet based on ϵ-Fe2O3 hard ferrite." *Sci Rep* 6, 27212 (2016) | doi:10.1038/srep27212

[113] D. Vrublevskiy, J. A. Lussier, J. R. Panchuk, *et al.* "Understanding the Interplay of Vacancy, Cation, and Charge Ordering in the Tunable Sc2VO5+δ Defect Fluorite System" *Inorganic Chemistry* **60**, 2, 872-882 (2021) | doi:10.1021/acs.inorgchem.0c02992

[114] H. Cong, H. Zhang, B. Yao, *et al.* "ScVO4: Explorations of Novel Crystalline Inorganic Optical Materials in Rare-Earth Orthovanadate Systems." *Crystal Growth & Design* **10**, 10, 4389–4400 (2010) | doi:10.1021/cg1004962

[115] Y. P. Wang, S. S. Li, W. X. Ji, *et al.* "Bismuth oxide film: a promising room-temperature quantum spin Hall insulator." *J Phys Condens Matter* **30** (10) 105303 (2018) | doi: 10.1088/1361-648X/aaabaa

[116] R. Noguchi, T. Takahashi, K. Kuroda, *et al.* "A weak topological insulator state in quasi-one-dimensional bismuth iodide." *Nature* **566** (7745) 518-522 (2019) | doi: 10.1038/s41586-019-0927-7. Epub 2019 Feb 11. Erratum in: Nature. 2020

[117] H. Zhao *et al.* "Generation and Manipulation of Chiral Terahertz Waves in the Three-Dimensional Topological Insulator Bi2Te3," *Adv. Photon.* **2** (6) 066003 (2020) | doi:10.1117/1.AP.2.6.066003.

[118] R. J. Betsch, W. B. White "Vibrational spectra of bismuth oxide and the sillenite-structure bismuth oxide derivatives." *Spectrochimica Acta Part A: Molecular Spectroscopy* **34** (5) 505–514 (1978) | doi:10.1016/0584-8539(78)80047

[119] Y. Ueno, K. Ajito "Analytical Terahertz Spectroscopy" *Analytical Sciences* **24**, 2, 185–192 (2008) | doi:10.2116/analsci.24.185

[120] H. Umeda, M. Takagi, S. Yamada, *et al.* "Quantum control of molecular chirality: Optical isomerization of difluorobenzo[c]phenanthrene," J. Am. Chem. Soc. *124*, 31, 9265–9271 (2002).

[121] M.T. Ruggiero, J. Sibik, J.A. Zeitler, and T.M. Korter "Examination of L-Glutamic Acid Polymorphs by Solid-State Density Functional Theory and Terahertz Spectroscopy" *J Phys Chem A* **120**, 7490 (2016)

[122] M.D. King, P.M. Hakey, T.M. Korter "Discrimination of Chiral Solids: A Terahertz Spectroscopic Investigation of L- and DL-Serine" *J Phys Chem A* **114**, 8, 2945–2953 (2010) | doi:10.1021/jp911863v

[123] J. Neu, H. Nikonow, and C. A. Schmuttenmaer "Terahertz Spectroscopy and Density Functional Theory Calculations of dl-Norleucine and dl-Methionine" *J. Phys. Chem. A* **122**, 5978–5982 (2018)

[124] Chen, W., Peng, Y., Jiang, X. *et al.* "Isomers Identification of 2-hydroxyglutarate acid disodium salt (2HG) by Terahertz Time-domain Spectroscopy." *Sci Rep 7* 12166 (2017) | doi:10.1038/s41598-017-11527-z

[125] M. Hu, M. Tang, H. Wang, *et al.* "Terahertz, infrared and Raman absorption spectra of tyrosine enantiomers and racemic compound." *Spectrochimica*

Acta Part A: Molecular and Biomolecular Spectroscopy **254**, 119611 (2021) | doi:10.1016/j.saa.2021.119611

[126] A. B. True, K. Schroeck, T. A. French, C. A. Schmuttenmaer "Terahertz Spectroscopy of Histidine Enantiomers and Polymorphs" *J of Infrared, Millimeter, and Terahertz Waves 32* 691–698 (2011)

[127] T. Ding, R. Li, J. A. Zeitler, *et al.* "Terahertz and far infrared Spectroscopy of alanine-rich peptides having variable ellipticity" *Optics Express* **18**, 26, 27431 (2010)

[128] K. Siegrist, C. R. Bucher, I. Mandelbaum, *et al.* "High-Resolution Terahertz Spectroscopy of Crystalline Trialanine: Extreme Sensitivity to Beta-Sheet Structure and Cocrystallized Water" *J. Am. Chem. Soc.* **128**, 5764-5775 (2006)

[129] T.M. Korter, R. Balu, M.B. Campbell, *et al.* "Terahertz spectroscopy of solid serine and cysteine." *Chem. Phys. Lett.* **418**, 1-3, 65-70 (2006) | doi:10.1016/j.cplett.2005.10.097

[130] Yu B, Zeng F, Yang Y, et al. "Torsional vibrational modes of tryptophan studied by terahertz time-domain spectroscopy." *Biophysical J* **86**, 3, 1649-1654 (2004) | doi:10.1016/s0006-3495(04)74233-2

[131] M. R. C. Williams, A. B. True, A. F. Izmaylov, *et al.* "Terahertz spectroscopy of enantiopure and racemic polycrystalline valine" *Phys. Chem. Chem. Phys.* **13**, 11719 (2011)

[132] J. Neu, C. T. Nemes, K. P. Regan, *et al.* "Exploring the solid state phase transition in dl-norvaline with terahertz spectroscopy" *Phys. Chem. Chem. Phys* **20**, 276 (2018)

[133] T. Chen, Q. Zhang, Z. Li, X. Yin, F. Hu, "Experimental and theoretical investigations of tartaric acid isomers by terahertz spectroscopy and density functional theory." *Spec. Acta A* (2018) | doi:10.1016/j.saa.2018.06.091

[134] C. Du, X. Zhang, Z. Zhang, "Quantitative analysis of ternary isomer mixtures of saccharide by terahertz time domain spectroscopy combined with chemometrics" *Vibrational Spectroscopy* **100** 64-70 (2019) | doi:10.1016/j.vibspec.2018.11.003.

[135] Z.-P. Zheng, W.-H. Fan, Y.-Q. Liang, Hui Yan, "Application of terahertz spectroscopy and molecular modeling in isomers investigation: Glucose and fructose" *Optics Communications*, **285**, 7, 1868-1871 (2012)

[136] T. Zhang, S. Yan, J. Hao, D. Li, "Experimental and Theoretical Investigations of Terahertz Spectra of the Structural Isomers: Mannose and Galactose" *J. Spec.* (2021) | doi:10.1155/2021/3469262

[137] Jianjun Liu, "Analysis of the terahertz characteristics of pesticide residue isomers," *J. Opt. Technol.* **87**, 440-444 (2020)

[138] M. Tang, M. Zhang, L. Xia, *et al.* "Detection of single-base mutation of DNA oligonucleotides with different lengths by terahertz attenuated total reflection microfluidic cell," *Biomed. Opt. Express* **11**, 5362-5372 (2020)

[139] E. Pickwell, V.P. Wallace "Biomedical applications of terahertz technology." *J Phys D: Appl Phys* **39**, 17, R301-R310 (2006) | doi:10.1088/0022-3727/39/17/r01

[140] Y.-C. Shen, P. F. Taday "Development and Application of Terahertz Pulsed Imaging for Nondestructive Inspection of Pharmaceutical Tablet." *IEEE J of Selected Topics in Quantum Electronics* **14**, 2, 407–415 (2008) | doi:10.1109/jstqe.2007.911309

[141] R. Paschotta, article on 'optical rectification' in the *Encyclopedia of Laser Physics and Technology*, 1. edition October 2008, Wiley-VCH, ISBN 978-3-527-40828-3

[142] "Terahertz Spectroscopy: Principles and Applications", edited by S.L. Dexheimer, author Mario Bertolotti Contemporary Physics **51**, 366-366 (2010)

[143] P. Yarbrough, K. Livesey, R. Camley, R. Macêdo, "Far-Infrared Reflection from Heterostructures Made of Ultrathin Ferromagnetic Layers" *Phys. Rev. App.* **12** (2019) | doi:10.1103/PhysRevApplied.12.024004.

[144] J. Kauppinen, J. Partanen "Fourier Transforms in Spectroscopy" 1 ed. *Wiley-VCH, Berlin* (2001)